Durham E-Theses

Localising the gamma-ray emission region of flaring Flat Spectrum Radio Quasars

COOGAN, ROSEMARY,THERESA

Localising the γ-ray emission region of flaring Flat Spectrum Radio Quasars

Rosemary Theresa Coogan

Supervisors: A. M. Brown and P. M. Chadwick

Very High Energy Gamma Ray Astronomy Group

A Thesis presented for the degree of
Master of Science by Thesis

Very High Energy Gamma Ray Astronomy Group

Department of Physics

University of Durham

UK

September 2015

Dedicated to

Mum

Localising the γ-ray emission region of flaring Flat Spectrum Radio Quasars

Rosemary T. Coogan

Submitted for the degree of Master of Science

September 2015

Abstract

Observations by the Large Area Telescope detector on-board the *Fermi* Gamma-ray Space Telescope are used to examine the $0.1 \leq E_\gamma \leq 300\,\text{GeV}$ γ-ray emission characteristics of flat spectrum radio quasars. Specifically, the γ-ray emission from 3C 454.3 and 3C 279 are analysed in detail, in order to put constraints on the location of the emission region. The variability in the spectral shape is explored, whether evidence of a spectral cutoff can be found and whether or not an energy-dependence of the emitting electron cooling exists. The significance of VHE emission is also quantified.

In May - July 2014, 3C 454.3 exhibited strong flaring behaviour. Observations with the *Fermi*-LAT captured the γ-ray flux increasing fivefold during this period, with two distinct peaks in emission. The peak daily binned flux climbed to $F = (1.3 \pm 0.1) \times 10^{-5}\,\text{ph}\,\text{cm}^{-2}\,\text{s}^{-1}$ on MJD 56823. γ-ray intrinsic flux doubling timescales as small as $\tau_{int} = 0.68 \pm 0.01$ h at a significance of $> 5\sigma$ are found, providing evidence of a compact emission region. Significant $E_{\gamma,emitted} \geq 35$ GeV and $E_{\gamma,emitted} \geq 50$ GeV emission are also observed. The location of the emission region can be constrained to $r \geq 1.3 \times R_{BLR}^{out}$, a location outside the broad-line region. The spectral variation of 3C 454.3 also suggests that these flares may be originating further downstream of the supermassive black hole than the emission before and after the flares.

3C 279 flared spectacularly in June 2015, becoming brighter than ever previously recorded by *Fermi*. The peak daily binned flux reached $F = (2.5 \pm 0.1) \times 10^{-5}\,\text{ph}\,\text{cm}^{-2}\,\text{s}^{-1}$ on MJD 56823. Interestingly, the smallest intrinsic flux doubling timescale is $\tau_{int} = 1.38 \pm 0.16$ h, and no sub-hour flux doubling timescales are found. Significant $E_{\gamma,emitted} \geq 35$ GeV and $E_{\gamma,emitted} \geq 50$ GeV emission are observed during the flare, alongside a significant spectral hardening. Using photon-photon opacity constraints, the location of the emission region must lie at least $r \geq 2.5 \times R_{BLR}$ from the SMBH, the mid-point of the broad-line region. As with 3C 454.3, the spectral variation across the period of interest hints that a multi-zonal model may be applicable to the γ-ray emission.

Declaration

The work in this thesis is based on research carried out by the author in the Department of Physics, Durham University, UK, under the supervision of Prof. Paula M. Chadwick and Dr Anthony M. Brown. No part of this thesis has been submitted elsewhere for any other degree or qualification.

The results and analysis presented in Chapter 4 have been sumbitted for publication in the following paper:

- *Localising the γ-ray emission region during the June 2014 outburst of 3C 454.3*,

  Coogan R. T.; Brown A. M.; Chadwick P. M.

Acknowledgements

Contents

List of Figures

List of Tables

Chapter 1

Introduction

The aim of this thesis is to investigate the high energy gamma-ray (hereafter γ-ray) emission from flat spectrum radio quasars, in order to put constraints on where the γ-ray emission is originating from in these complex and energetic systems. In this chapter, classification schemes between AGN are discussed, as well as the structure and γ-ray emission properties of AGN. The mechanisms for emission within the jets of AGN and the motivation for this work are also outlined. Chapter 2 gives an overview of the method for detecting γ-rays and the mission of the *Fermi*-Large Area Telescope, and Chapter 3 describes how specific flat spectrum radio quasars were selected for analysis in this thesis. Chapters 4 and 5 present the results of the analysis, and the conclusions drawn on the location of the emission region. Chapter 6 summarises the thesis and draws together the conclusions from the previous chapters.

1.1 AGN Unification

At the centre of every massive galaxy in the local universe is a supermassive black hole (SMBH), the mass of which is proportional to the mass of the galaxy spheroid itself (e.g. Kormendy & Richstone 1995, Magorrian et al. 1998). Active galactic nuclei are the central regions of the subset of these galaxies known as 'active' galaxies. A galaxy is considered to be active if the central SMBH is accreting large amounts of interstellar gas and dust onto it, resulting in an increase in mass of the SMBH and the production of a vast amount of energy (Salpeter, 1964; Alexander & Hickox, 2012). This accretion results in a loss of angular momentum of the interstellar gas, as the matter forms an accretion disk surrounding the SMBH and moves towards the SMBH in a spiral path. Depending on the scale of the original host galaxy, the gas needs to lose up to ~99.9% of its angular momentum, and the result of this is a vast expulsion of energy, with up to ~40% of the rest mass of the infalling matter being liberated as energy in the process (Alexander & Hickox, 2012). This liberation of energy causes the central regions of AGN to be incredibly bright, especially considering the compact size of a black hole in comparison with the size of very luminous stellar objects. Although it is not possible to directly observe galaxies
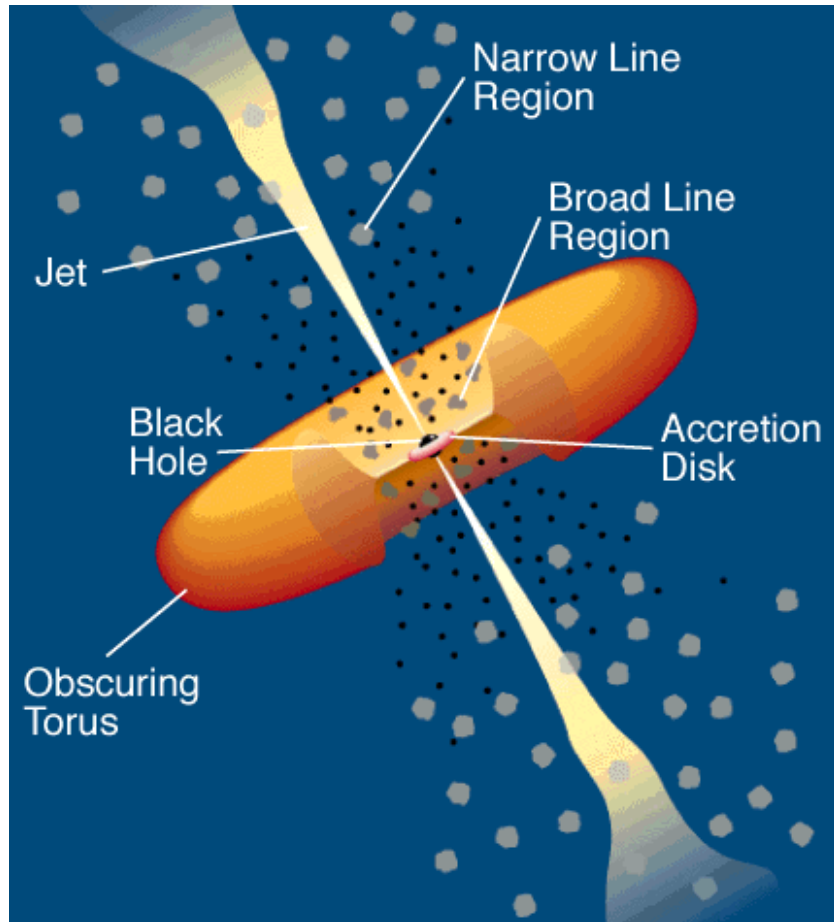
Figure 1.1: Schematic diagram of an active galactic nucleus. Taken from Urry & Padovani (1995).

so close to the central engine, observations at different wavelengths of a large population of AGN have allowed an inner structure that is consistent with these observations to be inferred (Urry & Padovani, 1995).

As can be seen in Fig. 1.1, the SMBH of an AGN is surrounded by several regions of gas. Notable components of an AGN are labelled in Fig. 1.1:

1. The supermassive black hole.

2. The relativistic jet.

3. The accretion disk and hot corona surrounding the SMBH.

4. The broad-line region.

5. The narrow-line region.

6. The molecular torus.

Acronym	Full name
Sy 1 (2)	Seyfert type 1 (2) galaxy
NELG	Narrow-Emission-Line x-ray Galaxy
QSO	Quasi-Stellar Object
BAL QSO	Broad Absorption Line Quasi-Stellar Object
NLRG	Narrow-Line Radio Galaxy
FR I (II)	Fanaroff-Riley type I (II) radio galaxy
BLRG	Broad-Line Radio Galaxy
SSRG	Steep Spectrum Radio Quasar
FSRQ	Flat Spectrum Radio Quasar
BL Lac	BL Lacertae

Table 1.1: Table of commonly used AGN acronyms.

The SMBH is surrounded by a thermally radiating accretion disk of matter, with a hot x-ray emitting corona at the centre. Close to the SMBH and the accretion disk is a region of hot, high velocity gas clouds known as the broad-line region (BLR). These clouds are so-called because they produce broad emission lines when they absorb and re-process the thermal emission from the accretion disk. Further out from the SMBH both the narrow-line region (NLR), in which slower-moving gas clouds produce much narrower emission lines, as well as the large molecular torus (MT) of gas and dust are found. Spanning these structures are relativistically moving jets of plasma, that are expelled from the innermost regions of the AGN both above and below the SMBH. These are perpendicular to the accretion disk and can extend well beyond the inner regions of the nucleus, as will be seen in Fig. 2.1. The mechanism for creating these jets is not well understood, but the result is an extremely energetic flow of charged particles through the regions of gas and dust surrounding the SMBH. These jets may be highly collimated and may or may not be observed as radio-loud, perhaps relating to the host galaxy type or black hole spin (Smith et al., 1986; Wilson & Colbert, 1995; Urry & Padovani, 1995). Approximately 15-20% of AGN are radio-loud, increasing up to ~50% at high optical and x-ray luminosities (Kellerman et al., 1989; Padovani, 1993; Della Ceca et al., 1994; Urry & Padovani, 1995). It's believed that it is from within these relativistic plasma jets that the γ-rays observed from AGN originate, and a potential mechanism for creating this emission will be outlined in Section 1.2.

It is believed that the differences in observational properties between AGN is due to their different orientations with respect to the line of sight. AGN can be classified in three broad groups, based on their angle of inclination (Urry & Padovani, 1995):

1. Type 1: AGN at large inclination, in which the BLR is obscured by the torus. This

```
                         Optical Emission Line Properties
                    _____

                    Type 2 (Narrow Line)   Type 1 (Broad Line)   Type 0 (Unusual)


 Radio-quiet:       Sy 2                    Sy 1
                    NELG                                                                 Black
                    IR Quasar?              QSO                    BAL QSO?              Hole
                                                                                        Spin?

                         ⎧FR I                BLRG                        ⎧BL Lac Objects
 Radio-loud:        NLRG ⎨                    SSRQ            Blazars⎨
                         ⎩FR II               FSRQ                        ⎩(FSRQ)

                    _____>
                              Decreasing angle to line of sight
```
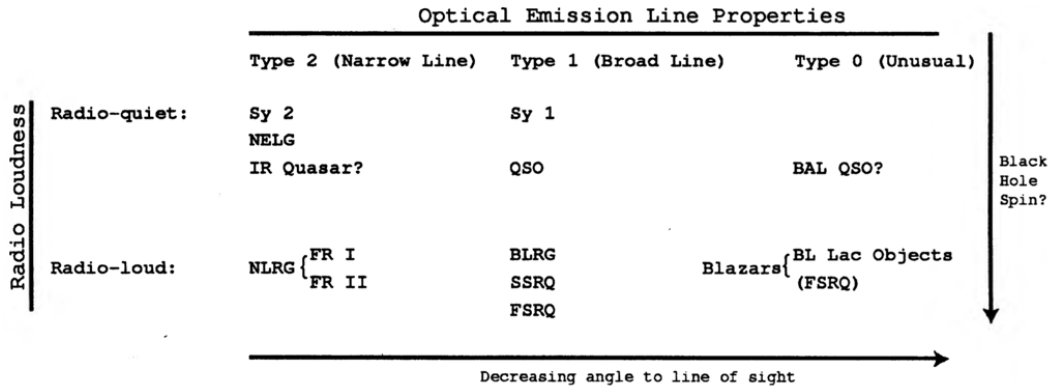
Figure 1.2: Observed optical properties of different types of AGN. Within each group, the AGN are listed by increasing luminosity. Taken from Urry & Padovani (1995).

results in only narrow optical emission lines, and weak continuum emission.

2. Type 2: AGN inclined further towards the jet, so that both the BLR and NLR are visible. Both strong broad and narrow emission lines, as well as bright continua can be observed.

3. Type 0: AGN at a small viewing angle, so that the AGN are being observed very close to the jet axis. In these systems, both the emission and absorption from the BLR and NLR are dominated by the strong, Doppler boosted continuum emission from the jet. The emission lines are therefore weak or undetectable in these systems.

The classifications based on these different optical properties are outlined in Fig. 1.2 and represented as a flowchart in Fig. 1.3. As can be seen in the figures, both radio-loud and radio-quiet AGN exist within these groups. Table 1.1 gives the full names of the acronyms used to classify AGN in Figs 1.2 and 1.3.
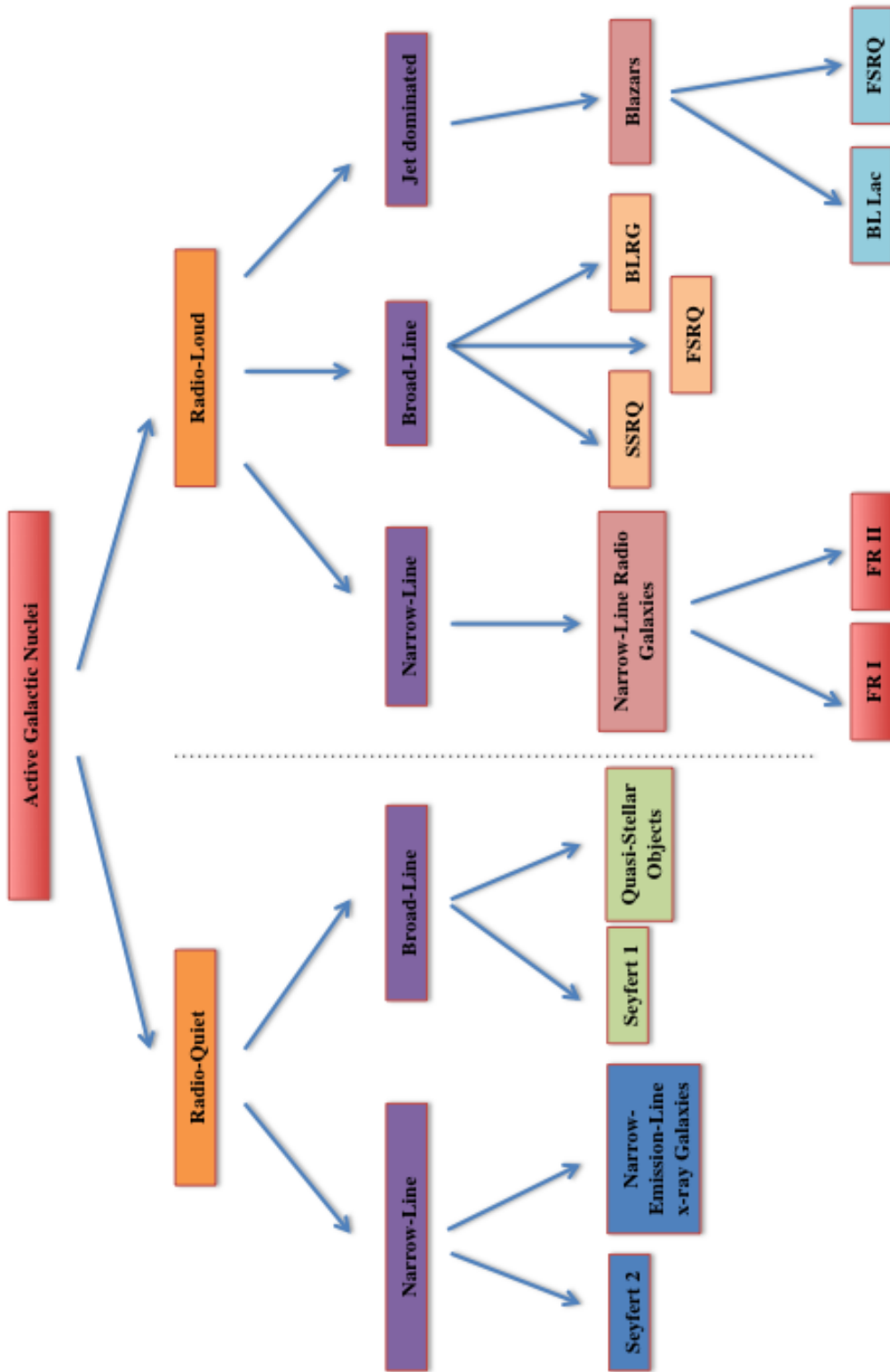
Figure 1.3: Flowchart of the AGN classification scheme, showing both radio-loud and radio-quiet AGN.

The focus of this work is on flat spectrum radio quasars, a subset of the radio-loud blazar class of AGN. Blazars are AGN in which the jet is oriented closely towards our line of sight, and are therefore classed as type 0 AGN. The effect of the direct orientation of blazars is that the observed emission is highly Doppler boosted, causing blazars to appear as some of the brightest objects in the γ-ray sky, particularly during flaring episodes (Abdo et al., 2011). Blazars are further split into two subclasses - BL Lacertae objects and flat spectrum radio quasars (Urry & Padovani, 1995). As can be seen from Fig. 1.2, FSRQs can be classified as either type 1 or type 0 AGN. This arises from the fact that AGN with the characteristic properties of FSRQs can also be found at small angles to the line of sight. In these cases, their continuum emission will resemble that of BL Lac objects, and they can be characterised by observations such as their rapid variability and superluminal cores. The distinction between FSRQs and BL Lac objects is based on the strength of the broad emission lines from the central engine. BL Lac objects have very weak or non-existent broad-lines, potentially due to a relatively low accretion rate onto the central SMBH (Ghisellini, 2010b).

The optical emission from blazars is often highly polisarised, and the emission all of the way across the electromagnetic spectrum is highly variable (Marscher et al., 2010). More than half of the γ-ray sources detected with the *Fermi*-Large Area Telescope (LAT) are AGN, with ~98% of these AGN being blazars (Ackermann et al., 2015).

1.2 Electromagnetic Radiation Emission Mechanisms

The relativistic jets of AGN emit radiation across the electromagnetic spectrum, with the energy of the photons being produced dependent on the emission mechanism.

In the case of radio-loud relativistic jets, such as those in FSRQs, radio emission is usually produced through synchrotron radiation. Synchrotron radiation is emitted from a charged particle when the particle is accelerated along a circular path in a magnetic field, illustrated in Fig. 1.4. A good candidate for the magnetic field structure around the jet is a toroidal magnetic field, with the magnetic field close to the SMBH thought to be particularly strong, sometimes referred to as the acceleration and collimation zone (Marscher et al., 2010). A suggestion for the jet structure close to the SMBH of the FSRQ PKS 1510-089 is shown in Fig. 1.5. This magnetic field accelerates the charged particles in a spiral path, producing the synchrotron radiation along a large portion of the length
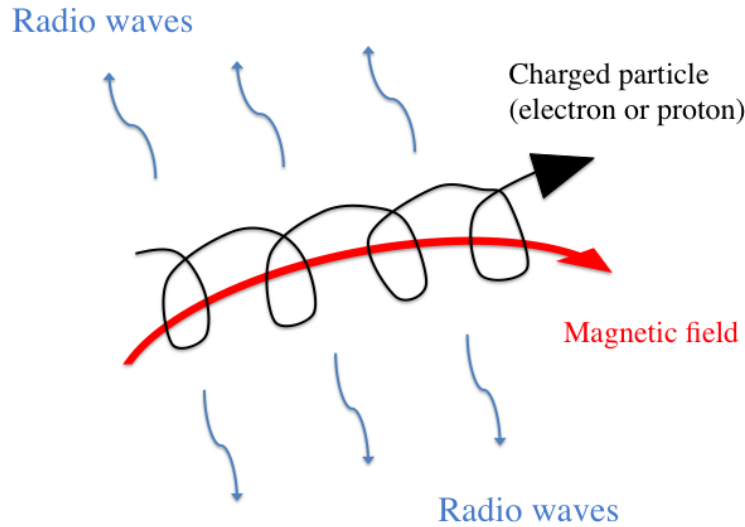
Figure 1.4: Illustration of radio emission being produced through synchrotron radiation.

of the jet.

In order to produce high energy photons such as γ-rays, a different emission mechanism needs to be employed. Although synchrotron emission is abundant in the jet, it does not contribute significantly towards γ-ray radiation. It would require an extremely strong magnetic field to accelerate the charged particle to energies high enough to produce a γ-ray, and it is therefore not likely that the synchrotron radiation from an FSRQ contributes significantly to emission at these energies. A mechanism that is believed to contribute significantly towards high energy emission is inverse-Compton scattering. Inverse-Compton (IC) scattering occurs when a low energy seed photon collides with a high energy relativistic particle, resulting in the photon gaining energy and the relativistic particle losing energy (Longair, 2011). Fig. 1.6 shows a schematic diagram of this scattering between a low energy photon and a relativistic electron, resulting in the photon being up-scattered to x-ray or γ-ray energies.

Alongside the increase in energy of the photon that arises from IC scattering, the loss of energy of the electron should also be noted. There are two regimes under which IC scattering can occur, depending on the total energy of the interaction. These regimes are Thomson scattering and Klein-Nishina (KN) scattering respectively. The way in which the photons gain energy, and therefore how the relativistic electrons lose energy or 'cool', differs between these two regimes. IC scattering occurs under the Thomson regime when
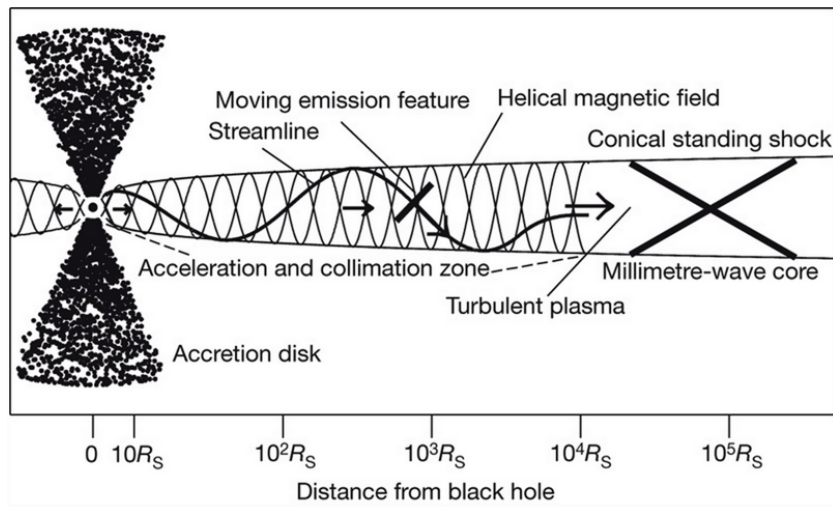
Figure 1.5: Diagram of the inner regions of PKS 1510-089, as an emission feature moves down the jet. A toroidal magnetic field can be seen. The region close to the SMBH is referred to as the acceleration and collimation zone, leading to the core of the jet. Taken from Marscher et al. (2010).
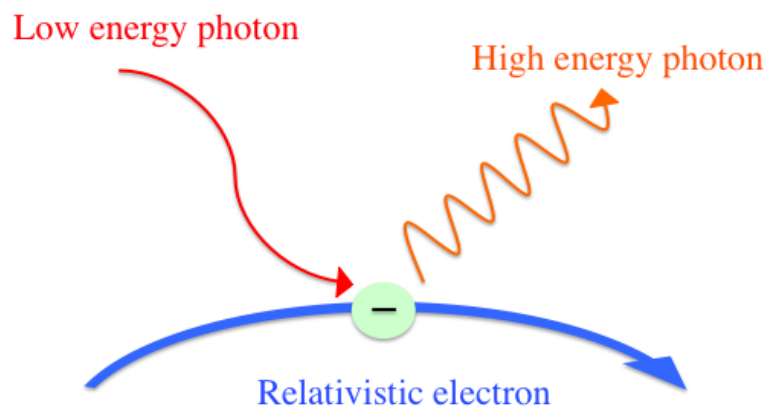
Figure 1.6: Illustration of high energy photons being emitted through inverse-Compton scattering.

$\gamma\epsilon_0 \ll 1$, where γ is the electron Lorentz factor and ϵ_0 is the seed photon energy, both measured in the same frame. On the other hand, IC scattering occurs under the Klein-Nishina regime when $\gamma\epsilon_0 \gg 1$, with the transition between the two regimes occurring at $\gamma\epsilon_0 \sim 1$ (Dotson et al., 2012). This means that for the same relativistic electron, the energy of the seed photon will dictate the scattering regime. In the Thomson regime, the final energy of the photon after scattering, ϵ_1, is (Blumenthal & Gould, 1970):

$$\epsilon_1 = \frac{4}{3}\gamma^2\epsilon_0. \tag{1.2.1}$$

The resultant photon energy and therefore the energy loss rate of the electron is $\propto \gamma^2$. However, in terms of the electron cooling in the Thomson regime, each interaction between a photon and an electron results in the electron only losing a very small amount of its total energy. In the KN regime, the final energy of the photon and therefore the electron cooling rate is $\propto ln(\gamma)\epsilon_0$. Unlike the Thomson regime, each scattering in the KN regime results in the electron losing a significant fraction of its energy (Blumenthal & Gould, 1970). How these differences in the electron cooling can be used to localise the γ-ray emission region will be discussed in Chapter 4.

In terms of the origin of the interacting photons, there are two variations of IC scattering that should be considered within the jet of a blazar: external inverse-Compton scattering and synchrotron self-Compton (SSC) scattering. SSC scattering is the process of IC scattering between a relativistic particle within the jet and a synchrotron photon that is also produced within the jet. Observing a large increase in synchrotron radio emission quasi-simultaneously with an increase in γ-ray emission can therefore be used an as indicator that SSC is a likely γ-ray emission process. The dominant mode of producing γ-rays within BL Lac objects is thought to be SSC (Ghisellini et al., 2010a).

On the other hand, the seed photons for external IC scattering are the ambient photons around the jet, i.e. external to the jet. Broadband spectral energy distribution (SED) modelling has shown that in the case of FSRQs, modelling the γ-ray emission as being produced by leptonic external IC scattering fits the observed spectra well. There is little need for SSC contributions to the spectra, nor a hadronic model of IC scattering in which the interaction would occur between a relativistic proton and a low energy photon (Ghisellini et al., 2010a). The origin of the seed photons for external IC in FSRQs is an exciting and growing area of high energy astrophysics research. Deducing whether the seed photons are likely to be optical and ultraviolet (UV) ambient photons from close to

the base of the jet and the BLR, or whether they are lower energy infrared (IR) ambient photons from further downstream of the SMBH can be used as a method of constraining the location of the γ-ray emission region.

Fig. 1.7 shows the SED of the flat spectrum radio quasar 3C 454.3. As is typical of blazar SEDs, two distinct peaks can be identified. The first peak is at low energy, and can be attributed to synchrotron radiation for both FSRQs and BL Lacs. The high energy part of the spectrum peaks at γ-ray energies, associated with external IC scattering in this case, as 3C 454.3 is an FSRQ. If the SED of a BL Lac was constructed, the second peak would be attributed to SSC. Intermediate energies such as the x-ray contribution shown in Fig. 1.7 have been shown to arise from a combination of scattering mechanisms, such as both SSC and external IC (e.g. Ghisellini et al. 2010a).

1.3 Localising the γ-ray Emission Region

The motivation behind this work is to gain a better understanding of the energetics of relativistic jets in FSRQs, and therefore of AGN themselves. As γ-ray emission is produced by energetic particles that are accelerated within the jet, the location at which the γ-ray emission is produced gives an indication of where the relativistic particles are being most strongly accelerated. The traditional view is that the most energetic part of the jet, where the plasma is most accelerated, is close to the SMBH. If γ-ray emission from an FSRQ was to be located significantly further out from the SMBH, it would be an indication that this region was also very energetic, and that the jet may not simply decrease in power with distance from the SMBH. It would also be interesting to discuss whether or not the location of the γ-ray emission region varies between FSRQs, thus being a property of the individual jets. On the other hand, the location of the emission region may also vary between flares from one source.

Despite the volume of γ-ray data that can be collected by both the *Fermi*-LAT and ground-based instruments, the emission cannot be spatially resolved for the majority of AGN. The process of locating the γ-ray emission region in an AGN is therefore indirect, and many different methods have previously been employed. As discussed in Section 1.2, the γ-ray emission from FSRQs is likely to be produced by external IC scattering. The emission region is modelled as a spherical, moving region of energetic electrons that will interact with the relevant seed photons (Ghisellini et al., 2010a). Although the processes
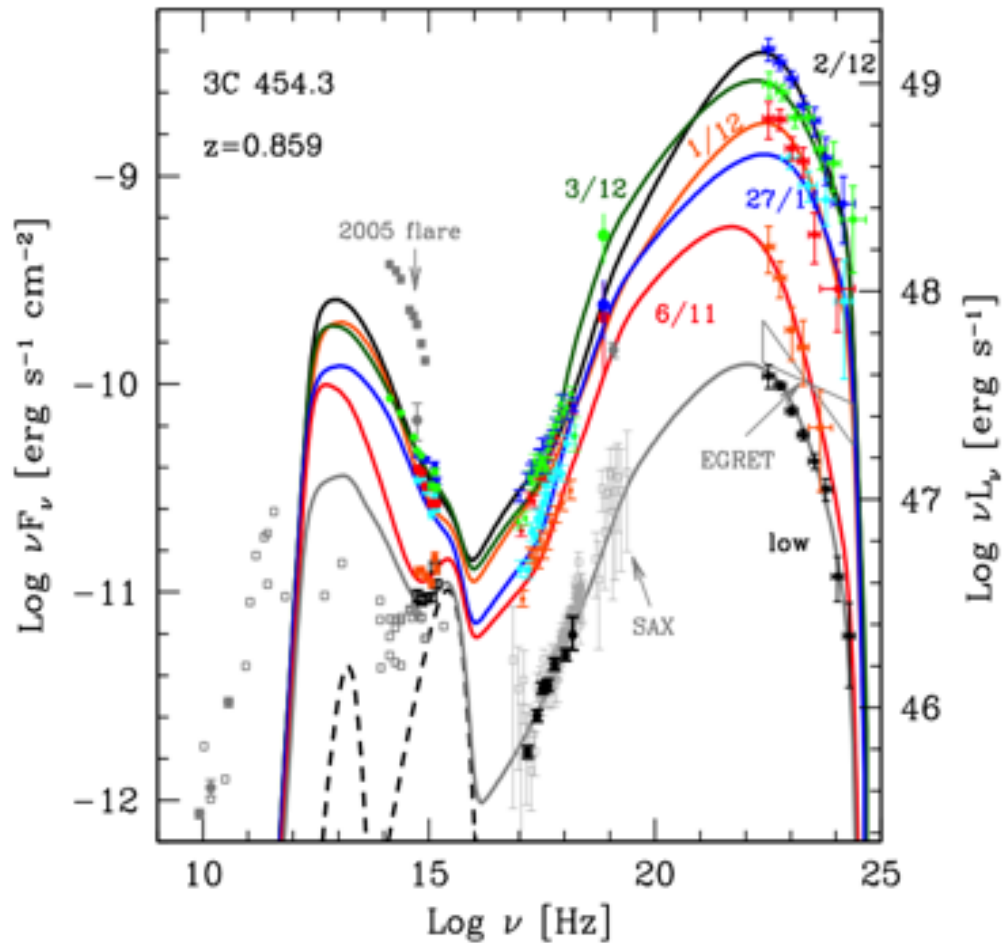
Figure 1.7: The SED of 3C 454.3 at 5 epochs: 6 and 27 Nov. 2009, 1, 2, and 3 Dec. 2009. The SEDs are labelled with the dates. The result of the modelling by Bonnoli et al. (2011) is also shown, including the accretion disk component, the x-ray corona contribution and the IR emission from the torus (dashed black lines). Archival data is shown in light grey, including the optical fluxes achieved during the 2005 optical flare, the 5-6 June 2000 BeppoSAX spectrum (Tavecchio et al., 2002) and the EGRET spectrum of Jan 1992 (Nandikotkur et al., 2007). Taken from Bonnoli et al. (2011).

occurring within the jet are not well understood, it's possible that the emission region is an over-density of plasma caused by passing through a standing shock in the jet, or through the injection of plasma into the jet.

As discussed, the origin of the γ-ray emission from blazars has traditionally been assumed to be close to the central SMBH. This conclusion is based in part on the results of spectral energy distribution modelling (e.g. Ghisellini et al. 2010a; Nalewajko et al. 2012), as well as the compact size of the emission region inferred from observations of rapid γ-ray variability (Tavecchio et al., 2010). Using the size of the emission region to infer its location rests on the assumption of a constant jet geometry as well as the assumption that the γ-ray emission region covers the full cross-section of the jet. This implies that the size of the emission region, R, is related to the distance from the SMBH, r, and constant opening angle, Ψ, by $r \sim R/\Psi$ (Dermer et al., 2009; Ghisellini & Tavecchio, 2009).

There are, however, studies that have concluded a MT or parsec-scale origin for the γ-ray emission from blazars (Lahteenmaki & Valtaoja, 2003; Marscher et al., 2010; Agudo et al., 2011; Jorstad et al., 2010, 2013). Multi-wavelength (MWL) studies of blazars have resolved outbursts in radio emission on a parsec-scale from the SMBH, and simultaneous flares in the γ-ray regime suggest a common origin for the γ-ray emission (Marscher et al., 2010). The presence of significant very high energy (VHE) emission from blazars also supports the inference that the emission region is not located within the broad-line region, and this will be discussed in Chapter 4 (Donea & Protheroe, 2003; Liu & Bai, 2006). The possibility of multiple emission regions has also recently been suggested, based on γ-ray observations (e.g. Brown 2013).

Chapter 2

The Fermi-Large Area Telescope

2.1 Gamma-ray Astronomy

Gamma-ray astronomy is the study of the highest energy photons emitted from astronomical sources. The lowest energy of γ-ray photons is often considered to be the rest mass energy of an electron or positron, ~511 keV, as γ-rays can be produced through electron-positron annihilation. However, the term high energy γ-rays usually refers to photons at MeV energies or higher, and the study of these γ-rays is the focus of this thesis. γ-ray astronomy is a relatively young branch of astronomy, with observations starting to become possible in the 1960s. The first γ-ray telescope was on-board on the Explorer XI satellite in 1961 (Kraushaar & Clark, 1962), and many ground- and space-based γ-ray detectors have been put into operation in the years since. The first satellite to provide a complete map of the entire γ-ray sky was the COS-B satellite, launched in 1975 (Bennet, 1990). Another ground-breaking γ-ray observatory was the Compton Gamma Ray Observatory (CGRO) launched in 1991 (Kniffen, 1989), the second of NASA's great observatories. Unlike Explorer XI and COS-B, the CGRO hosted a total of four instruments, reaching a sensitivity of greater than an order of magnitude over previous instruments. The most sensitive γ-ray satellite currently in operation is the *Fermi* satellite, discussed in Section 2.2. The data collected by *Fermi* complements the Very High Energy γ-ray data collected by the present generation of ground-based imaging atmospheric Cherenkov telescopes, namely H.E.S.S., MAGIC and VERITAS.

Both Galactic and extragalactic sources of γ-rays have been observed. A large amount of diffuse γ-ray emission is detected along the Galactic plane, as high energy cosmic rays interact with the interstellar medium (ISM). Galactic point sources include pulsar wind nebulae, supernova shell remnants and binary systems such as cataclysmic variables (Acero et al., 2015). The dominant sources of extragalactic γ-rays are the compact cores

Figure 2.1: The radio galaxy Centaurus A. Gamma-rays from the *Fermi*-Large Area Telescope are shown in purple, radio emission is shown in orange, and the visible light is also shown. Image credit: NASA/DOE/Fermi LAT Collaboration, Capella Observatory, Ilana Feain, Tim Cornwell, Ron Ekers (CSIRO/ATNF), R. Morganti (ASTRON) and N. Junkes (MPIfR).

of some galaxies known as active galactic nuclei, discussed in Section 1.1. Despite the advances in γ-ray detection technology, it is not possible to resolve the emission from distant sources such as AGN. An exception to this is the nearby radio galaxy Centaurus A shown in Fig. 2.1. From this galaxy, the *Fermi*-Large Area Telescope has resolved γ-ray emission originating in both the core and the radio lobes of the AGN, either side of the central engine (Abdo et al., 2010a).

2.2   The *Fermi*-Large Area Telescope

Thanks to the launch of the *Fermi* Gamma-ray Space Telescope in June 2008, >7 years of γ-ray data from both Galactic and extragalactic sources are publicly available. There are two detectors on-board *Fermi* - the Large Area Telescope and the Gamma-ray Burst Monitor (GBM). The LAT detector is the primary detector, in that its science objectives

are broader than those of the GBM, and that it usually operates in all-sky survey mode in order to collect data from all sources in the γ-ray sky. The *Fermi*-LAT can also perform in a pointed observations mode, in case of events such as γ-ray bursts (GRBs) or exceptional flares that are of particular interest. The satellite before launch is shown in Fig. 2.2. It is now in a near-earth orbit, and is powered by solar power. The original design lifetime of the satellite was five years, and since reaching that goal in 2013, *Fermi* has entered an extended period of observations that is expected to finish in 2018. The *Fermi*-LAT aims to provide insight into a plethora of questions including the physics behind relativistic jets of AGN, what comprises Dark Matter, the origin of cosmic rays and many more long-standing questions about the high-energy Universe.

The objective of the GBM is to observe GRBs at much lower energies than the LAT, complemented by the LAT's observations. The GBM detects photons at energies ~8 keV$\leq$ $E_\gamma \leq 40$ MeV. This energy range spans both x-ray photons and low energy γ-rays, and helps to give a more complete picture of GRBs than high energy γ-ray data alone. The GBM also allows the position of GRBs to be reported so that the LAT may be re-pointed at a GRB, in the cases where the LAT is observing in all-sky survey mode (Meegan et al., 2009).

The *Fermi*-LAT on the other hand detects photons between energies 20 MeV $\leq E_\gamma \leq 1$ TeV, although a subset of this energy range can be specified during the data selection stage of analysis. The on-axis effective area of the LAT at 1 GeV is ~700-820 cm^2, depending on the instrument response function (IRF) used. IRFs will be discussed in more detail in Section 2.3.2. The LAT detector has a wide field of view, covering ~20% of the sky at any one time. The *Fermi* satellite itself completes two orbits in ~3 hours, scanning the entire sky almost uniformly in this short time (Atwood et al., 2009). This allows a wealth of information to be collected, observing the entire γ-ray sky unbiased by activity state. In terms of localising the γ-ray emission region of blazars, this means that γ-ray data are collected both during bright flares and also when the source is not in an unusual activity state, allowing interesting comparisons to be made between the two states.

The point spread function (PSF) of a detected γ-ray depends on the energy of the photon, due to differences in the photon scattering within the detector. The 68% containment angle for γ-rays ranges from ~6° for 0.1 GeV photons to ~0.2° for 100 GeV photons for the Pass7 Reprocessed instrument response function (Atwood et al., 2009; Ackermann et al., 2012), shown in Fig. 2.3.

Figure 2.2: The *Fermi* satellite, shortly before being launched into space. One of the solar panels can be seen folded onto the side of the spacecraft. Image credit: NASA/DOE/Fermi LAT Collaboration.
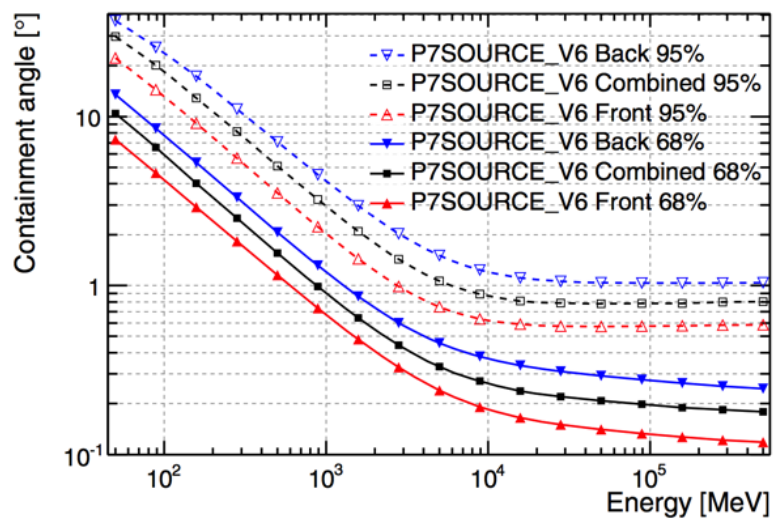
Figure 2.3: The 68% and 95% containment angles as a function of energy for the P7SOURCE_V6 IRF. The black lines show the containment angles for the combined photon data. Taken from Ackermann et al. (2012).
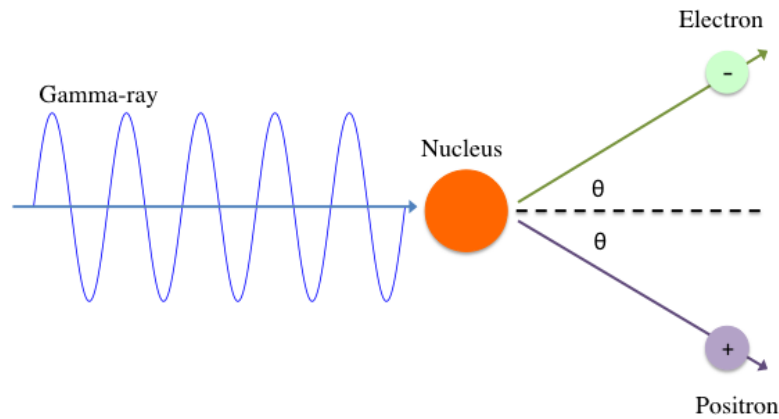
Figure 2.4: A high energy γ-ray being converted into an electron-positron pair in the proximity of an atomic nucleus.

The high energy of γ-ray photons means that the photons cannot be reflected or refracted, and cannot therefore be focused onto a detector as they would if they were lower energy photons. A γ-ray telescope therefore detects photons using a different method, and in the case of the *Fermi*-LAT the telescope is a pair conversion telescope.

The γ-ray detection method of the *Fermi*-LAT requires an understanding of the interactions between γ-rays and matter. The primary mode of interaction between matter and photons depends on the energy of the photon. For the highest energy γ-rays, the process of pair production should be considered. Pair production can occur in two situations. The first is when a high energy γ-ray comes into close proximity with an atomic nucleus. The energy of the photon, and therefore the γ-ray itself, is converted into the electron-positron pair through Einstein's equation $E = mc^2$ (Longair, 2011). The nucleus will receive some recoil in order to conserve momentum. This is pictured in Fig. 2.4.

The second situation in which pair production occurs is when a high energy γ-ray interacts with a lower energy photon, for example an optical or IR photon:

$$\gamma\gamma \rightarrow e^+ e^-. \tag{2.2.1}$$

The total energy of the two photons must be enough to create the electron-positron pair. This process will be discussed in the context of locating the emission region of γ-rays in Chapter 4.

Fig. 2.5 shows the principle of operation of a pair conversion telescope, such as that on-board the *Fermi* satellite. There are 3 primary components that comprise the detector (Atwood et al., 2009):
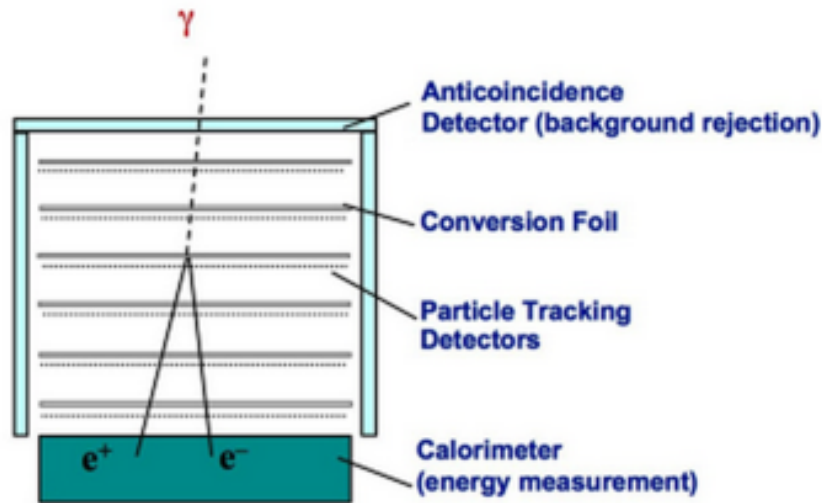
Figure 2.5: Operation of a pair conversion telescope, on-board the Large Area Telescope instrument. Image credit: The *Fermi* Collaboration.

1. The plastic anticoincidence detector.

2. The precision converter-tracker (tungsten foil converter layers and silicon detector layers).

3. The calorimeter.

When a γ-ray hits the LAT, it first comes into contact with a plastic anticoincidence detector. This anticoincidence detector is a scintillator, meaning that a photon will pass freely through it. However, if a charged particle such as a cosmic ray was to hit the LAT, a flash of light would be produced in the anticoincidence detector. This information allows a distinction to be made between photons and charged high energy particles such as cosmic rays (Moiseev et al., 2007), and is ~99.7% efficient at identifying unwanted charged particles (Atwood et al., 2009). As the γ-ray continues to travel, it is next incident on a thin metal tungsten layer. The γ-ray will interact preferentially with this tungsten layer to create an electron-positron pair, through the pair production process described previously. This tungsten layer is the 'converter' of the converter-tracker sub-detector. The electron and positron both continue to travel through the LAT, coming into contact with many silicon semiconductor detector 'tracker' layers, as shown in Fig. 2.5. Each silicon layer is also interleaved with a tungsten layer, to ensure that the pair production process occurs before the γ-ray finishes travelling through the detector (Atwood et al., 2007). The interactions of the e^-e^+ pair with the silicon layers allow the LAT to track
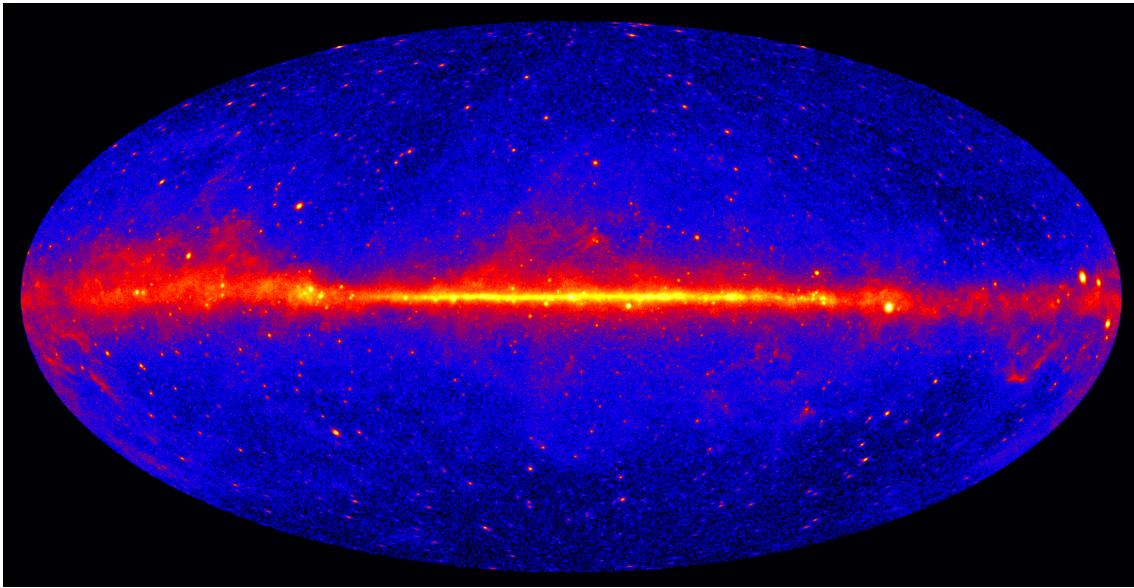
Figure 2.6: The γ-ray sky as seen by *Fermi*, with 5 years of data at $E_\gamma \geq 1$ GeV. Image credit: The *Fermi* collaboration.

the path that the pair takes through the detector. The converter-tracker also uses both the pair production signature and the path that the pair takes through the tracker layers to identify background charged cosmic rays and pair production induced by showers. Finally, the pair reaches the caesium iodide calorimeter at the bottom of the detector. The calorimeter measures the energy deposited by the electron and positron (Johnson et al., 1997). The shower deposition profile measured by the calorimeter also assists in the task of identifying background events.

In order to combine all of the information from the above sub-detectors, the *Fermi*-LAT has a Data Acquisition System (DAQ) on-board, made from specialized electronics and microprocessors. The sub-detectors on-board the LAT self-trigger on the detection of events, prompting the DAQ to collect and process the event data. The DAQ uses the information from the anticoicindence detector, converter-tracker and calorimeter to distinguish between γ-rays and unwanted cosmic rays or background events. It also uses the information from the converter-tracker and the calorimeter to reconstruct the direction and energy of the incident γ-ray. This is done using filtering algorithms that are performed on-board *Fermi*. The DAQ can then also filter out unwanted γ-rays if they have originated from the Earth's atmosphere, based on their arrival direction. The appropriate γ-ray event data is then sent back to the ground, with the number of background events having been minimised. The DAQ also performs tasks such as the instrument control and monitoring, and searching for transient events (Atwood et al., 2009).

Fig. 2.6 shows the results of five years of *Fermi*-LAT scanning the entire sky, at $E_\gamma \geq 1$ GeV. Along the centre of the sky the Galactic plane can be seen, including large amounts of diffuse emission. Off the Galactic plane, many bright point sources can be seen, which are predominantly AGN.

2.3   Event Classes and Instrument Response Functions

2.3.1   Event Classes

A photon 'event' is a description of a single detection by the LAT. In addition to the reconstruction of events from the raw LAT data in terms of the photon energy and arrival direction, the event is also given a classification. The reconstructed events are analysed in order to determine the accuracy of the reconstructed photon energy and direction, and the event classification is based on the probability that the photon is a γ-ray. Event classes for point source events include 'SOURCE', 'CLEAN' and 'ULTRACLEAN'. The event classes are hierarchical, with the events within each class having an increasing probability of being a non-background γ-ray (Atwood et al., 2009).

2.3.2   IRFs

The *Fermi*-LAT instrument response function is the tool that maps the detected photon events to the photon flux. The IRFs describe the performance of the LAT as a function of photon energy and incidence angle, as well as additional parameters. IRFs are calculated using Monte Carlo simulations of large numbers of γ-ray events (Atwood et al., 2009; Ackermann et al., 2012). The IRF is then given by a comparison of the properties of the simulated events within a given event class to the input photons.

An example of the performance described by the IRF is the PSF. The PSF of the LAT varies depending on the IRF used to analyse the LAT data. The aim is to continuously improve the way in which the LAT data is processed, using modified reconstruction algorithms. The analysis in this thesis uses both the P7_REP_V15 IRF and the P8R2_SOURCE_V6 IRF. This is because P8R2_SOURCE_V6 was released during the writing of this thesis. The above IRFs are both appropriate for 'SOURCE' class events. The 'P7' and 'P8' in these IRF names refer to the 'Pass7' and 'Pass8' *Fermi* data releases respectively.

P8R2_SOURCE_V6 shows a number of significant advances over P7_REP_V15, with

each sub-detector undergoing improvements. Details of this can be found in Atwood et al. (2012). For example, in the Pass8 IRF, the algorithm used to track the path of the e^-e^+ pair has been completely reworked. This was done in order to reduce the number of γ-rays that are misclassified as background cosmic rays, reduce the number of events that migrate to the outer edges of the photon PSF and reduce the number of events that cannot be reconstructed at all. Tests of the new approach to tracking show that the new tracker pattern recognition can significantly reduce the number of events that are mis-tracked, as well as giving a smaller PSF at high energies (Atwood et al., 2012). The new approach also enables a ~25% greater high energy acceptance (the effective area integrated over the solid angle).

The way in which the calorimeter operates has also been modified. An issue that was dominating the LAT's performance before Pass8 was the presence of 'ghost' signals. In the cases where a particle had passed through the LAT a few μ*s* before the particle of interest that triggered an event, remnants of the electronic signals and track of the unwanted particle through the detector were being recorded as part of the event. This was affecting all subsystems, complicating the γ-ray direction reconstruction and analysis, causing some γ-rays to be wrongly rejected as background cosmic rays, and affecting the ability of the calorimeter to accurately calculate the energy of the γ-ray. The new approach to calorimeter operation aims to identify ghost signals, and recover the effective area for γ-rays that was previously lost when a ghost signal was present. It was been shown that there is a ~5-10% increase in the effective area at $E_\gamma = 1$ GeV, increasing with decreasing photon energy (Atwood et al., 2012).

The energy resolution in the calorimeter has also been improved such that the Pass8 *Fermi* tools allow detection and analysis of photon energies up to $E_\gamma = 1$ TeV, whilst the P7_REP_V15 IRF only allows up to $E_\gamma = 300$ GeV.

Chapter 3

Source Selection and Basic Analysis

3.1 Source Selection

In order to locate the origin of γ-ray emission from FSRQs, the γ-ray emission characteristics need to be examined in the greatest level of detail possible. The primary consideration for choosing suitable sources is therefore the photon statistics of the emission.

Although accurate analysis can be achieved with lower photon statistics, a large number of photons is required in order to get the best temporal resolution. Being able to identify how the emission characteristics change on short timescales reveals substructures within more prominent changes in the emission, and the way in which this can be used to locate the emission region is discussed in Section 4.2. Good photon statistics allow for much more reliable γ-ray spectral parameters to be calculated, as there is less uncertainty in the shape of the spectra at high energies. There may also be less uncertainty on the γ-ray flux when a larger number of photons is detected.

It was considered that the amount of γ-ray contamination from neighbouring sources should be minimised. This would be achieved by not studying FSRQs that are close to the Galactic plane, where possible. The Galactic plane is a crowded region of γ-ray emitters, as can clearly be seen in Fig. 2.6. As discussed in Chapter 2, the PSF of photons detected by the *Fermi*-LAT (hereafter *Fermi*) is relatively large, and a crowded region makes the risk of associating photons and therefore a flux with the wrong source much greater. However, it was decided that this should not be a primary consideration, given the capabilities of the *Fermi* tools.

FSRQs are therefore studied when the γ-ray emission is at a heightened level, as the largest number of photons are detected in these periods and the best statistics with which to study the emission characteristics exist. The first step of the source selection is then to

identify FSRQs that have undergone periods of very high γ-ray activity, or 'flares'. The brighter the γ-ray flux from the sources that are studied, the greater the photon statistics are. The redshift of the source will also contribute towards how bright an FSRQ appears when detected, due to the absorption of γ-rays by the extragalactic background light (EBL). The EBL is comprised of IR, optical and ultraviolet photons, being emitted in the optical and UV by stars and galaxies since the epoch of reionization (Dube et al., 1977; Aharonian, 2001; Hauser & Dwek, 2001). Some of this light has since been absorbed by AGN as well as by interstellar gas and dust, and so has been re-emitted in the IR. The low energy photons of the EBL can therefore absorb high energy γ-rays as they travel through the Universe, leading to $e^- e^+$ pair production as described in Section 2.2. This is why the brightest FSRQs detected by *Fermi* do not tend to have redshift $z > 2.5$, as seen in Table 3.1. The absorption by the EBL therefore also has the potential to intrinsically affect the high energy part of the γ-ray spectrum that is calculated using the photons detected by *Fermi*.

Table 3.1 shows the position on the sky, redshift and recent flares of the first selection of FSRQs that were considered for this thesis. These FSRQs were chosen primarily based on the brightness of the γ-ray flares that they had undergone, and how recently the flare had taken place. It was decided that γ-ray flares that were either previously unstudied or less extensively studied would be the most suitable selections for analysis, so that the work in this thesis might contribute new material towards the growing body of work on localising the γ-ray emission region in blazars. Sources that had flared in the last 1-2 years were therefore preferable. All of the sources presented are 'LAT Monitored Sources[1]', and the information on the flares reported in Table 3.1 has been taken from the Astronomer's Telegram and the *Fermi* monitored source list daily binned light curves.

---

[1]http://fermi.gsfc.nasa.gov/ssc/data/access/lat/msl_lc/

FSRQ	z	RA	Dec	Brightest ×10⁻⁶	Date	Index	l	b	2nd brightest ×10⁻⁶	Date	3rd brightest ×10⁻⁶	Date
		(h m s)	(d m s)	(ph cm⁻² s⁻¹)	(MJD)	(Γ)	(°)	(°)	(ph cm⁻² s⁻¹)	(MJD)	(ph cm⁻² s⁻¹)	(MJD)
3C 273	0.158	12 29 09.0	+02 03 04.8	9.2	55063	2.52	289.98	64.35	4.9	55180	4.7	55230
PKS 1510-089	0.36	15 12 51.0	-09 06 00.9	16	55853	2.30	351.29	40.14	6.7	54900	6.5	56600
PKS 0507+17	0.416	05 10 05.9	+18 00 41.7	4.5	56403	2.41	184.72	-12.76				
PKS B1222+216	0.434	12 24 54.3	+21 22 46.9	13	55365	2.19	255.06	81.66	6.0	56950	3.5	56689
3C 279	0.536	12 56 09.9	-05 47 28.0	16	57187	2.23	305.09	57.06	7.0	56740	3.6	55660
PKS 1622-253	0.786	16 25 46.8	-25 27 20.0	3.0	56571	2.23	352.14	16.32	2.5	55760		
NRAO 190	0.844	04 42 38.8	-00 17 56.0	3.0	56464	2.50	197.20	-28.46	1.4	54950	1.2	54820
3C 454.3	0.859	22 54 00.4	+16 08 45.0	66	55516	1.63	86.12	-38.19	23	55150	15	56850
PKS 0502+049	0.954	05 05 22.4	+04 59 52.0	3.5	56894	2.46	195.47	-20.86	2.5	57100		
CTA 102	1.037	22 32 33.4	+11 43 13.0	6.2	56188	2.34	77.42	-38.58	4.0	55700	3.3	56400
PKS 0402-362	1.417	04 03 58.5	-36 04 38.0	6.5	55826	2.72	237.73	-48.47	1.9	55250	1.4	56000
PKS 1424-41	1.522	14 27 57.9	-42 06 38.0	3.2	56298	2.08	321.45	17.26	2.5	55320	1.9	55700
PKS 1633+382	1.813	16 35 14.9	+38 09 09.0	2.7	55689	2.41	61.11	42.34	2.7	56500	2.0	56250
NRAO 676	1.899	22 01 44.1	+50 47 59.0	4.6	56094	2.59	97.64	-3.55	2.4	56250	2.2	56370
PKS 1329-049	2.15	13 32 03.6	-05 08 51.0	4.5	55449	2.45	321.36	56.26	1.8	55100		
S5 0836+71	2.218	08 41 29.4	+70 53 50.0	5.3	57236	2.62	143.54	34.43	3.0	55900	1.0	56850
PKS 2149-306	2.345	21 51 48.6	-30 25 43.0	2.9	56296	2.6	17.13	-50.76	0.6	57110		
PKS 1830-211	2.507	18 33 38.6	-21 03 25.0	7.5	55483	2.35	12.17	-5.71	3.2	55580	2.6	56150

Table 3.1: Properties of a selection of FSRQs that were considered for analysis. The fluxes presented are daily fluxes and their values and dates are preliminary, based on the announcements in the Astronomer's Telegram and the preliminary fluxes given in the *Fermi* monitored source list light curves. The Astronomer's Telegrams announcing the brightest flares given above are as follows: 3C273: Bastieri (2009), PKS 1510-089: Hungwe (2011), PKS 0507+17: D'Ammando (2013b), PKS B1222+216: Iafrate (2010) 3C279: Cutini (2015), PKS 1622-253: Carpenter (2013), NRAO 190: Buson & Gasparrini (2013), 3C 454.3: Sanchez & Escande (2010), PKS 0502+049: Ojha et al. (2014), CTA 102: Orienti & D'Ammando (2012), PKS 0402-362: D'Ammando (2011), PKS 1424-41: Ciprini & Cutini (2013), PKS 1633+382: Szosteck (2011), PKS 1329-049: Sokolvsky & Schinzel (2010), S5 0836+71: Ciprini (2015), PKS 2149-306: D'Ammando & Orienti (2013a), PKS 1830-211: Ciprini (2010), NRAO 676: Ciprini & Hays (2012).

Alongside the primarily considerations for selecting suitable γ-ray flares, it was also preferable to select FSRQs that had flared brightly on more than one occasion. This might mean that the sources had flares that had been previously studied, in addition to the flares that would be studied for this thesis. This would allow the previous results on the location of the emission region to be compared to the results found in this thesis. This comparison would give insight into whether or not the location of the emission region for the flare studied in this thesis was the same as the location for the previous flare. Long-term daily light curves were created for a subset of six FSRQs, chosen from Table 3.1 based on the considerations discussed. The FSRQs chosen were PKS 1510-089, PKS B1222+216, 3C 279, 3C 454.3, CTA 102 and PKS 1424-41. The data analysis procedure is described in Chapters 4 and 5. For all of the light curves except for 3C 279, the P7_REP_V15 IRF was used. For 3C 279, the P8R2_SOURCE_V6 IRF was used, as the timing of the flare coincided with the release of the Pass8 data. In all cases, photon events were filtered using an event class of 'SOURCE'. 'Source' class photons have an event class of 2 in the P7REP data, and an equivalent event class of 128 in the P8 data. These have a high probability of being a photon (Ackermann et al., 2012).

Figs 3.1 - 3.6 show the daily binned light curves of the subset of six FSRQs. They show the flux at energies $0.1 \leq E_\gamma \leq 300$ GeV.

The sources chosen for detailed study in this thesis were 3C 454.3 and 3C 279, the results of which are given in Chapters 4 and 5. As can be seen from Figs 3.1 - 3.6, 3C 454.3 and 3C 279 both strongly meet the requirements of having good photon statistics because of their exceptionally bright flares, which have taken place very recently. The rest of the sources, although bright, have not reached a daily binned γ-ray flux level of $F = 1 \times 10^{-5}$ ph cm^{-2} s^{-1} for previously unstudied flares. Both 3C 454.3 and 3C 279 do reach this high flux level for the flares studied in this thesis. Although somewhat arbitrary, reaching a flux of $F = 1 \times 10^{-5}$ ph cm^{-2} s^{-1} is relatively unusual, as can be seen from Figs 3.1 - 3.6, and will enable the most in-depth analysis to be done on the flares.
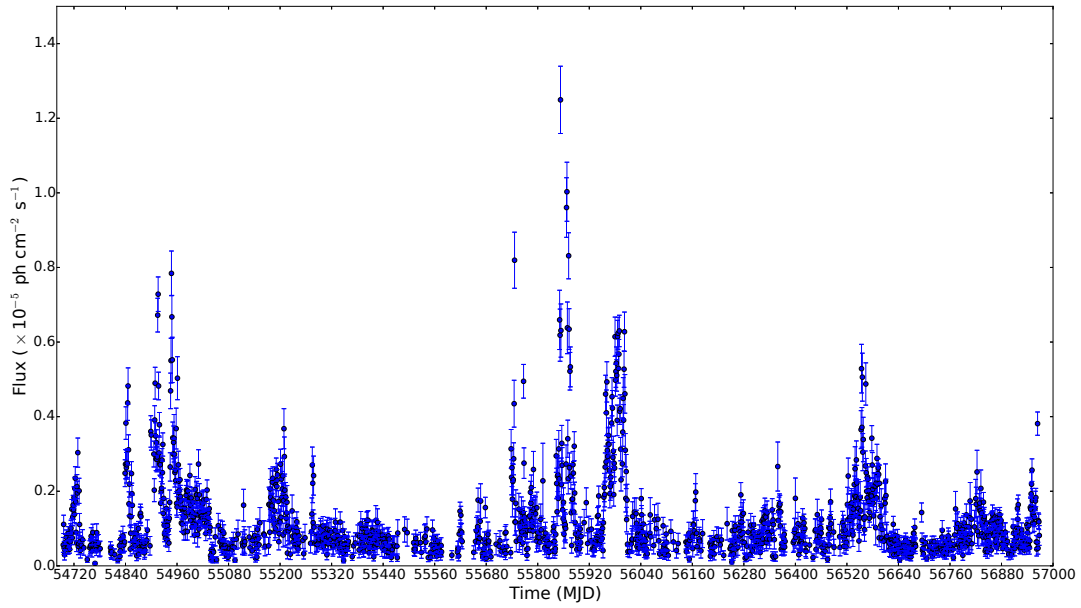
Figure 3.1: Daily binned $0.1 \leq E_\gamma \leq 300$ GeV light curve of PKS 1510-089, between MJD 54683 and 56986. Only data points with $TS \geq 10$ are shown.
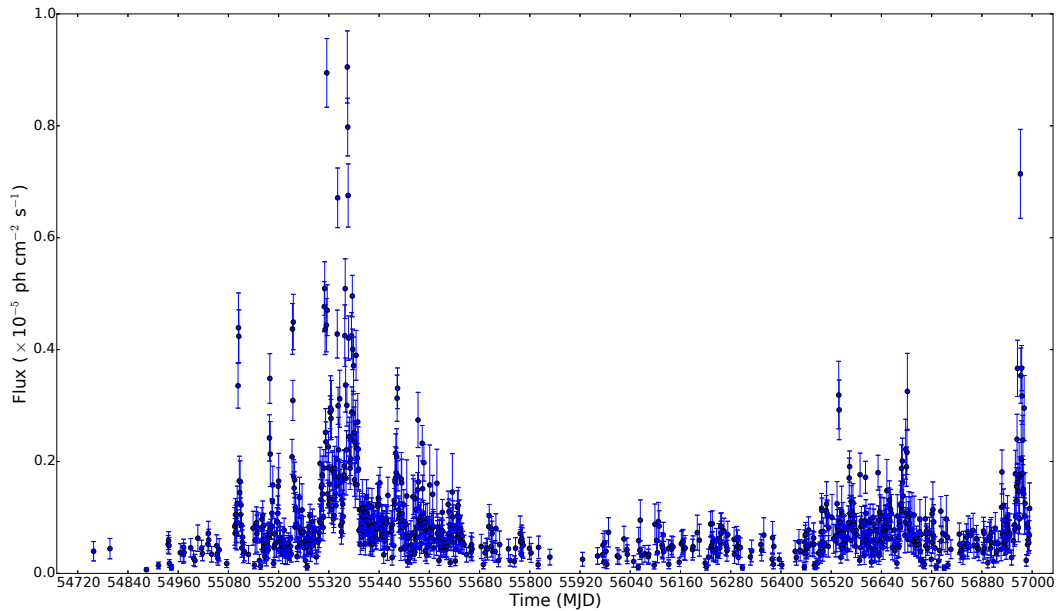
Figure 3.2: Daily binned $0.1 \leq E_\gamma \leq 300$ GeV light curve of PKS B1222+216, between MJD 54683 and 57000. Only data points with $TS \geq 10$ are shown.
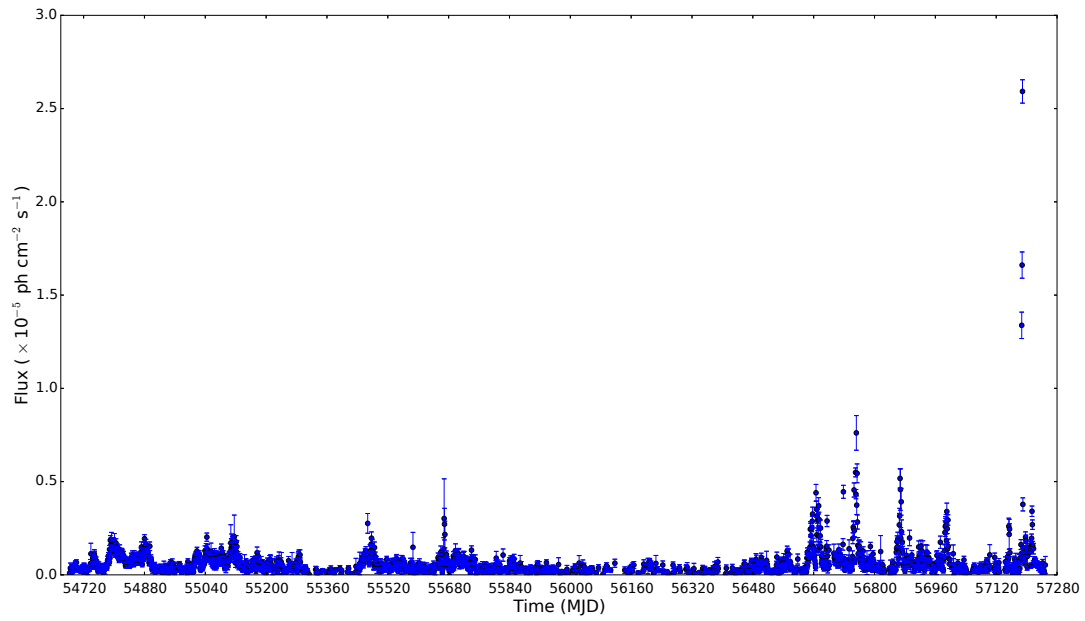
Figure 3.3: Daily binned $0.1 \leq E_\gamma \leq 300$ GeV light curve of 3C 279 between MJD 54683 and 57252. Only data points with $TS \geq 10$ are shown.
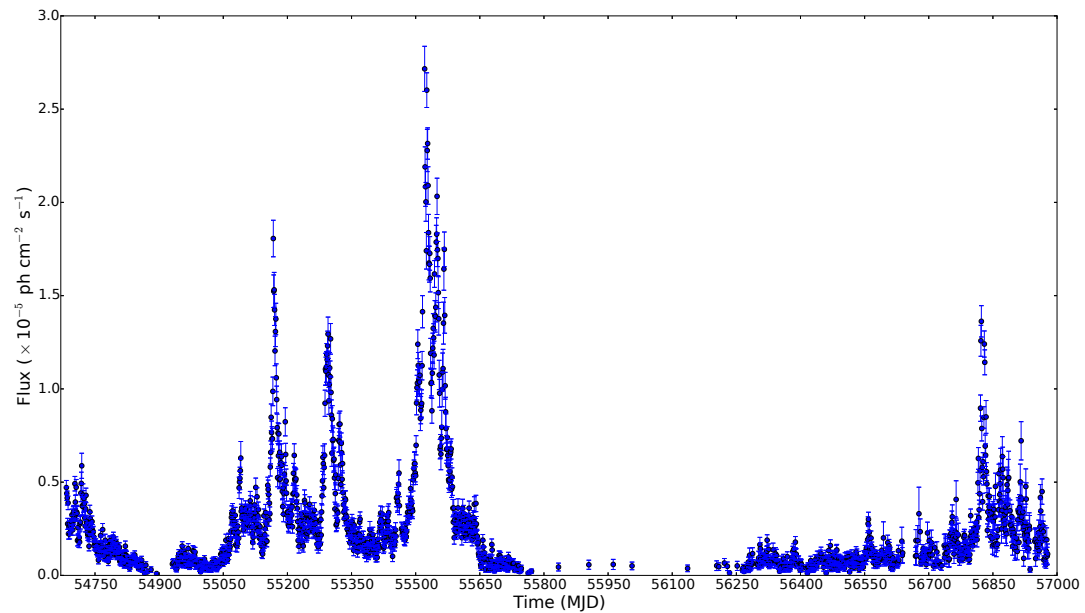
Figure 3.4: Daily binned $0.1 \leq E_\gamma \leq 300$ GeV light curve of 3C 454.3, between MJD 54683 and 56979. Only data points with $TS \geq 10$ are shown.
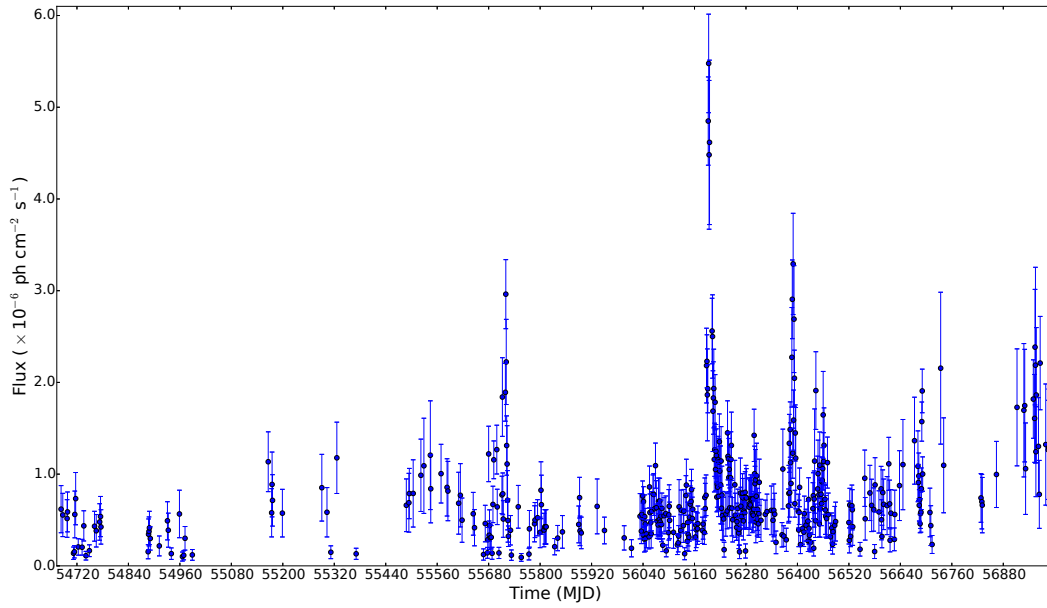
Figure 3.5: Daily binned $0.1 \leq E_\gamma \leq 300$ GeV light curve of CTA 102, between MJD 56483 and 56995. Only data points with $TS \geq 10$ are shown.
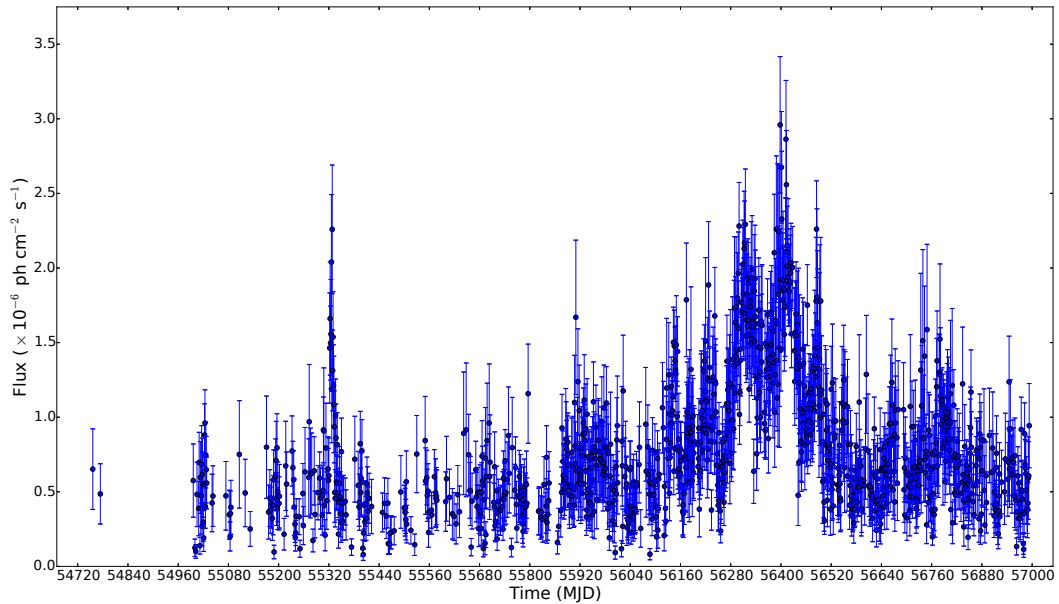
Figure 3.6: Daily binned $0.1 \leq E_\gamma \leq 300$ GeV light curve of PKS 1424-41, between MJD 56483 and 56999. Only data points with $TS \geq 10$ are shown.

Chapter 4

3C 454.3

The flat spectrum radio quasar 3C 454.3 can be found at a right ascension (hh mm ss.d) of 22 54 00.4, and a declination (dd mm ss.d) of +16 08 45.0. It is at a redshift of $z = 0.859$, a distance of approximately 11, 800, 000, 000 light years away. The discovery of 3C 454.3 was published by Bennett (1962), in the first revision of the third Cambridge (3C) catalog of radio sources, detected at 178 MHz. It was identified as being a γ-ray emitter by the the Energetic Gamma Ray Experiment Telescope (EGRET) on-board the CGRO, being published in the Second EGRET Catalog of High-Energy Gamma-Ray Sources (Thompson et al., 1995). Examples of observed SEDs of 3C 454.3 can be seen in Fig. 1.7.

3C 454.3 has been extraordinarily bright over the past decade. In December 2009, 3C 454.3 reached a record high energy γ-ray flux for blazars, with a daily flux of $F = (2.2 \pm 0.1) \times 10^{-5}$ ph cm^{-2} s^{-1} (Ackermann et al., 2010) and $F = (2.0 \pm 0.4) \times 10^{-5}$ ph cm^{-2} s^{-1} (Striani et al., 2010) measured by *Fermi* and Astro Rivelatore Gamma a Immagini LEggero (AGILE) (Tavani et al., 2009) respectively. It flared spectacularly again in November 2010, becoming brighter than even the Galactic Vela pulsar. The daily flux measured for this flare peaked at $F = (6.6 \pm 0.2) \times 10^{-5}$ ph cm^{-2} s^{-1} (Abdo et al., 2011), with a flux of $F = (6.8 \pm 1.0) \times 10^{-5}$ ph cm^{-2} s^{-1} detected on a timescale of ~12 h (Vercellone et al., 2011). The analysis in 3 hour time bins revealed that the flux reached $F = (8.5 \pm 0.5) \times 10^{-5}$ ph cm^{-2} s^{-1} on Modified Julian Date (MJD) 55520 (Abdo et al., 2011). These high flux levels have enabled extensive analysis to be done on the γ-ray characteristics of 3C 454.3, and the γ-ray emission has been suggested to originate both from the BLR and on parsec-scale distances from the SMBH (e.g. Ackermann et al. 2010; Tavecchio et al. 2010; Vercellone et al. 2010, 2011; Abdo et al. 2011; Bonnoli et al. 2011; Jorstad et al. 2013; Vittorini et al. 2014). 3C 454.3 has also been seen to flare brightly in the optical and radio (Villata et al., 2007; Raiteri et al., 2008; Hagen-Thorn et al., 2009; Jorstad et al., 2010; Vercellone et al., 2011).

In this chapter, the γ-ray flares peaking in June 2014 from 3C 454.3 are studied in detail, in order to understand more deeply the characteristics and location of the γ-ray emission. This flare period can be seen in Fig. 3.4, with the flux peaking on MJD 56823. A leptonic origin from a spherical emission region is assumed, where high energy electrons in the

relativistic jet up-scatter low energy photons external to the jet, through IC scattering (Ghisellini et al., 2010a). In Section 4.1, the method for data preparation and *Fermi*-LAT data analysis routines are described. In Section 4.2 the findings in relation to the γ-ray flux variability timescales are presented, and in Section 4.3 the spectral shape during the flare period is explored. This includes both the variation in the shape of the spectrum and an analysis of the high energy emission. An investigation into whether or not an energy-dependence on the cooling of the emitting electron population exists is carried out in Section 4.4, and the interpretation of the combined results is discussed in Section 4.6. The conclusions are summarised in Chapter 6.

4.1 Data Preparation and Source Modelling

Enhanced γ-ray emission from 3C 454.3 was reported by Buson (2014) as the first of two γ-ray flares was peaking on 15th June 2014. For this reason, the flaring period is referred to as June 2014 in this thesis. The data used in this study were collected by the *Fermi*-LAT. Photons detected in the energy range $0.1 \leq E_\gamma \leq 300\,\text{GeV}$ are considered, between mission elapse time (MET) 422409603 and 427248003. This corresponds to midnight on the 22nd May 2014 until midnight on 17th July 2014. The region of interest (RoI) covers a radius of $15°$ centred on 3C 454.3. A radius of $15°$ was chosen to account for the PSF of the detected γ-rays.

'Source' class photons were selected for analysis, and the instrument response function used was P7REP_SOURCE_V15. As recommended by the P7REP data selection criteria, a zenith cut of $100°$ was applied in order to exclude background photons from the Earth's atmosphere. The good time intervals were created by specifying that the LAT detector was at a rock angle of $< 52°$ and the filter expression '(DATA_QUAL==1) && (LAT_CONFIG==1)' was satisfied. The analysis criteria are summarised in Table 4.1.

In order to calculate the correct flux for each γ-ray source from the raw *Fermi* data, a model was created containing the position and spectral definition of all of the point sources and diffuse emission in the RoI. The Galactic and extragalactic diffuse models used were gll_iem_v05_rev1.fit and iso_source_v05.txt respectively. Both 3C 454.3 and neighbouring sources were modelled using the spectral definitions given in the *Fermi*-LAT 2-year Point Source Catalog 2FGL[1]. The spectra of point sources in the region of interest

---

[1]The *Fermi*-LAT 4-year Point Source Catalog, 3FGL, was released during the writing of this thesis. The

Science Tools version	v9r33p0
IRF	P7REP_SOURCE_V15
Event class	SOURCE, Reprocessed Pass 7
Photon energies	0.1 - 300 GeV
Radius of interest	15°
Zenith angle cut	≤ 100°
Rocking angle cut	< 52°
LAT config./Data quality	==1
Galactic diffuse model	gll_iem_v05_rev1.fit
Isotropic diffuse model	iso_source_v05.txt
γ-ray source catalog	gll_psc_v08.fit
Apply RoI zenith-angle cut	In gtmktime

Table 4.1: Table summarising the *Fermi*-LAT analysis criteria used to study the June 2014 flare of 3C 454.3.

are often modelled as power laws. The log parabola spectral shape of 3C 454.3, as well as of other blazars modelled in the RoI, is defined as (Nolan et al., 2012):

$$dN/dE = N_0(E/E_b)^{-(\alpha+\beta(log(E/E_b)))} \tag{4.1.1}$$

where dN/dE is the number of photons cm^{-2} s^{-1} MeV^{-1}, N_0 is the normalisation of the energy spectrum, E is the γ-ray photon energy, and E_b is the scaling factor of the energy spectrum. α and β (curvature) are spectral parameters.

A binned analysis was run initially to find the spectral parameters that best describe each source during the period of interest. The MINUIT minimiser was used during all *Fermi* gtlike optimisations. During this binned analysis, the spectral parameters of all of the sources in the RoI were free to vary. This ensured that the spectral parameters returned for each source provided an accurate representation of the spectral state of the source during the time period studied here.

From the results of the binned analysis, the observed γ-ray counts map was compared with the model counts map of the RoI, created by the *Fermi* gtmodel tool. This was done in order to assess whether or not any significant γ-ray sources existed in the RoI that had not been included in the 2FGL catalog. A residuals map was created by subtracting the model counts map from the observational counts map, and dividing by the model counts map. The observed map, model map and residuals map are shown in Fig. 4.1. If any significant sources were found that were not present in the model, they could be added accordingly (e.g. Brown, Adams & Chadwick 2015). Creating these maps ensured that all

---

3FGL contains a greater number of γ-ray sources than the 2FGL (Acero et al., 2015). However, the modelling and analysis routines performed in this chapter ensure that accurate results are drawn from the photon data.
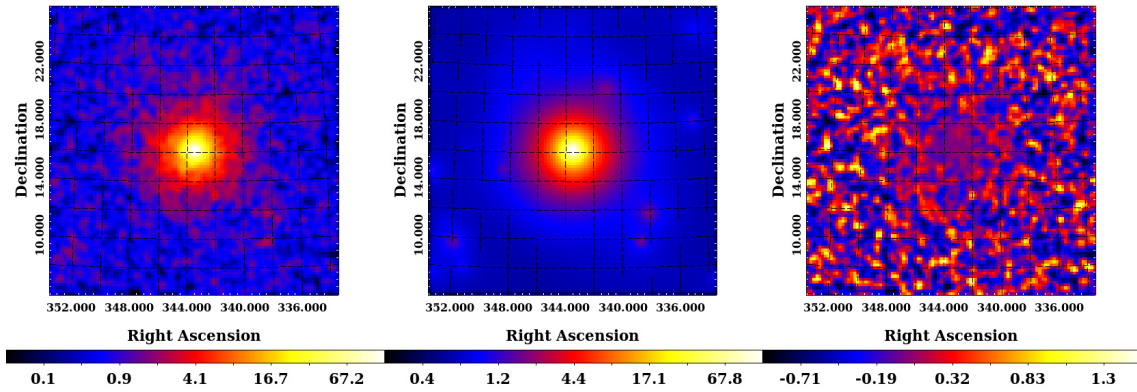
Figure 4.1: $20° \times 20°$ observed (left), model (centre) and residuals (right) maps of the 0.1-300 GeV flux centred on 3C 454.3. The observed and model maps are in units of γ-ray counts, and the residuals map is in units of percentage. All maps are smoothed with a 2° Gaussian, to reflect the PSF of photons at this energy range. All maps are at a scale of 0.2°/pixel.

of the sources in the RoI were accounted for and that both the γ-ray sources and RoI were represented accurately across the time period under investigation. No significant sources were detected that had not already been included in the 2FGL catalog, so no additional sources were added to the model.

In order to study the γ-ray characteristics of 3C 454.3, the correct initial model of the RoI was used during the unbinned analyses. These analyses were then employed to create plots of flux and spectral parameters with time, presented in Sections 4.2 - 4.5. For the unbinned analyses, spectral parameters α, β and N_0 of 3C 454.3 were input as the best-fitting parameters calculated from the binned analysis, but were free to vary during the gtlike fitting procedure. The spectra of all other sources except for the Galactic and extragalactic diffuse backgrounds were frozen at the best-fitting parameters returned by the binned analysis.

4.2 Flux Variability Timescales

Blazars are observed to be the most highly variable class of AGN. Strong γ-ray flux variability has been captured by the *Fermi*-LAT as well as by ground-based instruments, when blazars exhibit an outburst well above their baseline emission. The term baseline is used to mean emission at a typical flux level for a given blazar. For 3C 454.3, this is $F \sim 4.6 \times 10^{-6}$ ph cm^{-2} s^{-1} during the period of interest, from the average of the daily fluxes shown in Fig. 4.4. The rapid variability during these flares allows the physical processes occurring within the relativistic blazar jets to be probed more closely.

The timescales on which γ-ray emission from an AGN is observed to vary allow the size of the emission region to be constrained. It is assumed that the γ-rays originate from within the relativistic jet, with the two main emission locations under consideration being the BLR and the narrow-line or MT region. The BLR is located close to the base of the jet and the SMBH, while the torus is further downstream (Urry & Padovani, 1995). The jet expands and widens with distance from the SMBH according to its opening angle (thought to be of the order of ~0.1 rad, (Ghisellini & Tavecchio, 2009; Ghisellini et al., 2010a)), so that the cross-sectional diameter of the jet is smaller in the BLR than the MT. If the assumption is made that the entire cross-section of the jet at a certain location is responsible for the emission, the light-crossing time and therefore the γ-ray flux doubling timescale will be smaller for a BLR origin.

Ground-based telescopes such as the High Energy Stereoscopic System (H.E.S.S.) and Major Atmospheric Gamma Imaging Cherenkov (MAGIC) have measured γ-ray variability from blazars on extremely short timescales. Examples of these observed flux doubling times include ~220 s (Aharonian et al., 2007), ~2 min (Albert et al., 2007), and more recently < 5 min (Aleksić et al., 2014). Previous studies using *Fermi*, such as those of Brown (2013) and Saito et al. (2013), have investigated flux doubling timescales using a minimum of 3 hour time bins in the unbinned *Fermi* analysis. This duration is often chosen as the minimum because it is the time that the *Fermi*-LAT takes to complete one full scan of the sky (2 orbits). In the case of the FSRQ PKS 1510-089, this revealed intrinsic doubling timescales, τ_{int}, of τ_{int} = 1.30 ± 0.12 h during the October 2011 flare period seen in Fig. 3.1 (Brown, 2013). Paliya, Sahayanathan & Stalin (2015) also found variability of just τ = 1.19 h at the ~4σ significance level for the FSRQ 3C 279 during a flare in March 2014. Another recent study of this flare by Hayashida et al. (2015) found characteristic flux rising timescales of only τ = 1.4 ± 0.8 h, and flux decay timescales of τ = 0.68 ± 0.59 h, although the fitting errors are relatively large. However, the smallest timescales can be probed using good time interval (gti) time bins as described by Foschini et al. (2011a,b). The gti time bins are uneven in length and are provided with the *Fermi* raw photon data, with the binning being dependent on the instrument pointing direction (Foschini et al., 2013). The good time intervals are of the order of one orbit of *Fermi*, ~90 minutes. This analysis technique enabled Foschini et al. (2013) to discover the fastest FSRQ γ-ray variation measured to date, also during the October 2011 flare period of PKS 1510-089. The γ-ray flux took just ~20 minutes to double at the source (Foschini et al.,

2013). Doubling times of less than one hour enable us to put tight constraints on the size of the emission region.

The flux doubling timescales of the γ-ray data are calculated using:

$$F(t) = F(t_0)2^{(\tau^{-1}(t-t_0))} \tag{4.2.2}$$

where $F(t)$ and $F(t_0)$ are the flux at times t and t_0 respectively and τ is the observed flux doubling timescale. This observed timescale can be used to calculate the intrinsic doubling timescale by taking into account the redshift of 3C 454.3, z = 0.859 (Jackson & Browne, 1991):

$$\tau_{int} = \frac{\tau}{(1+z)} \tag{4.2.3}$$

A least-squares routine was used to calculate the parameters that provide a best-fit solution to equation 4.2.3 for flare rise and fall subsets of the data. Examples of the resulting curves are shown as the insets in Fig. 4.2. This fitting was done for both 3 hour and gti binned data. Fig. 4.3 shows the resulting fitting for all of the timescales at $\geq 5\sigma$ presented in Tables 4.2 and 4.3. Tables 4.2 and 4.3 give the intrinsic doubling timescales of the γ-ray flux for several time intervals between MJD 56799 and 56855. The errors given on the timescales in Tables 4.2 and 4.3 are one standard deviation, σ. Only data points with a gtlike analysis test statistic[2] $TS \geq 10$ ($\sim 3\sigma$) are considered. Doubling timescales that are ≤ 1.5 h with a significance of $\geq 3\sigma$ are shown. The significance of a doubling timescale in terms of σ is defined as how many standard deviations τ_{int} is from zero. Interestingly, no flux halving timescales that fit these criteria were found. From Table 4.2, four occasions on which the flux doubles in less than one hour at a significance level > 5σ are identified. The fastest doubling timescale discovered is $\tau_{int} = 0.68 \pm 0.01$ h, between MJD 56819.461 and 56819.593.

---

[2]The test statistic is defined as $TS = -2ln(L_0/L_1)$, where L_0 is the maximum likelihood value for a model when the source is not included, and L_1 is the maximum likelihood value for a model with the source included at the specified location (Mattox et al., 1996).
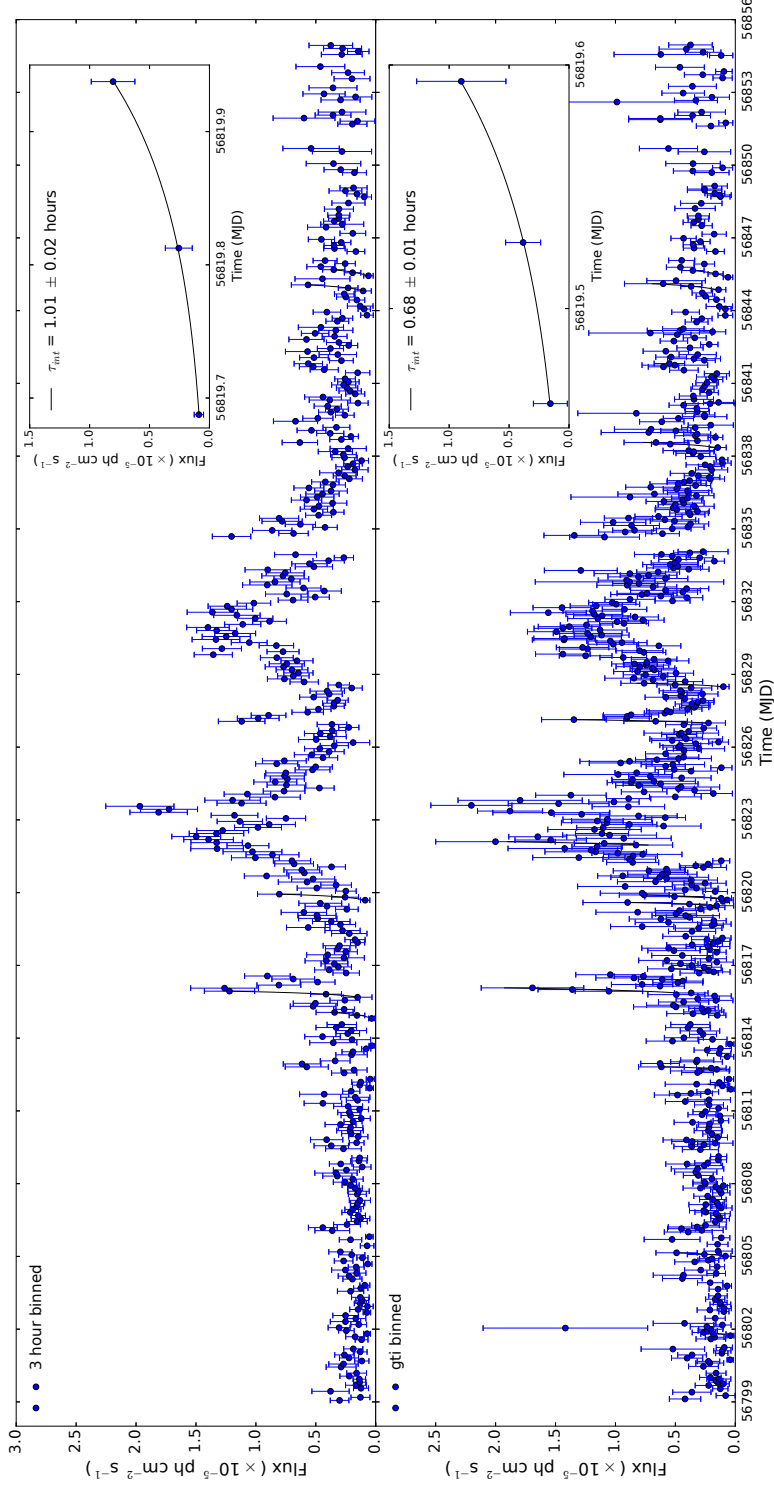
Figure 4.2: The light curve of 3C 454.3 between MJD 56799 and 56855. Top: 3 hour binned. Bottom: gti binned. The horizontal error bars are not shown here, but are of unequal sizes for the gti binning. The best-fitting curves of equation 4.2.3 are also plotted (black lines). The insets show zoomed-in sections of the light curves, and the corresponding shortest intrinsic doubling timescales are given in the legends. Only data points with $TS \geq 10$ are shown.
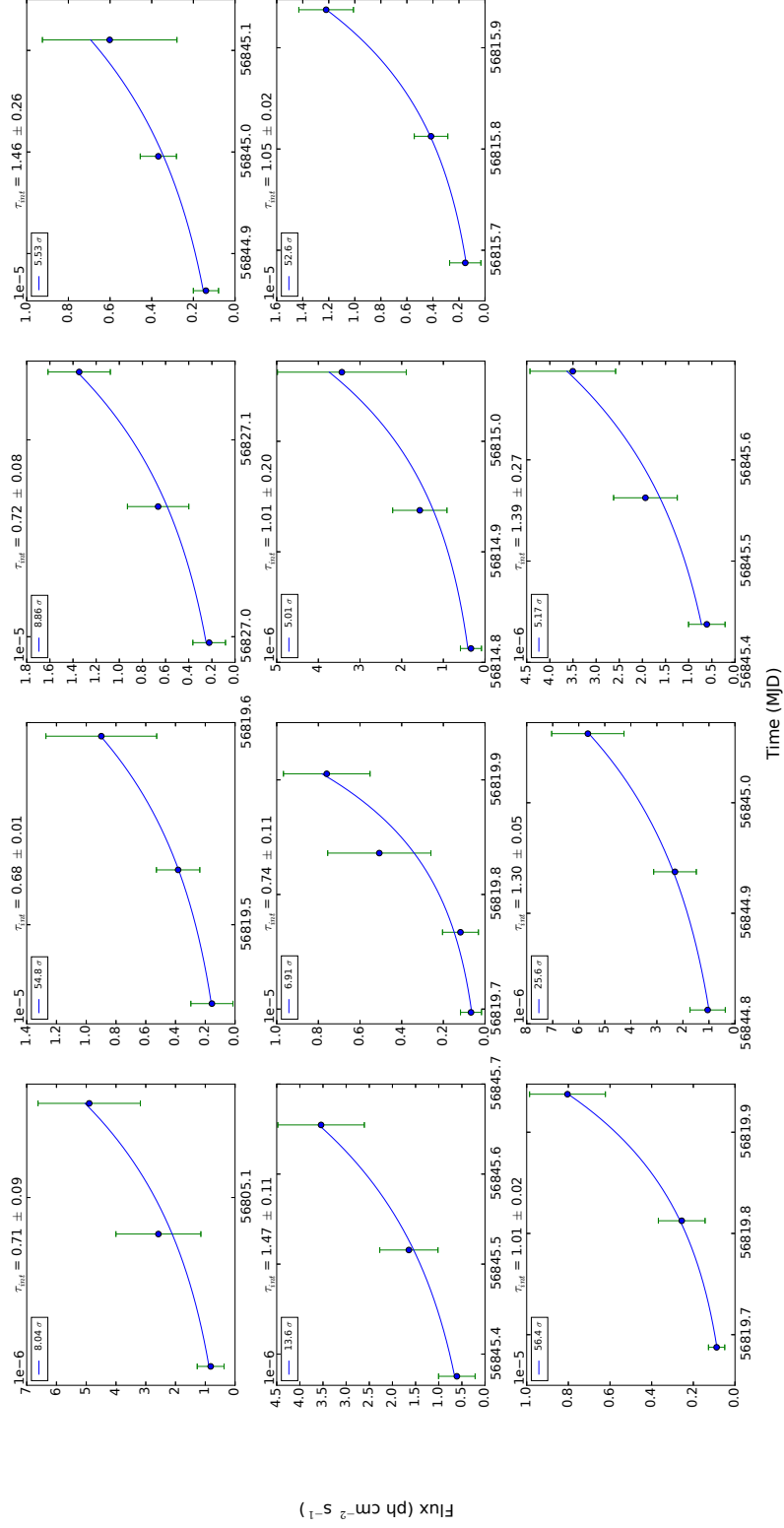
Figure 4.3: The intrinsic flux doubling timescale curve fitting, for all of the $\geq 5\sigma$ significance timescales. The intrinsic flux doubling timescales in hours are given above each subplot, and the significances are given in the legend.

Start Time (MJD)	End Time (MJD)	$F(t_0)$ ($\times 10^{-6}$ ph cm^{-2} s^{-1})	$F(t)$ ($\times 10^{-6}$ ph cm^{-2} s^{-1})	τ_{int} (hours)	Significance (σ)
56805.011	56805.150	0.82 ± 0.45	4.9 ± 1.7	0.71 ± 0.09	8.04
56819.461	56819.593	1.6 ± 1.4	9.0 ± 3.7	0.68 ± 0.01	54.8
56826.997	56827.134	2.2 ± 1.4	13 ± 3	0.72 ± 0.08	8.86
56844.863	56845.110	1.4 ± 0.6	6.0 ± 3.2	1.46 ± 0.26	5.53
56845.375	56845.655	0.61 ± 0.39	3.5 ± 0.9	1.47 ± 0.11	13.6
56819.697	56819.905	0.67 ± 0.50	7.6 ± 2.1	0.74 ± 0.11	6.91
56801.732	56801.864	0.40 ± 0.29	2.6 ± 1.0	0.67 ± 0.19	3.54
56811.893	56812.101	0.39 ± 0.28	3.2 ± 2.6	0.99 ± 0.29	3.43
56812.713	56812.814	1.5 ± 1.1	6.2 ± 1.9	0.54 ± 0.15	3.52
56816.731	56816.857	1.8 ± 1.4	5.3 ± 2.0	0.88 ± 0.22	3.92
56819.697	56819.836	0.67 ± 0.50	5.1 ± 2.5	0.56 ± 0.15	3.74
56821.962	56822.102	8.3 ± 3.1	20 ± 5	1.30 ± 0.32	4.02
56828.494	56828.634	1.0 ± 0.5	7.6 ± 1.9	0.66 ± 0.20	3.22
56838.355	56838.564	1.5 ± 0.7	6.6 ± 2.7	1.22 ± 0.32	3.82
56815.865	56816.074	3.7 ± 1.4	17 ± 4	1.34 ± 0.37	3.66

Table 4.2: γ-ray flux intrinsic doubling timescales and their significance, from the gti unbinned analysis. Above the horizontal line, the timescales are significant at the $\geq 5\sigma$ level.

The size of the emission region can be constrained using:

$$R \leq c\delta\tau_{int} \tag{4.2.4}$$

where R is the diameter of the emission region, c is the speed of light and δ is the Doppler factor of the jet. These sub-hour flux doubling timescales therefore imply that the size of the emission region is relatively small. Taking equation 4.2.4 and $\tau_{int} = 0.68$ h, the size of the emission region can be constrained to be $R\delta^{-1} \leq 2.38 \times 10^{-5}$ pc.

The intrinsic doubling timescales in Table 4.2 can be used to calculate the required Doppler factor of the jet, if a minimum size for the emission region is assumed. The mass of the SMBH, M_{BH}, of 3C 454.3 is $(0.5 - 4.6) \times 10^9 M_\odot$ (Gu, Cao & Jiang, 2001; Bonnoli et al., 2011). The corresponding range for the Schwarzschild radius of the SMBH, R_S, is $(0.48 - 4.40) \times 10^{-4}$ pc. This can be taken as the smallest cross-sectional radius of the jet, provided that the jet doesn't re-collimate downstream. One might assume that the

Start Time (MJD)	End Time (MJD)	$F(t_0)$ ($\times 10^{-6}$ ph cm^{-2} s^{-1})	$F(t)$ ($\times 10^{-6}$ ph cm^{-2} s^{-1})	τ_{int} (hours)	Significance (σ)
56814.813	56815.063	0.34 ± 0.25	3.4 ± 1.5	1.01 ± 0.20	5.01
56815.688	56815.938	1.5 ± 1.2	12 ± 2	1.05 ± 0.02	52.6
56819.688	56819.938	0.88 ± 0.39	8 ± 2	1.01 ± 0.02	56.4
56844.813	56845.063	1.1 ± 0.7	5.7 ± 1.4	1.30 ± 0.05	25.6
56845.438	56845.688	0.61 ± 0.39	3.5 ± 0.9	1.39 ± 0.27	5.17

Table 4.3: γ-ray flux intrinsic doubling timescales and their significance, from the 3 hour unbinned analysis.

Schwarzschild radius is therefore the minimum radius of the γ-ray emission region. This is a conservative assumption, as the emission region could also take the form of a small blob within the jet. Taking the Schwarzschild radius as the minimum emission region radius, the range of minimum Doppler factor required for a flux doubling timescale $\tau_{int} = 0.68$ h is therefore $\delta_{min} = 4.03 - 37.03$, from equation 4.2.4. However, it should be noted that a value of δ as low as $\delta = 4.03$ is not consistent with previous measurements of δ for 3C 454.3 (Jorstad et al., 2005; Ackermann et al., 2010; Abdo et al., 2011). Jorstad et al. (2005) used very long baseline interferometry (VLBI) observations of 3C 454.3 to derive jet Doppler factors of ~14-30. If the mass of 3C 454.3 is at the lower end of the proposed range, as suggested by Bonnoli et al. (2011), a value of $\delta = 4.03$ might therefore be interpreted as evidence that the emission region is not covering the full cross-section of the jet. We will discuss relevant emission region models for the June 2014 flares in Section 4.6.

The size of the emission region compared with the size of the jet may be dependent on factors such as the Doppler factor of the jet and the geometry of the jet, as described above. If a value of $\delta = 25$ is used for the sake of argument, which is consistent with the literature (Jorstad et al., 2005) and with the above calculations, the size of the emission region is limited to $R \leq 5.95 \times 10^{-4}$ pc for $\tau_{int} = 0.68$ h.

It should be highlighted that constraining the size of the emission region does not locate the emission region. However, once the location of the emission region is inferred, it will be interesting to compare the size of the emission region with the size of the jet at that location.

4.3   Spectral Shape and Photon-Photon Pair Production

High energy photons, such as γ-rays at $E_\gamma > 10$ GeV, can be absorbed by lower energy optical and UV photons. This leads to photon-photon pair production as described in Section 2.2 ($\gamma\gamma \rightarrow e^+e^-$). FSRQs such as 3C 454.3 are very bright in their innermost regions, near to the SMBH and the accretion disk. Several studies have shown that γ-rays emitted here can be absorbed by the lower energy ambient photons in these inner regions (Donea & Protheroe, 2003; Liu & Bai, 2006). In this way, high energy γ-rays originating close to the base of the jet are absorbed before they are able to escape the BLR. The photon field external to the jet is comprised of photons from the accretion disk, the reprocessed

emission in the BLR or MT, and thermal radiation from the corona close to the SMBH (Blazejowski et al., 2000; Sikora et al., 2002; Ghisellini & Tavecchio, 2009). The density of this photon field at a given point along the jet is dependent on the distance to the SMBH and the accretion disk luminosity (Ghisellini & Tavecchio, 2009; Sikora et al., 2009; Pacciani et al., 2014). The photon density in the MT is therefore much lower than inside the BLR, greatly increasing the likelihood of pair production in the BLR compared to the MT. This photon attenuation manifests itself as a high energy cut-off in the γ-ray spectrum, such that the shape of the spectrum may be better described by a log parabola than a power law. As the MT is not as opaque to high energy photons as the BLR, one would not expect to observe a cut-off due to attenuation if the γ-rays are being produced here. It has been suggested that the spectral shape of 3C 454.3 can be fitted well by a log parabola or a broken power law, where γ-rays are being emitted from the base of the jet (e.g. Ackermann et al. 2010; Poutanen & Stern 2010; Harris, Daniel & Chadwick 2012). It has also been suggested that specific GeV breaks that are present in the spectra of some AGN could be arising due to pair production of γ-rays with the He Lyman recombination continuum, again in the BLR (Poutanen & Stern, 2010). However, Harris, Daniel & Chadwick (2012) found that the location of these spectral breaks was inconsistent with the absorption model proposed. A log parabola spectral shape might also arise from a curved energy distribution of the emitting electrons (Dermer et al., 2015).

4.3.1 Spectral Variation

As discussed in Section 4.1, the spectral shape of 3C 454.3 is modelled by a log parabola, equation 4.1.1. The log parabola is the spectral shape used to describe 3C 454.3 in the first two *Fermi*-LAT catalogues (1FGL, 2FGL). The parameter α dictates the slope of the spectrum and is therefore a measure of the hardness of a spectrum, with a shallower slope indicating relatively more high energy emission. The amount of curvature in the spectrum is described by β. This curvature leads to a cut-off in the flux at higher energies, with a larger curvature giving a sharper cutoff.

The presence of spectral variation with time is considered first. Changes in the α and β parameters of a log parabola indicate that the spectral shape of the γ-rays is changing. One possible reason for this is that the dominant location of γ-ray emission is changing, particularly during a flare. A change in the spectral shape during a flare gives information on both the point-of-origin of the flare, and whether the emission location is different to
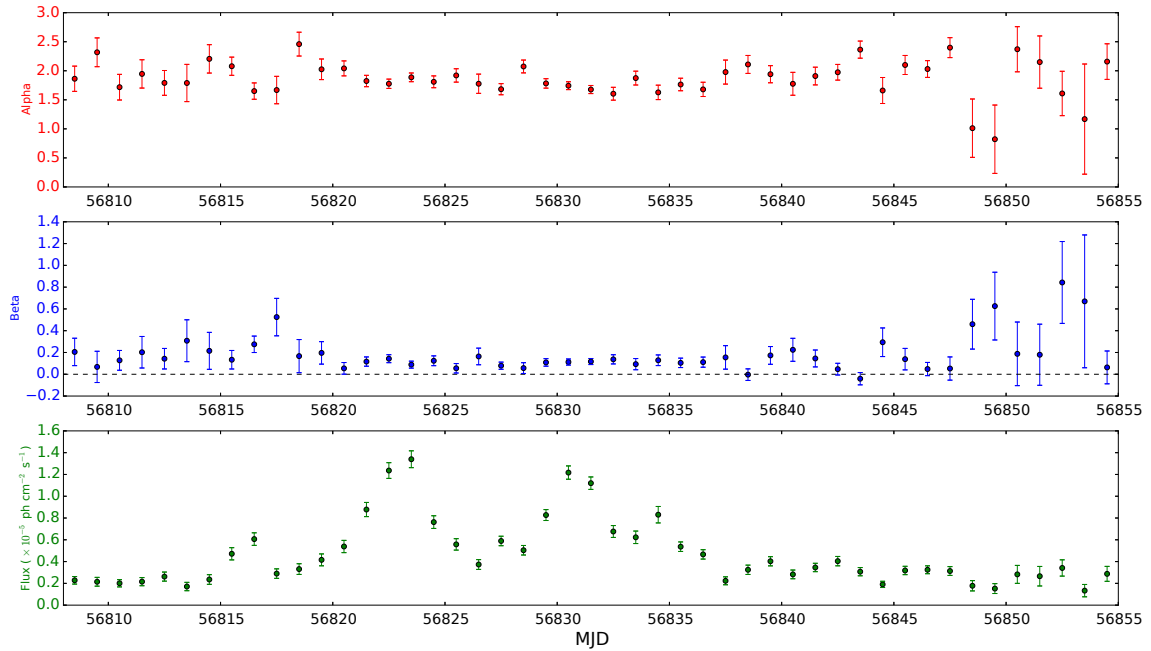
Figure 4.4: Top: α as a function of time. Middle: the variation of β with time. The dashed line is at β=0. Bottom: the γ-ray light curve. All three plots are binned daily. No strong trend of α and β with flux is identified. The curvature during the flares is lower and less turbulent than during the baseline emission. All of the data points have a $TS \geq 25$.

that of the baseline γ-ray emission. Spectral changes with increasing flux are of interest as they could indicate injection into the high energy part of the spectrum at this time, or a decrease in high energy attenuation.

The data in Fig. 4.4 are binned daily in order to observe trends in the spectral parameters without sacrificing the statistics. All of the data have a $TS \geq 25$ from the gtlike analysis. It can be seen from Fig. 4.4 that both α and β vary with time across June 2014, indicating that the spectral shape of 3C 454.3 is changing across the flare period.

There doesn't appear to be strong evidence for the spectrum becoming harder as the FSRQ gets brighter, or for a correlation between curvature and flux. In order to investigate this further, it is also useful to look at α and β as a function of flux. Figs 4.5 and 4.6 are binned daily, and show that the relationship between both α and β with flux becomes flatter at higher flux. The lowest values of α can be seen at low flux in Fig. 4.5, although there are large error bars on these points. The highest curvature is also seen at low flux in Fig. 4.6, again with large error bars. These data correspond to MJD 56848 onwards, as can be seen from Fig. 4.4. This is ~10 days after the second flare has finished, and the flux is ~5 times lower than during the peak of the flares. The large errors on α and β at this
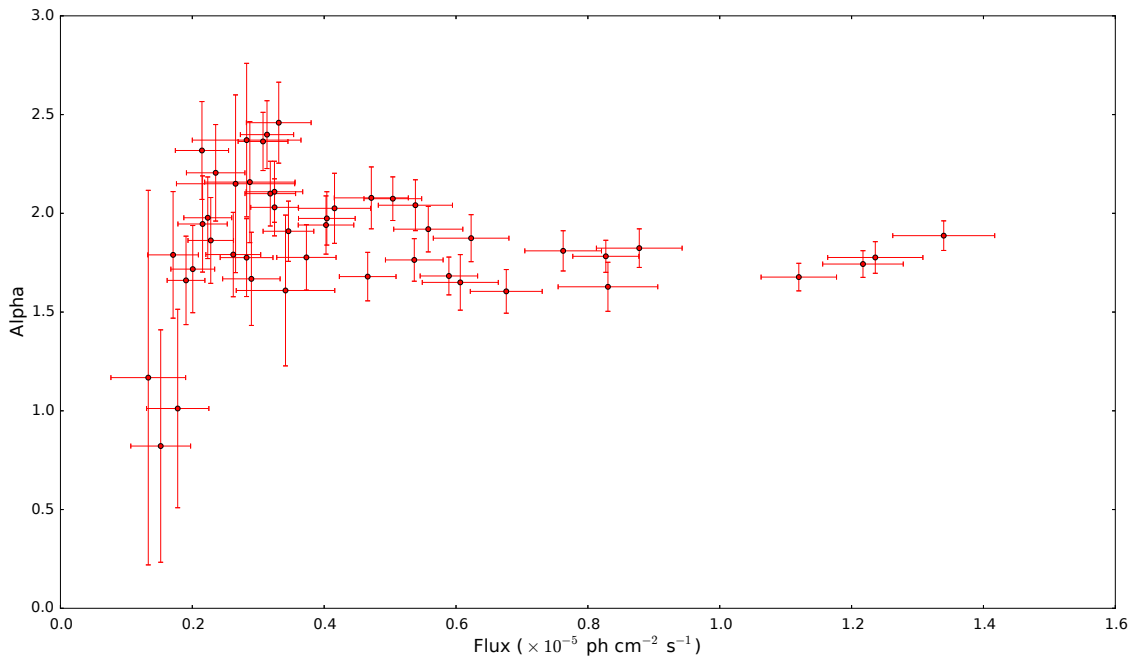
Figure 4.5: α as a function of flux, binned daily. All of the data points have a $TS \geq 25$.
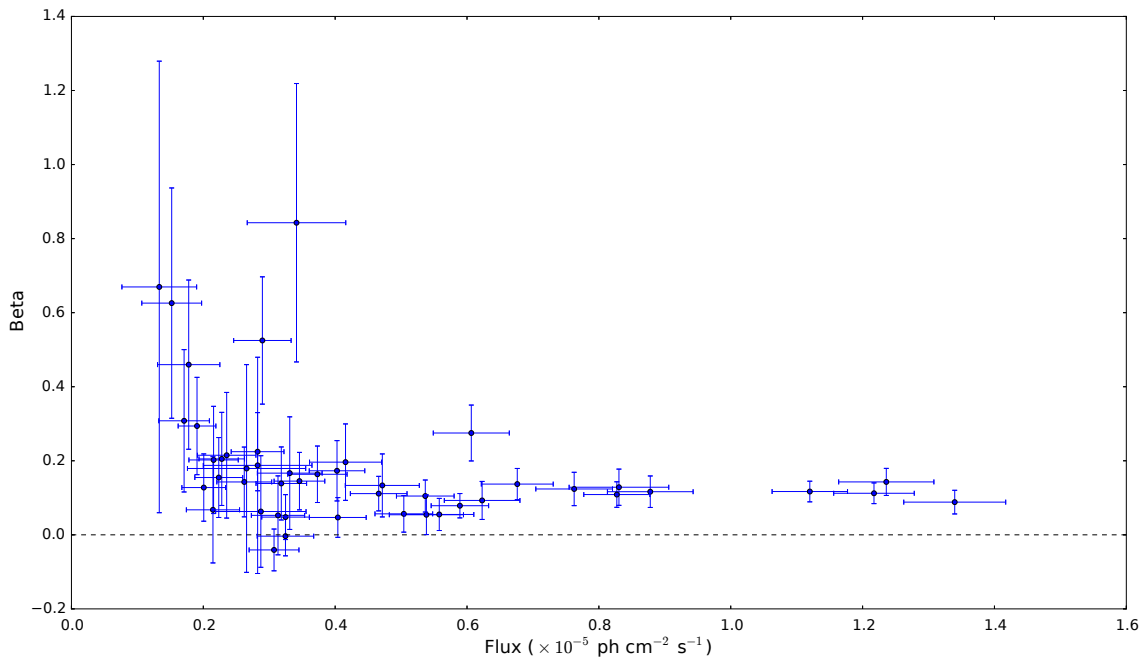
Figure 4.6: β as a function of flux, binned daily. The dashed line is at $\beta = 0$. All of the data points have a $TS \geq 25$.

time are likely to be due to poor photon statistics and there are also relatively large errors on the flux here, seen in Fig. 4.4.

Specifically how α changes during the flare period is now considered. Fig. 4.5 does not show a strong correlation between the hardness of the source and flux. When the flux reaches above $F = 0.6 \times 10^{-5}$ ph cm^{-2} s^{-1}, α remains between 1.5 and 2 and the distribution is relatively flat. A spectral index of < 2, or $\alpha < 2$ in the case of a log parabola, is generally considered to be a hard spectrum. At lower flux there is a greater range of α, but a slightly negative correlation can be found, suggesting a harder-when-brighter behaviour. This could either be due to the energy of the emitting electron population, or an indication that the high energy emission suffers less from absorption during the flares.

How β is changing is examined next. When $\beta = 0$, the spectral shape of a log parabola is equivalent to a power law, as there is no longer any spectral curvature. A low value of β therefore strongly suggests a power law spectral shape if the error on β is small. When β is larger, such as on MJD 56849 in Fig. 4.4, the spectral shape takes the form of a log parabola. However, if the error on β is also large it cannot be concluded that strong curvature is present. Despite the large errors on β either side of the flares in Fig. 4.4, a change in the spectral curvature during the flare period can be identified. The curvature appears to be lower during the flares than during the baseline emission. This is supported by the results of a least-squared analysis performed to find the best-fitting constant value of β. The analysis was done for the entire period between MJD 56808 and 56855, and also between MJD 56818 and 56038, across the flares. A higher value of β was returned across the entire period compared to during the flares. The reduced chi-squared values for the fits are $\chi^2_{red} = 2.86$ and $\chi^2_{red} = 0.65$ respectively, demonstrating that a lower value and flatter distribution of β are better fits to the data during the flares. Current evidence for an unambiguous variation of the spectral curvature between MJD 56808 and 56855 is therefore suggestive, although not yet compelling. Whilst other possible explanations exist, this could be interpreted as evidence that the flaring emission region is at a different location to that of the baseline emission. Better statistics would be required to probe the spectral shape either side of the flares and explore the idea of multiple emission regions further.

Fig. 4.6 shows no strong trend in curvature, due to the errors on β being large at low flux. It can however be seen that there is curvature on the majority of days between MJD 56808 and 56855. Approximately ten days during this period are consistent with $\beta = 0$, but
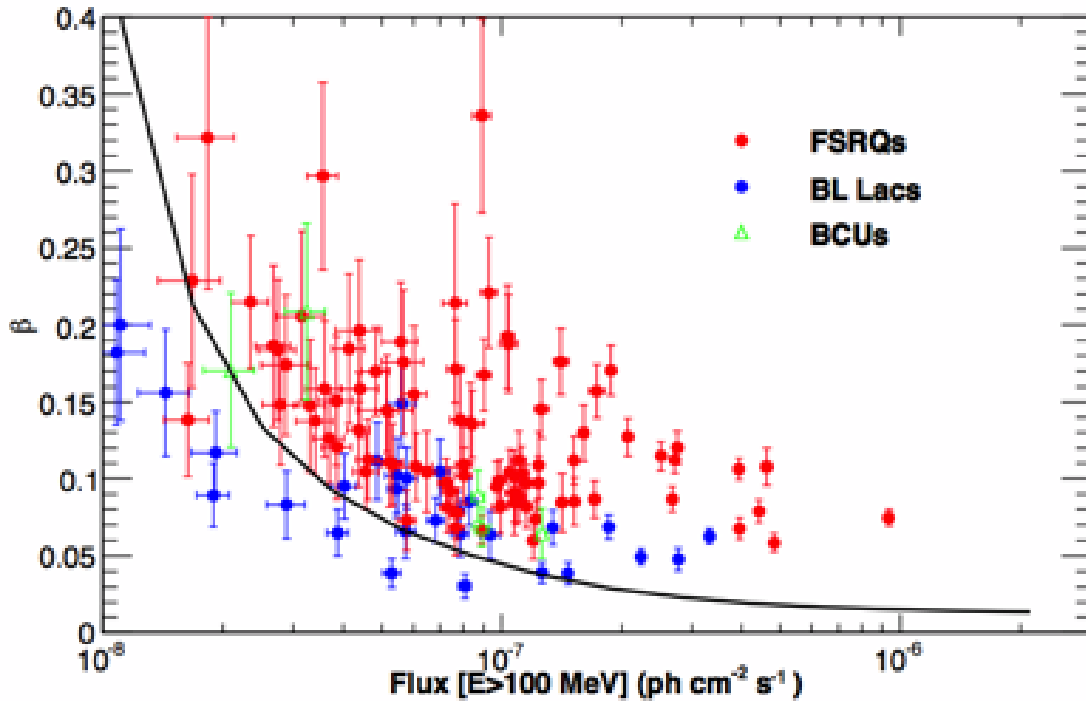
Figure 4.7: β against flux for four years of observations on FSRQs and BL Lac objects. The green triangles are AGN of unknown type. The black line shows the analysis limit of $TS = 16$ estimated for FSRQs. Taken from Ackermann et al. (2015).

there is certainly evidence for spectral curvature across the flux range. There is a trend towards larger curvature at lower flux, even with the larger error bars being taken into account. At higher flux, above $F = 0.6 \times 10^{-5}$ ph cm^{-2} s^{-1}, the distribution of β becomes much flatter and β is not consistent with 0. It should be noted that a process other than pair production in the BLR could be responsible for the small amount of curvature that is seen during the flares, and this will be discussed in Section 4.3.2.

Whether or not the trend of β decreasing with flux is solely due to poor photon statistics at the low flux end needs to be assessed. The trend of decreasing curvature that can be seen in Fig. 4.6 could be due to the fact that a curved spectrum is more easily fitted when there are large error bars on the flux, or it could represent a real change in the emission characteristics. To determine which interpretation is most likely, Fig. 4.6 can be compared to Fig. 4.7, taken from the third catalog of AGN detected by the *Fermi*-LAT (3LAC) (Ackermann et al., 2015). The 3LAC plot shows β against flux for four years of observations on FSRQs and BL Lac objects. Theirs is a phenomenological study with a large data set, but it shows the same shape and trend of β with flux as in the daily binned Fig. 4.6. The 3LAC data is also less limited by statistics than Fig. 4.6. Nonetheless, further

Emitted Energy (GeV)	Significance (σ)	Flux ($\times 10^{-6}$ ph cm^{-2} s^{-1})
≥ 35	9.8	2.57 ± 0.88
≥ 50	6.8	1.14 ± 0.57

Table 4.4: The flux and significance for $E_{\gamma, emitted} \geq 35$ GeV and $E_{\gamma, emitted} \geq 50$ GeV emission, between MJD 56808 and 56855. A single time bin was used over this period.

work is needed to make firm conclusions, but the similarity in trend might indicate that the property of a smaller curvature at larger flux is not simply due to poor statistics in the case of these flares.

4.3.2 VHE Emission

VHE emission is defined as observed emission from a source at $E_{\gamma} \geq 100$ GeV. At present, there are only 5 FSRQs that have been observed as VHE emitters[3], which does not include 3C 454.3. This is most likely due to the attenuation at high energy for the case of a BLR origin, which is classically assumed to be the location of the emission region. Observations by Abdo et al. (2009) showed that the majority of blazars that emit in the TeV energy range have a hard photon spectrum, with a photon index < 2. As 3C 454.3 displays a similarly hard spectrum throughout the flare period, an unbinned analysis was done to calculate the significance of $E_{\gamma} \geq 100$ GeV emission between MJD 56808 and 56855. No significant emission at $E_{\gamma} \geq 100$ GeV was found. 3C 454.3 is therefore not a VHE emitter during this period, despite the hardness of the γ-ray spectrum seen in Fig. 4.5. A lack of VHE emission could be due to a high energy cut-off, caused by the curvature of the spectrum that is seen in Fig. 4.6. This might suggest that either the emitting electrons are not energetic enough to produce VHE γ-rays, or that there is a mechanism for high energy γ-ray attenuation taking place during flaring episodes.

The significance of $E_{\gamma} \geq 20$ GeV high energy emission during the flares is probed next. The data are binned into 5 day periods between MJD 56810 and 56845, so that the statistics are good enough to detect the presence of high energy emission both during the flares and either side. The 5 day binned α values confirm that α remains below 2 across this period, and it can be seen that $E_{\gamma} \geq 20$ GeV emission is only significant during MJD 56825-30 and MJD 56830-35. The significance of the emission is > 5σ and > 8σ respectively. The 5 day binned values of α are consistent within error between MJD 56810-45, except

---

[3]http://tevcat.uchicago.edu/ (accessed on 15/05/15). See Wakely & Horan (2008).

spherical shell of BLR clouds
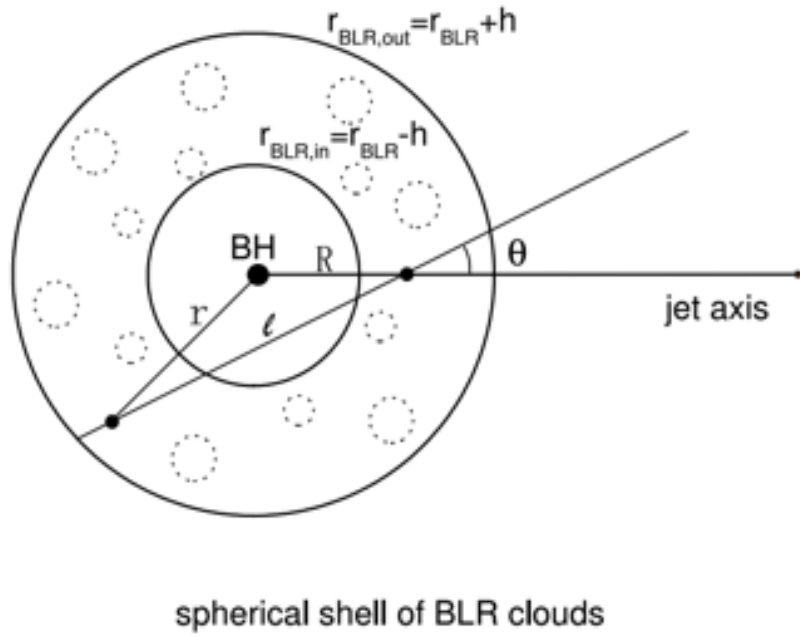
Figure 4.8: Schematic diagram of the structure of an FSRQ, including a spherical BLR shell surrounding a central SMBH. In the figure, $r_{BLR,in}$ corresponds to R_{BLR} in this thesis, and $r_{BLR,out}$ in the figure is equivalent to R_{BLR}^{out} in the thesis. The h in the figure is half of the BLR shell thickness. Figure taken from Liu & Bai (2006).

for over MJD 56830-35. Here, α reaches a minimum, at a value of $\alpha = 1.72 \pm 0.04$. This suggests a trend towards spectral hardening at the peak of the second flare.

In order to quantify the position of the emission region, the optical depth of different *emitted* photon energies with distance from the SMBH, both within the BLR and beyond, is studied. In order to do this, the BLR is modelled as a spherical shell surrounding the central SMBH, as shown in Fig. 4.8. The expansion of the Universe means that *Fermi* will detect γ-rays at $E_\gamma = E_{\gamma,emitted}/(1 + z)$, where $E_{\gamma,emitted}$ is the photon energy emitted at the source. The photon optical depth is a measure of how opaque a region is, in terms of how far a γ-ray can travel before being absorbed through γ-γ pair production in this case. The intensity of the external photon field at a certain point along the jet dictates the optical depth of γ-rays of energy ϵ, $\tau_{\gamma\gamma}(\epsilon)$. This is why the optical depth outside the BLR is much lower than inside (Liu & Bai, 2006).

Pacciani et al. (2014) interpolated the work of Liu & Bai (2006) in order to calculate optical depths for the BLR region of 3C 454.3. They found $\tau_{\gamma\gamma}(\epsilon) = 2.8$ at 35 GeV and $\tau_{\gamma\gamma}(\epsilon) = 4.0$ at 50 GeV, for γ-rays emitted at the mid-point of a spherical BLR shell. These are the *emitted* γ-ray energies at the source. In order to interpret these optical depths in the context of our *Fermi* data, the analyses need to be run on the *observed*

energies that correspond to *emitted* energies of 35 GeV and 50 GeV. The optical depths presented by Pacciani et al. (2014) give a clear indication that one would not expect to observe significant γ-ray emission of $E_{\gamma, emitted} \geq 35$ GeV and $E_{\gamma, emitted} \geq 50$ GeV if the γ-rays are being emitted at the mid-point of the BLR. Using the *Fermi* tools to calculate the flux between MJD 56808 and 56855 for *emitted* energies[4] $E_{\gamma, emitted} \geq 35$ GeV and $E_{\gamma, emitted} \geq 50$ GeV gives the fluxes shown in Table 4.4 at significances of 9.8σ and 6.8σ respectively. These high energy fluxes are both significant, meaning that the emission region during these flares is extremely unlikely to be located in the middle of the BLR, due to the high opacity at these energies. The optical depth of the γ-rays will decrease with distance towards the outer edge of the BLR and beyond, so it's much more likely that the emission region is towards this outer edge. However, the existence of an axion-like particle (ALP) that could facilitate the path of photons through the BLR should also be considered. This mechanism has been postulated in order to explain the detection of VHE emission from distant sources (Csáki et al., 2003; Harris & Chadwick, 2014).

Taking the distance to the outer edge of the BLR, R_{BLR}^{out}, to be ~3.8 times larger than the inner radius of the BLR, R_{BLR} (Ghisellini & Tavecchio, 2009; Pacciani et al., 2014), the optical depth relations given in Tavecchio et al. (2013) are used to assess at what distance along the jet the optical depth reaches a value of $\tau_{\gamma\gamma}(\epsilon) = 1$ for $E_{\gamma, emitted} = 35$ GeV and $E_{\gamma, emitted} = 50$ GeV photons. It is found that in both cases, the optical depth does not decrease to a value of 1 until the emission region is outside the BLR. In the case of $E_{\gamma, emitted} = 35$ GeV photons, $\tau_{\gamma\gamma}(\epsilon) = 1$ at ~4.0 × R_{BLR}, equivalent to ~1.1 × R_{BLR}^{out}. For $E_{\gamma, emitted} = 50$ GeV photons, $\tau_{\gamma\gamma}(\epsilon) = 1$ at ~4.8 × R_{BLR} or ~1.3 × R_{BLR}^{out}. These results suggest that the emission region of these high energy γ-rays is located outside the BLR.

In order to dissect the high energy emission further, the *Fermi* tool gtsrcprob was used to calculate the probability of each photon detected at $E_{\gamma, emitted} \geq 20$ GeV having been emitted by 3C 454.3. Only photons within a radius of 0.1° around 3C 454.3 were selected for analysis. Fig. 4.9 shows the individual *emitted* energies of the photons that were given a $\geq 99.7\%$ probability of originating from 3C 454.3, and the time at which they were detected. The largest number of these high energy photons are emitted between MJD 56824 and 56835, corresponding to the fall of the first flare until a few days after the peak of the second flare. There are 26 photons at $E_{\gamma, emitted} \geq 20$ GeV in total, and the highest

---

[4]This corresponds to *observed* energies, as detected by *Fermi*, of $E_\gamma \geq 35/(1+z)$ GeV and $E_\gamma \geq 50/(1+z)$ GeV respectively.
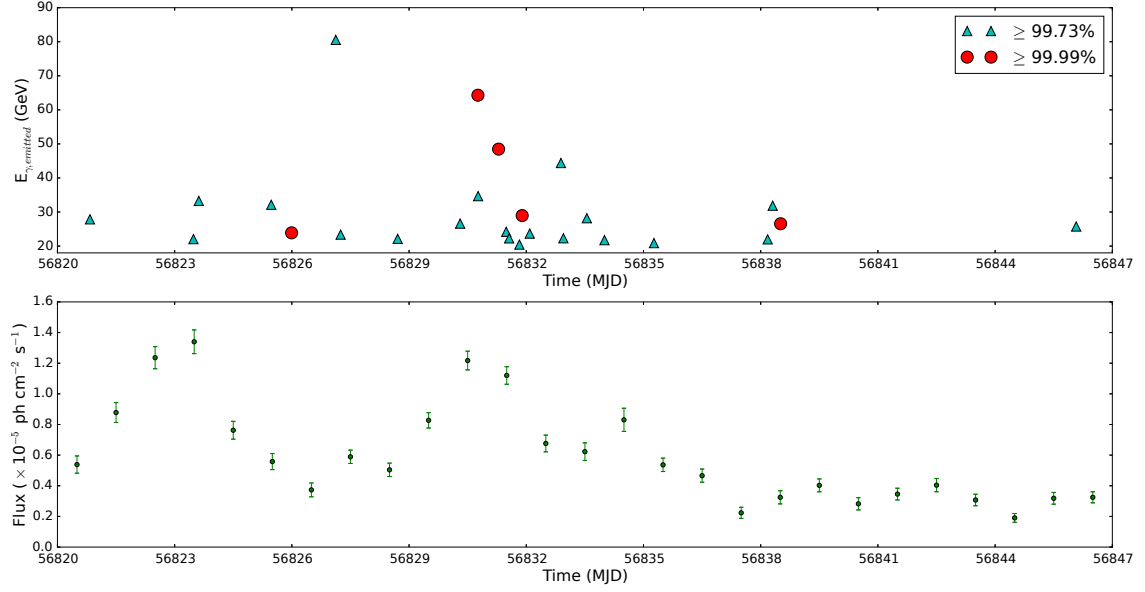
Figure 4.9: The emitted energies of the individual high energy photons detected by *Fermi* over the flare period, as a function of time. Only photons with $E_{\gamma,emitted} \geq 20$ GeV and a probability of originating from 3C 454.3 of $\geq 99.73\%$ are shown.

energy photon that is detected has an energy $E_{\gamma,emitted} = 80$ GeV. Interestingly, the highest energy photons are detected between MJD 56827 and 56833, coinciding closely with the second flare. This in-depth analysis of the high energy photons being emitted by 3C 454.3 supports the result that there is a spectral hardening between MJD 56830-35, and that significant high energy emission is emitted across the flare.

If the emission region is located at $r \sim 1.3 \times R_{BLR}^{out}$, a different model for the spectral curvature seen in Fig. 4.6 than pair production within the BLR is required. Pacciani et al. (2014) and Tavecchio & Ghisellini (2008) studied the effect of the Klein-Nishina suppression. The KN regime of IC scattering that occurs in the BLR results in an intrinsic curvature of the γ-ray spectrum at high energies. Fig. 4.10, taken from Pacciani et al. (2014), shows that this suppression alone causes a curvature in the spectrum until at least $\sim 8 \times R_{BLR}$. This is consistent with the distance constraint on the emission region derived from the June 2014 data, based on the presence of high energy emission.

4.4 Energy-dependent Cooling

Fig. 4.11 shows the γ-ray flux of 3C 454.3 in 6 hour time bins over the period of interest. The high energy, $1 \leq E_{\gamma} \leq 300$ GeV, and low energy, $0.1 \leq E_{\gamma} \leq 1$ GeV fluxes have been
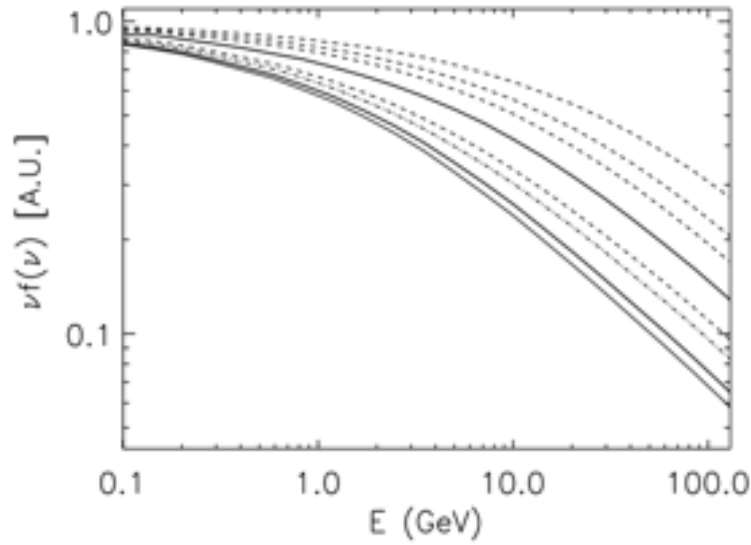
Figure 4.10: γ-ray SED for the IC scattering with seed photons from the BLR as a function of the location of the emission region. From the bottom up, the solid curves refer to an emission region located at the center of the BLR cavity, at R_{BLR}, R_{BLR}^{out}. The dot-dashed curve refers to an emission region at the mid-point of the BLR. From the bottom up, the four dashed curves refer to an emission region located at $3.8 \times R_{BLR}$, $5 \times R_{BLR}$, $6 \times R_{BLR}$, and $8 \times R_{BLR}$. Figure and caption taken from Pacciani et al. (2014).

plotted separately in order to highlight any energy-dependence that might exist in the rising and falling of the γ-ray flux. 6 hour bins were chosen to provide the balance between adequate statistics and being able to see the detail of the flare structure. The corresponding hardness ratio of 3C 454.3, the ratio of high energy flux to low energy flux F_{high}/F_{low}, is also shown, and only bins with $TS \geq 10$ are considered. No strong trend of hardness ratio with flux is identified, and the hardness ratio doesn't peak simultaneously with the flux. This may be evidence that the γ-ray flares are not solely due to an increase in flux at the high energy end of the spectrum.

As the energy-dependence of the flare cooling is an indicator of the energy-dependence of the emitting electron cooling, it is of interest to deduce whether or not any energy-dependence of the flare cooling exists, using Fig. 4.11. If the gradient of the hardness ratio is consistent with zero as the flares cool, the hardness ratio is remaining constant, meaning that the flux is not cooling differentially. This would indicate that the emission region is located within the BLR, with the IC scattering occurring in the KN regime (Dotson et al., 2012). Conversely, energy-dependent cooling would manifest itself as a negative correlation of hardness ratio with time, according to our definition of hardness ratio and fig. 3 of Dotson et al. (2012). The energy-dependence of the cooling in the
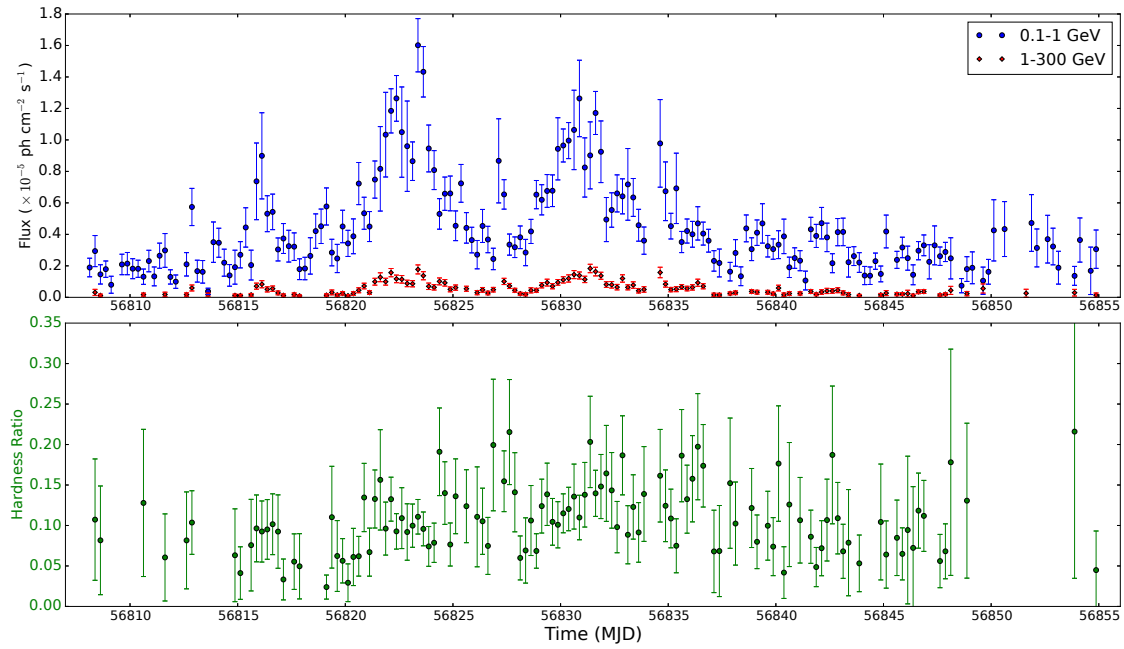
Figure 4.11: Top: The light curve of 3C 454.3, in 6 hour time bins. The low energy flux, $0.1 \leq E_\gamma \leq 1$ GeV is plotted using blue circles and the high energy flux, $1 \leq E_\gamma \leq 300$ GeV is plotted using red diamonds. Bottom: The corresponding hardness ratio of the γ-ray emission. This is the ratio of high energy flux to low energy flux. Only data points with $TS \geq 10$ are shown.
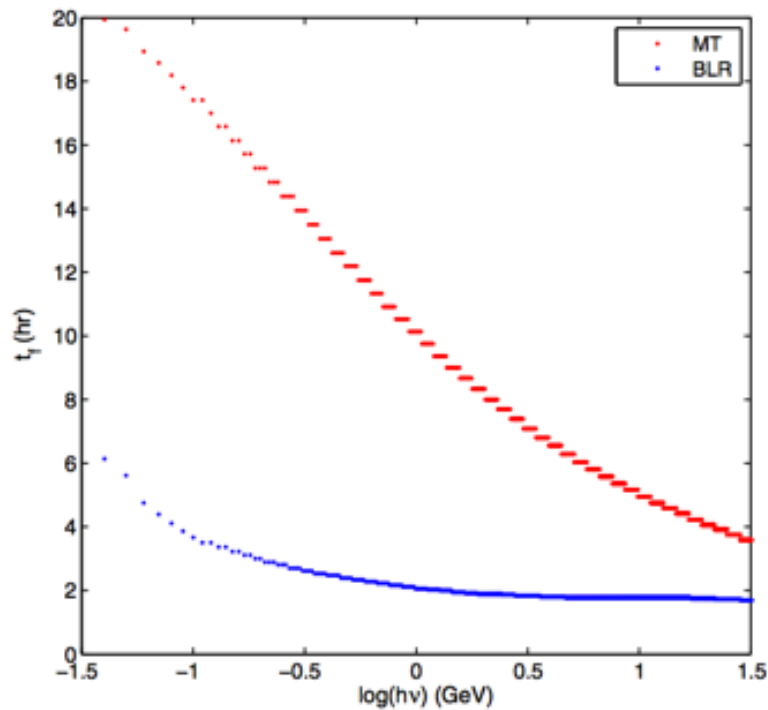
Figure 4.12: 1/e flux falling time in the galaxy frame against observed energy, for MT IC seed photons (red) and BLR seed photons (blue). Taken from Dotson et al. (2012).

MT is shown in Fig. 4.12. A least-squares analysis is performed between MJD 56823.2 and 56827.0 for the cooling of the first flare, and between MJD 56830.9 and 56834.5 for the second flare, to assess which of the two cases is applicable to the data. The results show that the gradient of the change in hardness ratio is $m = (2.56 \pm 8.04) \times 10^{-3}$ and $m = -(1.99 \pm 1.01) \times 10^{-2}$ for the first and second flare cooling respectively. The hardness ratio is therefore consistent with being constant for the first flare, due to the large statistical uncertainties on the hardness ratio. The cooling of the second flare shows evidence for a negative gradient of the hardness ratio with time, but at $< 2\sigma$ significance. It is also possible that substructures within the flares are masking any overall trend. Although it can be seen that there is variability in the hardness ratio between MJD 56808 and 56855, less statistical uncertainty would be required to come to a conclusion about the presence of energy-dependent cooling.

4.5 Spectral Energy Distribution

In order to compare the June 2014 flare with previous γ-ray flares of 3C 454.3, Fig. 4.13 shows the high energy SED of 3C 454.3 at several different epochs. Best-fit SED curves were calculated for each epoch in Fig. 4.13 using a third degree polynomial, taking a least-squares approach. Fig. 4.13 illustrates that although the June 2014 flare has a lower peak γ-ray flux than previous bright γ-ray flares, it is certainly significantly brighter than the quiescent state of 3C 454.3. However, the most notable feature in Fig. 4.13 is the relative position of the γ-ray peak frequency. It can be seen for the 2008, 2009 and 2010 SEDs that the peak frequency in the *Fermi*-LAT energy range corresponds to a photon energy $E_\gamma \sim 150$ MeV. For the June 2014 flare on the other hand, the peak is shifted to higher frequencies and lies between the $E_\gamma = 600$ MeV and $E_\gamma = 1200$ MeV energy bins. This is emphasised by the spectral curvature of the 2014 SED between $E_\gamma = 150$ MeV and $E_\gamma = 2400$ MeV, compared with the other observations. It can be seen that the γ-ray data for June 2014 illustrate a rise, peak and fall of the IC SED component. For the previous epochs, as the IC peak occurs at lower energies, the γ-ray data show only the fall of the IC component and may not contain the peak. This indicates that there is relatively more high energy emission in the June 2014 flare of 3C 454.3 than for previous flares, and for the quiescent state observed in 2008.
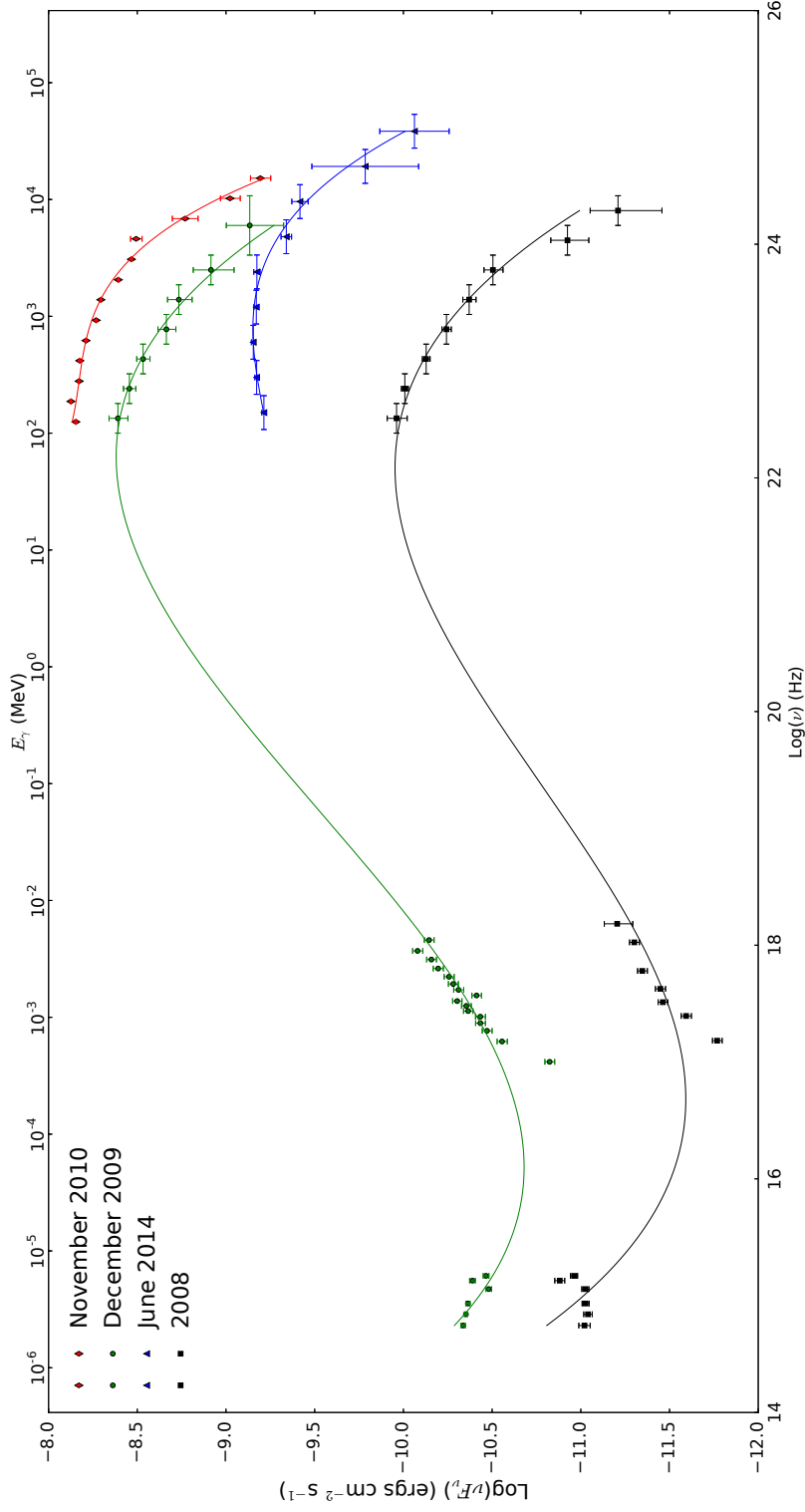
Figure 4.13: The high energy SED of 3C 454.3 during December 2008 - May 2009 (black), December 2009 (green), November 2010 (red) and June 2014 (yellow). The 2008 and 2009 data are from Bonnoli et al. (2011), and the 2010 data are from Abdo et al. (2011). The June 2014 spectrum uses the data analysed in this thesis. In all cases, the γ-ray data were observed by the *Fermi*-LAT. The optical-UV and x-ray data were observed by the *Swift* satellite, using the Ultraviolet-Optical Telescope and the X-Ray Telescope respectively. The x-axis is in units of $Log(\nu)$, where ν is the frequency of the photon. The frequency of a photon is related to the energy of a photon and Planck's constant, h, by $E_\gamma = h\nu$. The curves are the best-fit third degree polynomials that have been calculated using a least-squares approach.

It has been discussed by Sol et al. (2013) that γ-ray flares can be observed for a number of different reasons. These include an injection of particles into the jet, an increase in energy of the particles due to acceleration or by procession and beaming effects (e.g. Melrose 2009; Sironi & Spitkovsky 2009; Katarzynski & Walczewska 2010). It has been suggested that the movement of the SSC IC γ-ray peak of an SED with time can give insight into the mechanism that is causing the flare (Sol et al., 2013). As can be seen in Fig. 4.13, the energy range over which the spectrum of 3C 454.3 in June 2014 is constructed is limited, and to probe into the physical processes that are dominating the IC peak would require an extended SED before and after the flare. Even so, if the low γ-ray state is an accurate representation of the SED of 3C 454.3 during a quiescent state then the shift in peak frequency may be noteworthy. From Sol et al. (2013), the results of Fig. 4.13 suggest that an acceleration of the emitting particles may best describe the shift of the SED peak between the quiescent state and the June 2014 flare. However, as this modelling is based on a SSC model, the results may be more relevant to BL Lac objects than FSRQs, as discussed in Chapter 1. The results of modelling the shift in the SSC IC peak as a result of an acceleration can be seen in Fig. 4.14 (Sol et al., 2013).

4.6   Discussion

In order to draw conclusions on the location of the emission region, the emission characteristics from all of the analyses discussed in this chapter need to be combined.

The small amount of curvature and hard spectrum seen during the flares indicate an emission region that is not buried deep within the BLR. The optical depth calculations interpolated from Pacciani et al. (2014) can be used to constrain the location of the emission region, since significant emission of $E_{\gamma,emitted} \geq 35$ GeV and $E_{\gamma,emitted} \geq 50$ GeV is observed. Assuming that the γ-rays are not oscillating to ALPs, optical depth arguments place the emission region at least $r \sim 1.3 \times R_{BLR}^{out}$ from the SMBH. The effect of the KN suppression shown in Fig. 4.10 can account for the small amount of curvature that exists during the flares. Pacciani et al. (2014) used MWL SED modelling to locate the emission region during a high energy activity period of 3C 454.3, in September 2013. They found that the emission region was located at ~0.75 pc from the SMBH, which is significantly outside the BLR, upstream of the torus of 3C 454.3. They also found the γ-ray emission region to be located outside of the BLR for a number of other high energy FSRQs, and
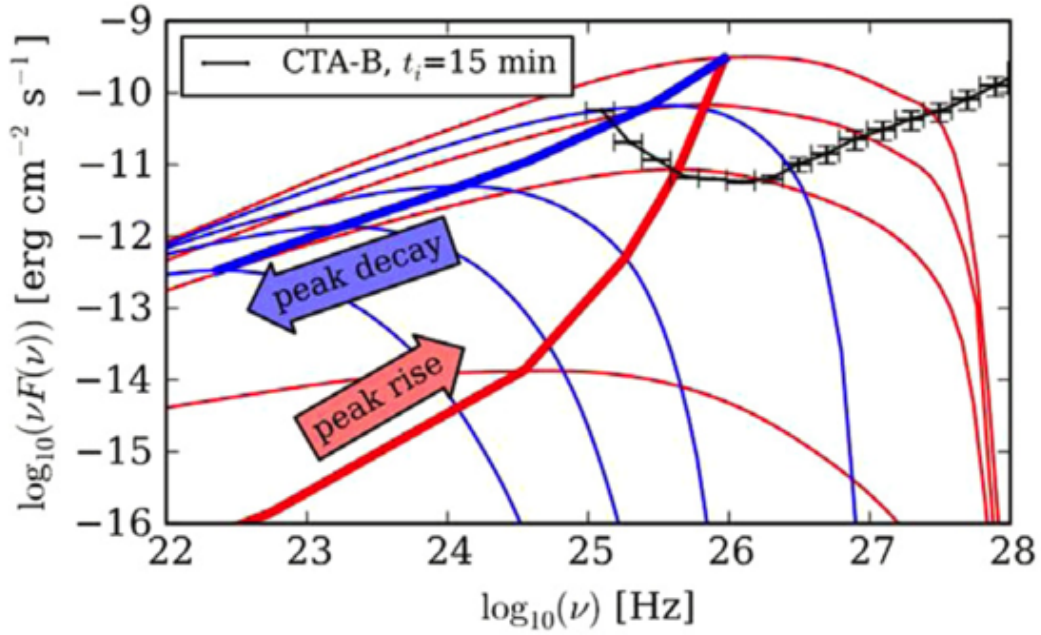
Figure 4.14: The effect on the SED with time as a result of the acceleration and cooling of γ-ray emitting particles, for a SSC model. Examples of the SED as emission rises (falls) are shown in red (blue) lines, with a thicker red (blue) line connecting the peaks of the SEDs. The bold black line shows the Cherenkov Telescope Array sensitivity curve for 15 minutes of integration time with the CTA-B array, and so is not strictly relevant to the discussion in this thesis. Taken from Sol et al. (2013).

even discovered evidence for the emission originating downstream of the torus in two cases. MWL studies of the November 2010 flare of 3C 454.3 such as those by Wehrle et al. (2012) and Vittorini et al. (2014), have also concluded that the preferred emission model requires an emission location at parsec-scales from the SMBH. The γ-ray emission in the model of Vittorini et al. (2014) is a result of the scattering of photons reflected by a mirror cloud crossing the jet outflow, and is supported by the simultaneous variation in the optical continuum.

Lower and more stable curvature is observed during the flares compared to during the baseline emission either side, as seen in Figs 4.4 and 4.6. In addition to this, the only significant $E_\gamma \geq 20$ GeV emission is observed during the flares. This could be interpreted as a different origin of the flare emission compared to that of the baseline emission. The KN suppression is mitigated as the emission region moves further downstream of the SMBH and BLR (Pacciani et al., 2014), so the increased curvature during the baseline emission is consistent with both the increased KN suppression and the high energy attenuation from pair production in the BLR. This increased curvature could be due to poor photon statistics either side of the flares, but the lack of high energy emission during

these times strengthens the conclusion that the curvature is not due to statistics alone.

The change in emission characteristics during the flaring episode could indicate a multi-zonal emission model, where the baseline emission originates from inside the BLR and the flares from outside the BLR. If more conservative conclusions were made based on the presence of the high energy emission, it could be said that the flares must originate from the downstream half of the BLR or further. Previous studies such as Pacciani et al. (2010), Tavecchio et al. (2010), Bonnoli et al. (2011) and Vercellone et al. (2011) have concluded that the γ-ray emission region was located close to the SMBH during the December 2009 and November 2010 flares of 3C 454.3 respectively. A long-term MWL campaign presented by Vercellone et al. (2010) also concluded that the dominant emission mechanism of γ-rays from 3C 454.3 was the scattering of external photons around the BLR. Given the opposing results in this chapter, a multi-zonal model for the flaring emission of 3C 454.3 may therefore also be applicable. Evidence for multiple emission regions, where emission originates in both the MT and the BLR simultaneously, has previously been presented by Brown (2013) for the FSRQ PKS 1510-089. This conclusion was primarily based on significant changes to the γ-ray spectral shape between flares separated by only a few days, and the seeming lack of correlation between the hardness ratio and the detection of high energy emission. It was concluded that one of the flares that Brown (2013) studied originated in the MT, based on a power law spectral shape and the presence of high energy emission, similar to what is observed here for 3C 454.3.

The investigation into the energy-dependence of the electron cooling did not reveal any significant differential cooling. This would indicate that the emission was originating from inside the BLR. Given the opposing evidence, and the fact that variation is identified in the hardness ratio across the flare period, finding no strong decreasing trend in the hardness ratio as the flares cool is most likely due to the high level of statistical uncertainty.

The short flux doubling timescales discussed in Section 4.2 allow an upper limit to be put on the size of the emission region, $R\delta^{-1} < 2.38 \times 10^{-5}$ pc. Strikingly, there are no corresponding flux halving timescales that are less than 1.5 h. Assuming a leptonic model for the IC scattering, Dotson et al. (2012) show in Fig. 4.12 that the cooling of electrons in the BLR is much faster than in the MT, for a given energy. This is because the IC scattering occurs under the Thomson regime in the MT rather than the KN regime, due to the lower external photon field energies. The comparatively slow cooling that is seen during the 2014 flares of 3C 454.3 is therefore also in support of an emission region that is not inside

the BLR.

The size of the BLR, R_{BLR}^{out}, in 3C 454.3 is ~0.2 pc (Bonnoli et al., 2011). Therefore, the cross-sectional diameter of the jet at $r = 1.3 \times R_{BLR}^{out}$ (r ~0.26 pc), is ~0.05 pc if a constant opening angle of ~0.1 rad is assumed (Ghisellini et al., 2010a). Comparing this to the calculated size of the emission region, $R\delta^{-1} < 2.38 \times 10^{-5}$ pc, the jet at this point is ~3 orders of magnitude too large for the emission region to be covering the cross-section of the jet. This calculation of jet diameter does however assume that the geometry of the jet is constant and cone-like. Studies such as Marscher (2006); Villata et al. (2007); Vercellone et al. (2010) and Mizuno et al. (2015) have suggested that this geometry is not the case for all relativistic jets of AGN, and that the jets may in fact bend or re-collimate in some cases. Structural observations of the jet are difficult when they are directed so closely towards our line of sight, so it may be the case that the geometry of the jet of 3C 454.3 is also not constant. If the jet of 3C 454.3 does re-collimate, the diameter of the jet at the location of the emission region may be smaller than for the assumed geometry.

Alongside the suggestion of multiple emission regions, it is interesting to consider whether or not the γ-ray flares observed from 3C 454.3 could all have been produced by the same population of particles. This might arise when a population of particles in the jet passes through standing shocks at several distances from the SMBH, for example. A study by Jorstad et al. (2005) measured the average bulk Lorentz factor of the jet in 3C 454.3 to be $\Gamma = 15.6 \pm 2.2$, using VLBI observations of features emerging from the stationary core between 1998 and 2001. This is related to the jet speed, v, by:

$$\Gamma = \frac{1}{\sqrt{1 - \frac{v^2}{c^2}}} \qquad (4.6.5)$$

$\Gamma = 15.6$ therefore equates to a speed of $v = 0.998c$ at this point in the jet, a large fraction of the speed of light. Taking the conclusions drawn on the location of the emission region in December 2009 and November 2010 respectively, the speed that the emitting particle population would need to be travelling in order to move between emission locations can be calculated. The locations at which these flare dissipated is of course somewhat disputed, but an emission location of ~1000R_S (~4.8×10^{-2} pc) can be taken for the December 2009 flare (Bonnoli et al., 2011), and a location at the edge of the BLR (~0.2 pc) can be taken for the November 2010 flare (Abdo et al., 2011). In order for the emission region to travel this distance between flares would require an average speed of $v = 1.54 \times 10^8$ ms^{-1}. For

the emitting particles to then travel at least ~0.06 pc down the jet to the location of the emission region in June 2014 would require a speed of $v = 1.54 \times 10^7$ ms^{-1}. It is therefore possible that the emitting particles could have travelled between these locations in the jet of 3C 454.3. These required velocities do appear to be far lower than the jet is thought to be moving, although both the November 2010 and June 2014 locations used were the lower limits of the emission distance from the SMBH. However, the kinematics within relativistic jets of FSRQs are not well understood, and these calculations can only suggest that another population of emitting particles is not *necessary* to explain the three flares at these locations. Since the emission location appears to be increasing in distance from the SMBH with time, it will be thought-provoking if the next bright flare from 3C 454.3 can be constrained to be even farther from the SMBH.

It is suggested that the γ-ray emission region for the June 2014 flares can be well described as a blob-in-jet that is subject to KN suppression outside of the BLR. This is consistent with the short γ-ray flux doubling timescales, the relatively long flux cooling timescales, the presence of significant high energy emission and the small but consistent curvature present in the γ-ray spectrum during these flares. Characterising the emission region as covering the entire cross-section of the jet would also be consistent with obser-vations, if the jet can re-collimate to the size of the emission region downstream of the BLR.

Chapter 5

3C 279

The second γ-ray source that was studied is the FSRQ 3C 279. 3C 279 is less distant than 3C 454.3 at a redshift of $z = 0.536$, or a distance of approximately $7, 400, 000, 000$ light years away. 3C 279 is located at a right ascension (hh mm ss.d) of 12 56 09.9, and a declination (dd mm ss.d) of -05 47 28.0. It was first identified by members of the Radio Astronomy Group of the University of Cambridge, using a radio interferometer at 159 MHz. This discovery was published as part of the original 3C catalog of radio sources by Edge et al. (1959). It was observed as an extremely bright γ-ray source in 1998 by EGRET, featuring as NASA's Astronomy Picture of the Day[1], and was observed at VHE energies in 2006 by the Major Atmospheric Gamma Imaging Cherenkov (MAGIC) telescopes (Albert et al., 2008). It was published as a γ-ray source in the Second EGRET Catalog of High-Energy Gamma-Ray Sources (Thompson et al., 1995). Fig. 5.1 shows an example of the spectral energy distributions that have been observed for 3C 279, illustrating the classic double-peaked structure of blazar SEDs.

The mass of the black hole of 3C 279 is $M_{BH} = (3 - 8) \times 10^8 M_\odot$ (Woo & Urry, 2002; Nilsson et al., 2009; Abdo et al., 2010b), and the luminosity of the BLR is less than in 3C 454.3 by approximately one order of magnitude (Sbarrato et al., 2012). The background information on the analysis methods used in this chapter can be found in Chapter 4.

In this chapter, the γ-ray flare peaking in June 2015 from 3C 279 is studied in detail. This flare can be seen in Fig. 3.3, peaking on MJD 57189. This is the second brightest γ-ray flare that has been detected by *Fermi* from an FSRQ and is the brightest γ-ray flare ever detected from 3C 279. As in Chapter 4, a leptonic origin from a spherical emission region is assumed for the γ-ray emission. In Section 5.1, the method for data preparation used in the *Fermi*-LAT data analysis is described. In Section 5.2 the γ-ray flux variability timescales found during the June 2015 flare are presented, and in Section 5.3 the variation in the shape and hardness of the spectrum is explored, alongside an analysis of the high energy emission. In Section 5.5 an investigation is carried out as to whether or not the cooling of the emitting electron population is energy-dependent. The interpretation of

---

[1]http://apod.nasa.gov/apod/ap981226.html
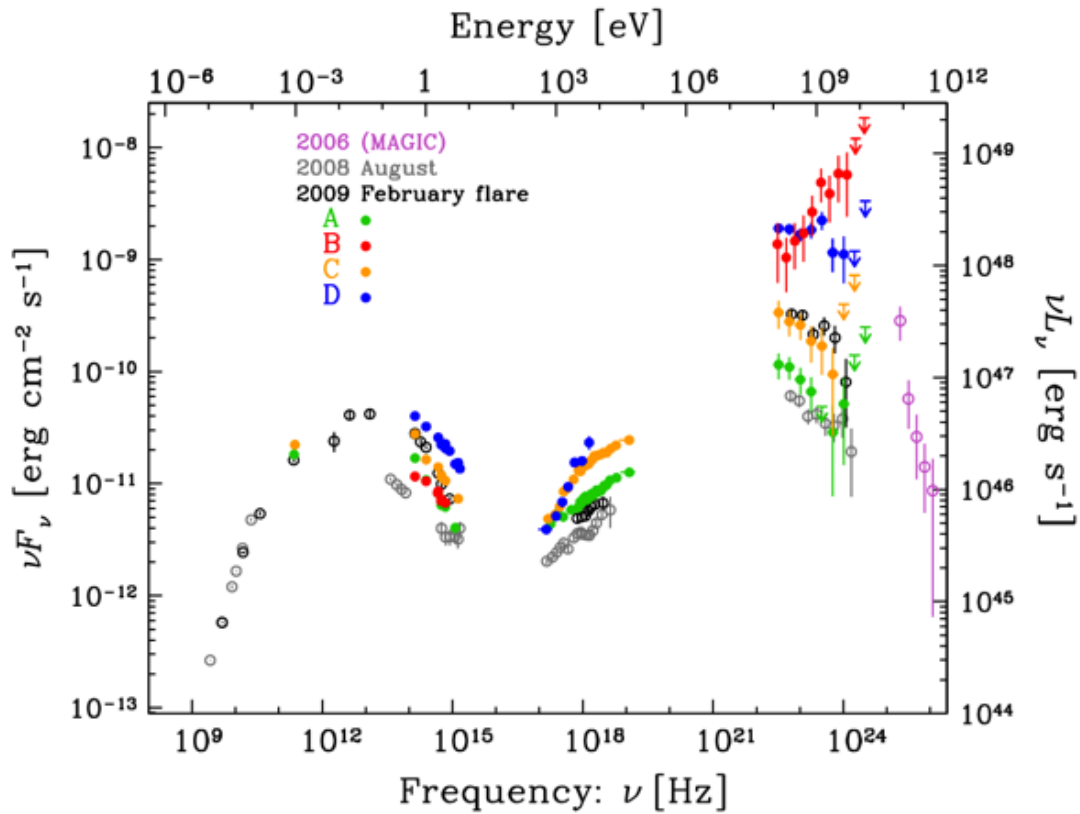
Figure 5.1: Broadband SEDs of 3C 279 for four observational periods between December 2013 and April 2014 (A-D). The vertical bars represent 1σ statistical errors and the downwards arrows indicate 95% confidence level upper limits. The data for these SEDs were collected by the *Fermi-LAT*, the NuSTAR satellite, the Swift-XRT, the Swift-UVOT, the SMARTS project, the Kanata telescope and the Submillimeter Array. Also shown are historical SEDs of 3C 279 in a quiescent state in August 2008, and in a flaring state in 2009 February. These are taken from the 2008-2010 campaign by Hayashida et al. (2012). The data for these SEDs were collected by the Suzaku X-ray satellite, the XMM-Newton, the RXTE-PCA, the Swift-XRT and UVOT, the GASP-WEBT, the Kanata telescope, the GROND, the Spitzer Space Telescope, the CARMA telescopes and the ORVO 40 m telescope. The spectral fluxes measured by MAGIC in 2006 are also plotted (Albert et al., 2008). Taken from Hayashida et al. (2015).

Science Tools version	v10r0p5
IRF	P8R2_SOURCE_V6
Event class	SOURCE, Pass 8
Photon energies	0.1 - 300 GeV
Radius of interest	15°
Zenith angle cut	≤ 90°
Rocking angle cut	< 52°
LAT config./Data quality	==1
Galactic diffuse model	gll_iem_v06.fits
Isotropic diffuse model	iso_P8R2_SOURCE_V6_v06.txt
γ-ray source catalog	gll_psc_v16.fit
Apply RoI zenith-angle cut	In gtltcube

Table 5.1: Table summarising the *Fermi*-LAT analysis criteria used to study the June 2015 flare of 3C 279.

the results is discussed in Section 5.6 and summarised in Chapter 6.

5.1   Data Preparation and Source Modelling

In order to investigate the location of the γ-ray emission region in 3C 279, the photon data collected by *Fermi* between midnight on 1st June 2015 and midnight on the 30th June 2015 were analysed. This is equivalent to the period between MJD 57174 and 57203, during which 3C 279 underwent an extremely bright flare, reported by Cutini (2015). 'Source' class photons in the energy range $0.1 \leq E_\gamma \leq 300$ GeV were once again considered in an RoI of 15°. However, the IRF used to analyse this data was P8R2_SOURCE_V6. In accordance with the guidelines for P8R2 data selection, a zenith cut of 90° was applied. The good time intervals were created by specifying that the LAT detector was at a rock angle of < 52° and the filter expression '(DATA_QUAL==1) && (LAT_CONFIG==1)' was satisfied. The analysis criteria are summarised in Table 5.1.

A binned analysis was run over the period of interest to calculate the best-fitting spectral parameters for each γ-ray source in the RoI. All of the spectral parameters of 3C 279 were free to vary, and the spectral parameters of sources within 12° of 3C 279 were also free to vary. For sources at a radius > 12° from 3C 279, only the spectral normalisation parameters were free to vary in order to allow the MINUIT optimisation to successfully converge. Fig. 5.2 shows the observed counts map, model counts map and percentage residuals map resulting from the binned analysis for 3C 279 between MJD 57174 and 57203. The γ-ray point sources that were defined in the RoI model were taken from the *Fermi*-LAT 4-year Point Source Catalog, 3FGL. The spectrum of 3C 279 was modelled by a log parabola, equation 4.1.1. As can be seen from the residuals map, there were no
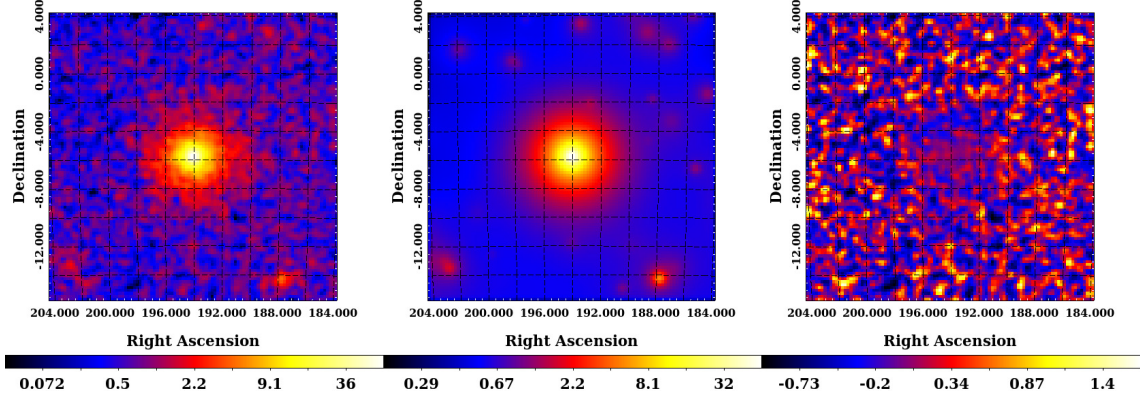
Figure 5.2: $20° \times 20°$ observed (left), model (centre) and residuals (right) maps of the 0.1-300 GeV flux centered on 3C 279. The observed and model maps are in units of γ-ray counts, and the residuals map is in units of percentage. All maps are smoothed with a 2° Gaussian and are at a scale of 0.2°/pixel.

percentage residuals between the observed and model map greater than ~1%. Therefore, no additional sources that were significant during this time period needed to be added to the model.

The spectral parameters of all sources returned from the binned analysis were input into the unbinned analyses. All of the parameters in the RoI except for the normalisation, α and β of 3C 279 were frozen at these values.

5.2 Flux Variability Timescales

Fig. 5.3 shows the fastest flux variability timescales calculated for 3C 279, which are also presented in Tables 5.3 and 5.2. The fastest flux doubling timescale that is found is $\tau_{int} = 1.38 \pm 0.16$ h. Interestingly, no sub-hour flux doubling timescales are found, unlike the June 2014 flare of 3C 454.3. This will be discussed in Chapter 6. Using equation 4.2.4 and $\tau_{int} = 1.38 \pm 0.16$ h, the size of the emission region in 3C 279 can be constrained to $R\delta^{-1} \leq 4.83 \times 10^{-5}$ pc.

The range of the Schwarzschild radius for the black hole of 3C 279 is $(2.87-7.66) \times 10^{-5}$ pc. Taking the smallest intrinsic variability timescale, $\tau_{int} = 1.38$ h, one might conservatively assume that the Schwarzschild radius provides a constraint on the smallest possible radius of the jet. If the size of the emission region is assumed to be $R = 2R_s$, the minimum Doppler factor required for the jet can be calculated from equation 4.2.4, where the value for R is dependent on the size of the black hole. The results of this give between $\delta_{min} \sim 1$ and $\delta_{min} \sim 3$. These values are both much lower than can be expected for a relativistic
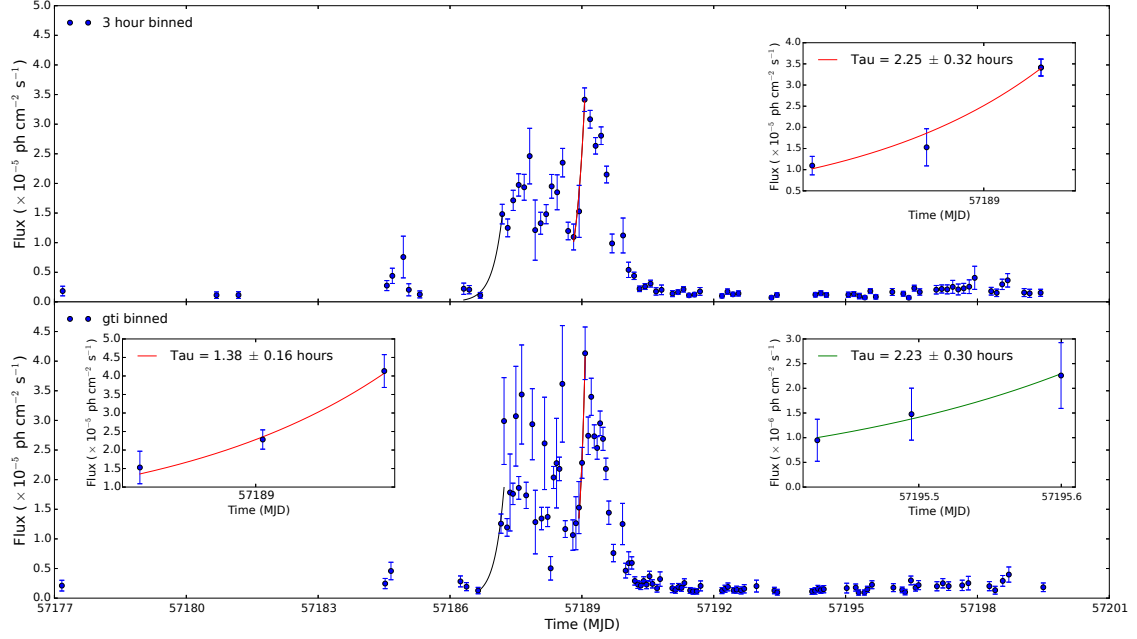
Figure 5.3: The light curve of 3C 279 between MJD 57177 and 57201. Top: 3 hour binned. Bottom: gti binned. The horizontal error bars are not shown here, but are of unequal sizes for the gti binning. The best-fitting curves of equation 4.2.3 are also plotted as lines. The insets show zoomed-in sections of the light curves, for the three timescales that have a significance ≥5σ. These lines are colour-coded so that they can be identified in the main figures. The intrinsic doubling timescales are given in the legend. Only data points with $TS \geq 10$ are shown.

Start Time (MJD)	End Time (MJD)	$F(t_0)$ ($\times 10^{-6}$ ph cm^{-2} s^{-1})	$F(t)$ ($\times 10^{-6}$ ph cm^{-2} s^{-1})	τ_{int} (hours)	Significance (σ)
57188.933	57189.074	15 ± 4	41 ± 4	1.38 ± 0.16	8.62
57186.639	57187.229	1.3 ± 0.5	30 ± 7	2.29 ± 0.72	3.17
57195.429	57195.600	0.95 ± 0.43	2.3 ± 0.7	2.23 ± 0.30	7.42

Table 5.2: γ-ray flux intrinsic doubling timescales of 3C 279 and their significance, from the gti unbinned analysis.

jet, and much lower than previous VLBI observations of this source suggest (Jorstad et al., 2005). It can therefore be concluded that the width of the emission region must be $R > 2R_s$, in order to establish a reasonable Doppler factor for the jet. Taking a Doppler factor of $\delta = 24.1$ from (Jorstad et al., 2005), the size of the emission region can be expressed as $R \leq 1.16 \times 10^{-3}$ pc. This width is ∼2 orders of magnitude larger than the Schwarzschild radius of the SMBH, and is therefore consistent with the emission region being either a blob-in-jet or covering the full cross section of the jet.

Start Time	End Time	$F(t_0)$	$F(t)$	τ_{int}	Significance
(MJD)	(MJD)	($\times 10^{-6}$ ph cm^{-2} s^{-1})	($\times 10^{-6}$ ph cm^{-2} s^{-1})	(hours)	(σ)
57188.813	57189.063	11 ± 2	34 ± 2	2.25 ± 0.32	6.94
57186.313	57187.188	2.2 ± 1.0	15 ± 2	2.49 ± 0.75	3.31

Table 5.3: γ-ray flux intrinsic doubling timescales of 3C 279 and their significance, from the 3 hour unbinned analysis.
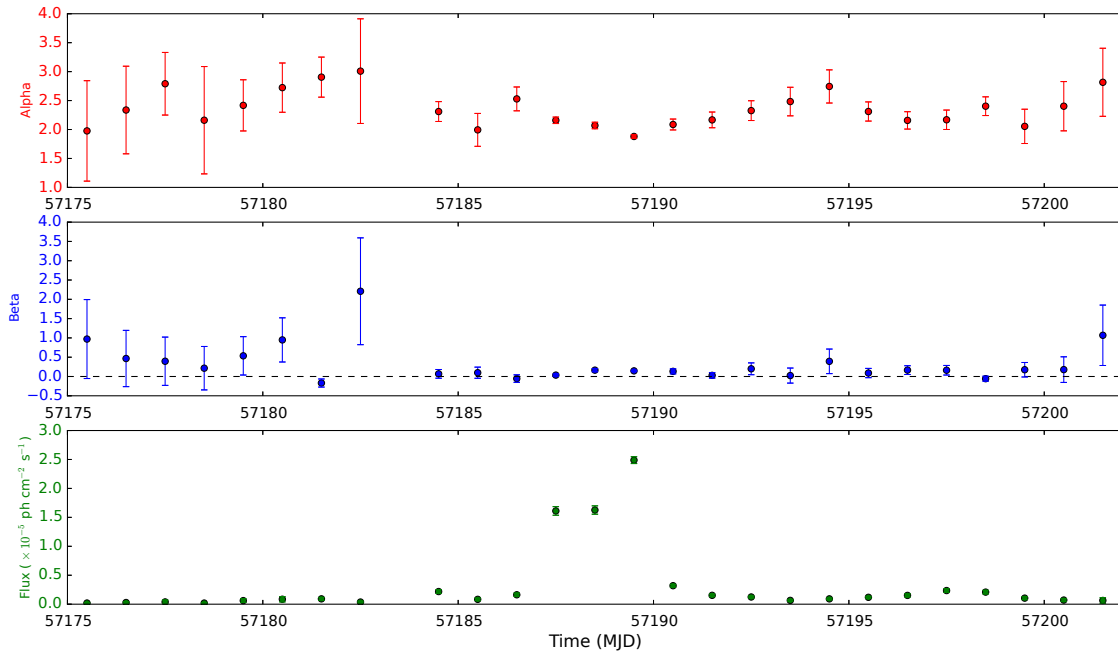
Figure 5.4: Top: α as a function of time. Middle: The variation of β with time. The dashed line is at β=0. Bottom: The γ-ray light curve. All three plots are binned daily. Little spectral variability is identified across the flare. The curvature during the flare is extremely low. Only data points with $TS \geq 10$ are shown.
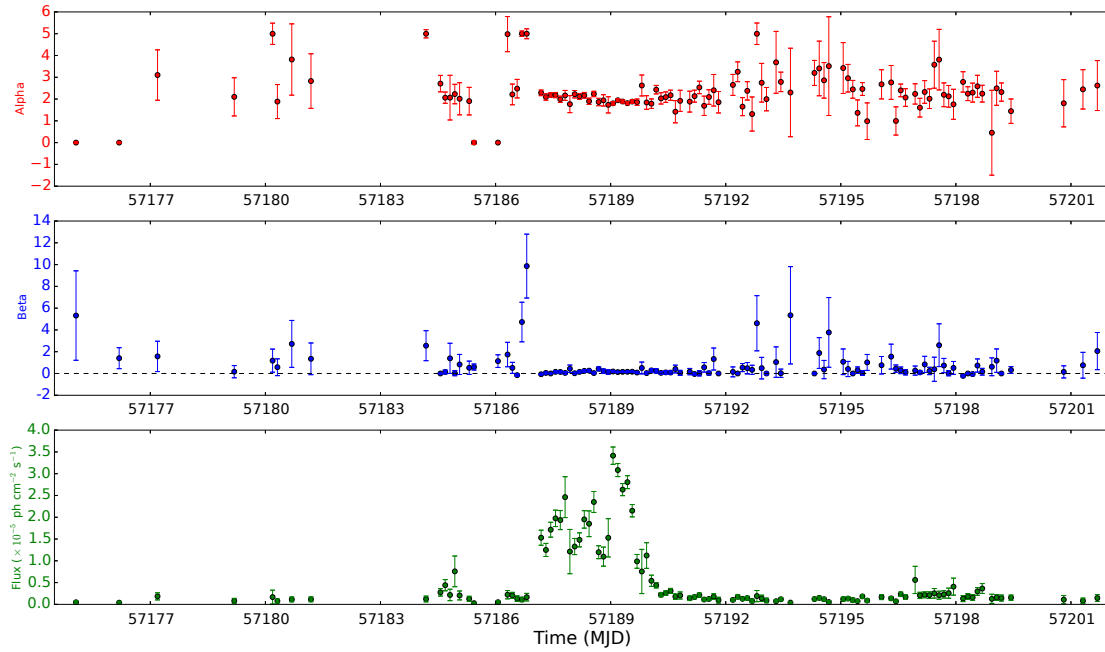
Figure 5.5: Top: α as a function of time. Middle: The variation of β with time. The dashed line is at β=0. Bottom: The γ-ray light curve. All plots are 3 hour binned. Only data points with $TS \geq 10$ are shown.
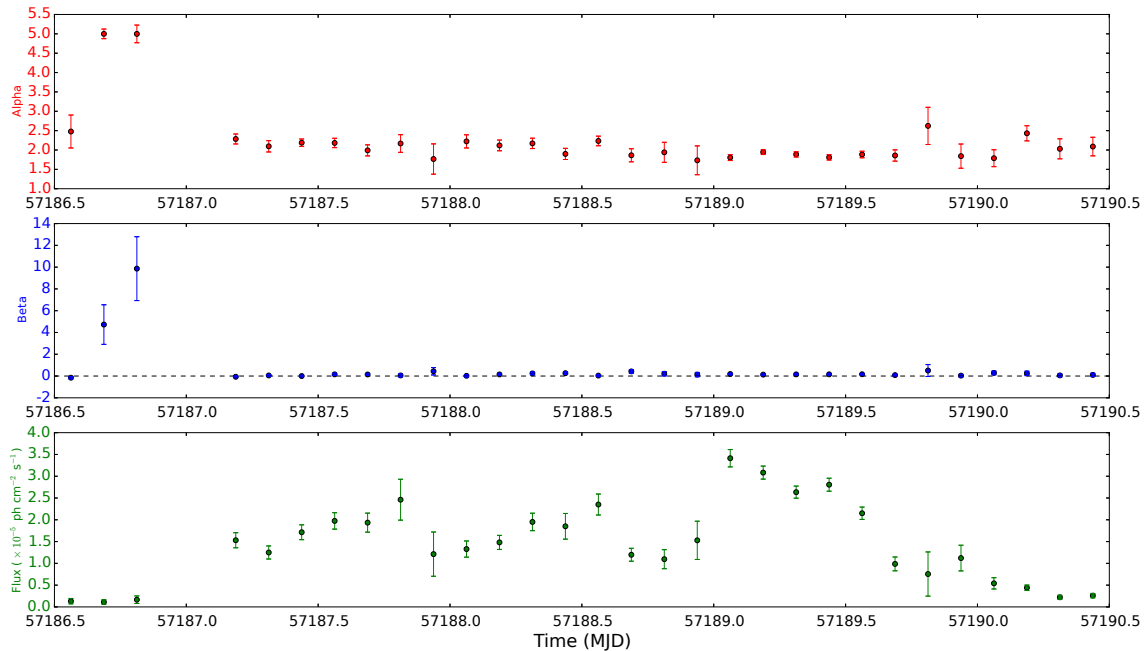
Figure 5.6: Top: α as a function of time. Middle: The variation of β with time. The dashed line is at β=0. Bottom: The γ-ray light curve. All plots are 3 hour binned and show the time period across the flare only. Only data points with $TS \geq 10$ are shown.

5.3   Spectral Variability

Figs 5.4, 5.5 and 5.6 show the spectral parameters and flux of 3C 279 over the period of interest, in daily and 3 hour bins respectively. It can be seen that although the flare is very bright it is also brief, lasting ~3 days in total. Substructures can also be identified within the flare in Fig. 5.6, where three subflares are apparent. The last subflare is the brightest, corresponding to the peak in Fig. 5.4. There is very little spectral variability during the flare. This can be seen by the very flat distributions of both α and β, particularly in the case of the 3 hour binned data. The daily binned values of β both during the flare and afterwards are extremely low, indicating negligible curvature in the spectrum during the flare. The 3 hour binned values of β confirm the presence of only a very small amount of curvature throughout the flare, being consistent with zero in some cases. The values of β before the flare erupts appear to be larger and less well constrained than during the rest of the flare period. The larger error bars before the flare are likely to be due at least in part to poor photon statistics, although the errors on β after the flare has finished are much smaller. Fig. 5.8, β as a function of flux, confirms clearly that the distribution of β is much more flat and very close to zero when the flux is brightest. The lack of curvature during the flare strongly indicates a power law spectral shape. The spectrum is therefore suffering from very little absorption at the high energy end of the spectrum, and so it is extremely unlikely that the γ-rays are being emitted from deep within the BLR.

It can be seen that there is a significant reduction in β when the flare erupts, particularly in the 3 hour binned data. The possibility of multi-zonal emission should therefore be considered, where the baseline emission once again may originate closer to the SMBH.

Neither the daily or 3 hour binned values of α indicate an unusually hard spectrum. It can be seen from the daily data that α becomes lower during the peak of the flare, suggesting a slightly harder-when-brighter behaviour. The 3 hour binned data show a large amount of fluctuation in the value of α before and after the flare, and Fig. 5.7 illustrates that the trend of α with flux is not particularly strong. It can be seen from Fig. 5.7 that α fluctuates between ~1.5 and ~2.5 during the flare, when the flux climbs above $F = 1 \times 10^{-5}$ ph cm^{-2} s^{-1}. Values of α binned in 5 day periods will be presented in Section 5.4, indicating more clearly whether a change in the relative amount of high energy γ-ray emission is observed during the flare. If there is a significant harder-when-brighter behaviour, this will support the conclusion that more high energy emission is detected during the flare because the photons are suffering from less high energy absorption.
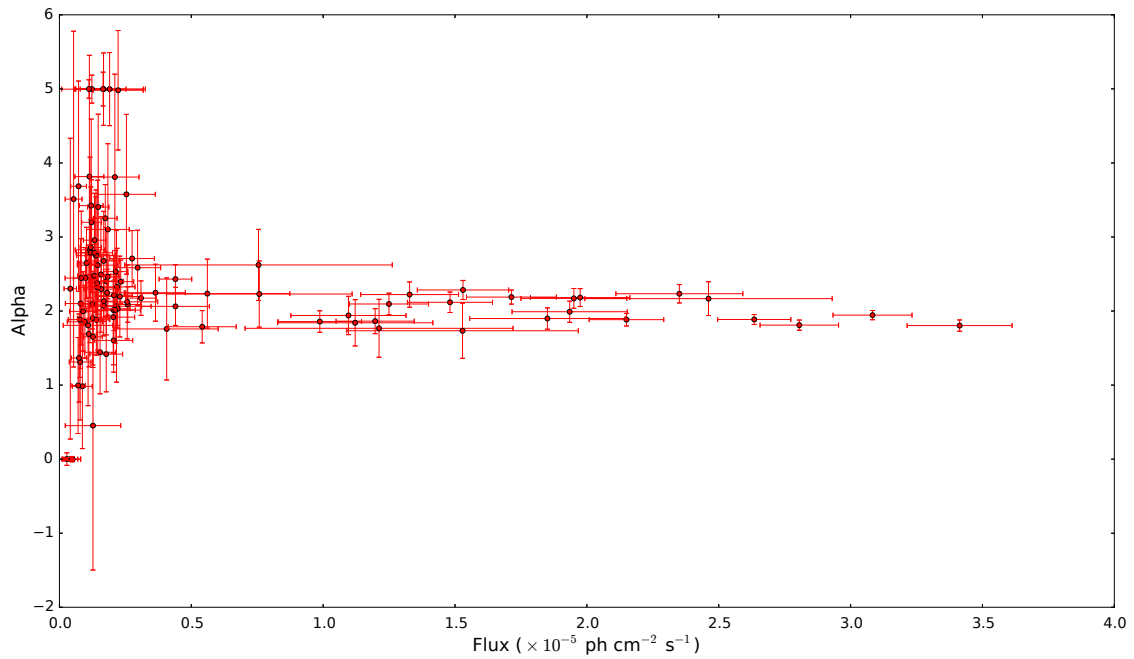
Figure 5.7: α as a function of flux. 3 hour binned. Only data points with $TS \geq 10$ are shown.
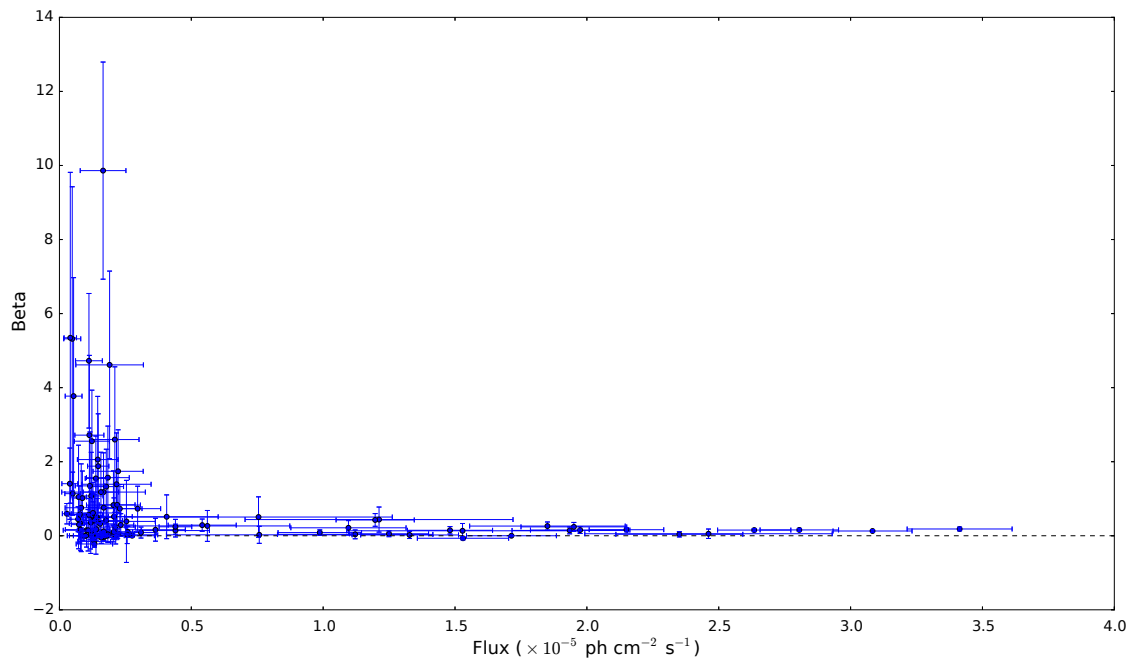
Figure 5.8: β as a function of flux. 3 hour binned. Only data points with $TS \geq 10$ are shown.
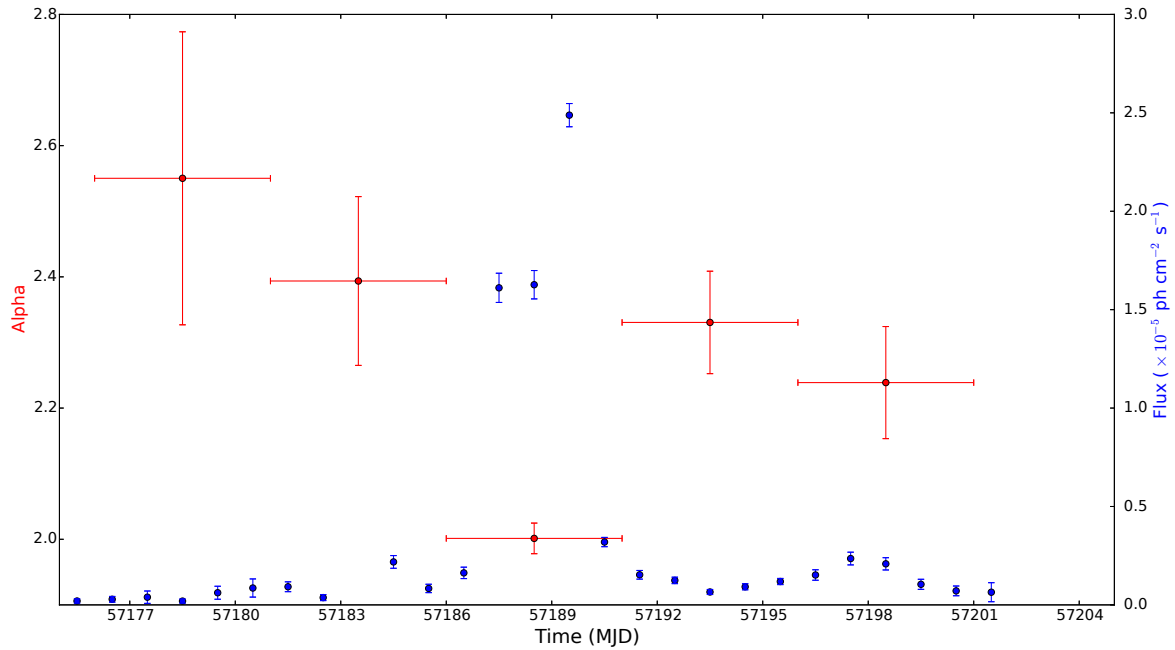
Figure 5.9: α as a function of time, shown in red. The α data points are binned in 5 day periods. The daily binned flux is shown in blue.

5.4 VHE Emission

Fig. 5.9 shows how the 5 day binned values of α vary with the flux of 3C 279. It can be seen that the values of α either side of the flare are consistent with one another, but that there is a significant hardening in the 5 days that include the γ-ray flare. Therefore, relatively more high energy γ-ray emission is being detected during the flare, compared to either side of it. The value of α between MJD 57186-57190 is $\alpha = 2.00 \pm 0.02$. A study performed on the long-term emission of 3C 279 by Hayashida et al. (2012) concluded that a general feature of the γ-ray emission was that the spectral index remained fairly constant, regardless of the flux level. However, this is in contrast to the results shown in Fig. 5.9, and in addition to this, an investigation into the γ-ray emission from 3C 279 in December 2013 by Hayashida et al. (2015) measured a γ-ray spectral index of $\Gamma = 1.7 \pm 0.1$, an even harder spectrum than is observed for the June 2015 flare. These instances both suggest a harder-when-brighter behaviour for 3C 279.

As stated in Section 4.3.2, TeV emission from a blazar usually implies that the source has a spectral index of < 2 (Abdo et al., 2009). However, an unbinned analysis on the γ-ray emission at $E_\gamma \geq 100$ GeV over the period of interest showed no significant flux

Emitted Energy (GeV)	Significance (σ)	Flux ($\times 10^{-9}$ ph cm^{-2} s^{-1})
≥ 35	8.6	1.68 ± 0.76
≥ 50	5.9	0.67 ± 0.47

Table 5.4: The flux and significance for $E_{\gamma,emitted} \geq 35$ GeV and $E_{\gamma,emitted} \geq 50$ GeV, between MJD 57174 and 57203. A single time bin was used over this period.

detected at this energy. 3C 279 has been detected at VHE previously, such as by the MAGIC telescope in 2006 (Teshima et al., 2008). A possible explanation for the lack of VHE emission in June 2015 is that the location of the emission region in 2006 was further from the SMBH than the flare studied here. This would reduce the amount of absorption of high energy γ-rays, such as those at $E_\gamma \geq 100$ GeV. As *Fermi* was not in operation in 2006, no direct comparison of the amount of high energy emission can be made. Although the duty cycle for space-based γ-ray telescopes is much better than for ground-based γ-ray telescopes, ground-based telescopes have a much greater effective area and instantaneous sensitivity with which to detect high energy γ-rays. Given that high energy γ-rays tend to be relatively rare, a greater effective area and instantaneous sensitivity greatly increase the chance of high energy γ-rays being detected.

Taking 5 day bins over the period of interest once again, the significance of $E_\gamma \geq 20$ GeV emission was next assessed. No significant $E_\gamma \geq 20$ GeV emission is found before the flare. However, between MJD 57186-57190, during the flare, the $E_\gamma \geq 20$ GeV flux becomes $F = (7.73 \pm 3.88) \times 10^{-9}$ ph cm^{-2} s^{-1} at a significance of $\sim 8\sigma$. This demonstrates that there is a significant increase in $E_\gamma \geq 20$ GeV emission during the flare. The emission is therefore originating at a location along the jet where $E_\gamma \geq 20$ GeV emission is not significantly absorbed. Between MJD 57191-95 there is an immediate fall in the $E_\gamma \geq 20$ GeV flux, such that it is no longer detected significantly. However, it is detected in the following 5 day period, MJD 57196-57200, at a significance of $\sim 4\sigma$. The lack of $E_\gamma \geq 20$ GeV emission either side of the flare could strongly support the idea of multiple emission regions, as does the significant decrease in α. However, the increased significance of the $E_\gamma \geq 20$ GeV emission later on in June 2015 makes this conclusion slightly less compelling.

Table 5.4 illustrates the significance of $E_{\gamma,emitted} \geq 35$ GeV and $E_{\gamma,emitted} \geq 50$ GeV emission over the entire period of interest. The presence of this high energy emission is quantified in order to place constraints on the distance of the emission region from the SMBH. The $E_{\gamma,emitted} \geq 35$ GeV emission is significant at $> 8\sigma$, and the $E_{\gamma,emitted} \geq 50$ GeV emission is significant at $> 5\sigma$. The BLR is taken to be a spherical shell of outer radius
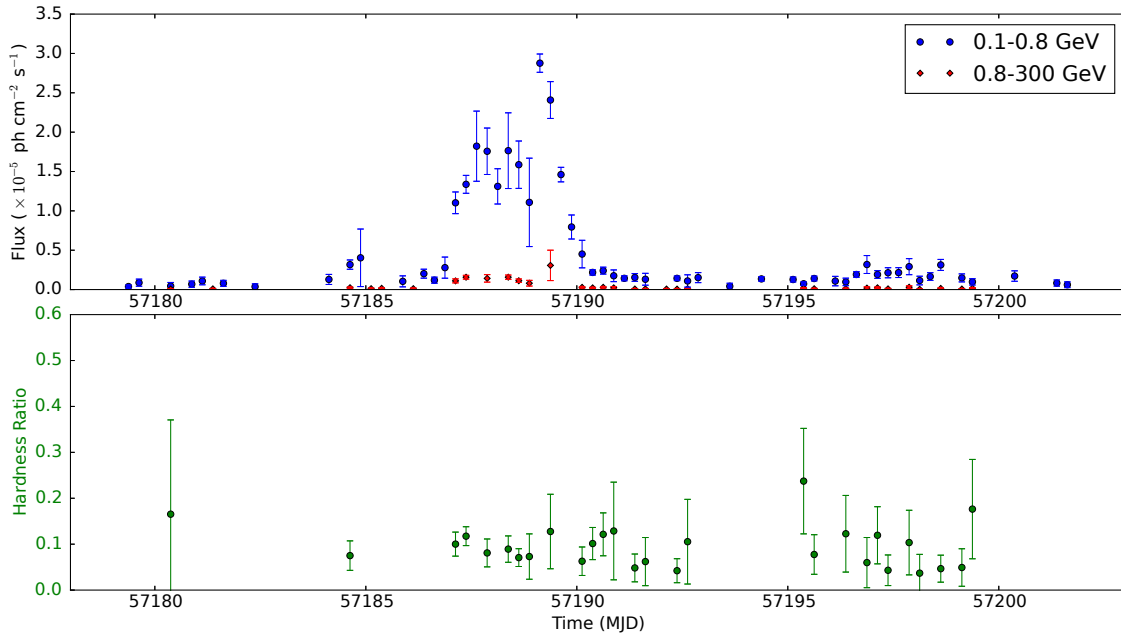
Figure 5.10: Top: The light curve of 3C 279, in 6 hour time bins. The low energy flux, $0.1 \leq E_\gamma \leq 0.8$ GeV is plotted using blue circles and the high energy flux, $0.8 \leq E_\gamma \leq 300$ GeV is plotted using red diamonds. Bottom: The corresponding hardness ratio of the γ-ray emission. This is the ratio of high energy flux to low energy flux. Only data points with $TS \geq 10$ are shown.

$R_{BLR}^{out} = 4 \times R_{BLR}$ (Hartman, 2001; Liu Bai & Ma, 2008). The change in optical depth with distance from the SMBH for $E_{\gamma,emitted} = 50$ GeV photons is considered, as this photon energy gives the tighter constraint on the position of the emission region. If the emission region is located at the distance along the jet where the optical depth for $E_{\gamma,emitted} = 50$ GeV photons reaches a value of $\tau_{\gamma\gamma}(\epsilon) = 1$, approximately one half of the emitted photons are likely to be detected. This optical depth is often taken as the arbitrary opacity at which one might expect to be able to detect photons at a significant level. Using the values of optical depth calculated in Liu Bai & Ma (2008), the position of the emission region in June 2015 must therefore be located at the mid-point of the BLR or farther from the SMBH. This is equivalent to $r \geq 2.5 \times R_{BLR}$, $r \sim 0.25$ pc.

5.5 Energy-Dependent Cooling

Fig. 5.10 shows the light curve of 3C 279, binned in 6 hour periods. The low energy emission, $0.1 \leq E_\gamma \leq 0.8$ GeV, is plotted separately to the high energy emission, $0.8 \leq E_\gamma \leq 300$ GeV. It can be seen from the light curve that there is very little high energy emission

either side of the flare. The lower panel of Fig. 5.10 shows the hardness ratio of the emission. A least squared analysis of the slope of the hardness ratio finds a best-fit slope with a gradient of $m = -(1.9 \pm 0.9) \times 10^{-2}$ as the flare cools, between MJD 57189 and 57193. However, taking into account the large error on the calculated slope, the significance of this result is only $\sim 2\sigma$. Although this evidence is not strong enough to make firm conclusions due to the large amount of statistical uncertainty, the negative gradient may imply that the cooling of the emitting electron population is energy-dependent. This differential cooling would be indicative of a MT origin of the emission, scattering under the Thomson regime. However, visual inspection of Fig. 5.10 highlights that the high energy emission peaks before the low energy emission, which could also cause the hardness ratio to decrease with time over this period. No conclusions can therefore be made on the location of the emission region based on this method.

5.6 Discussion

The spectral parameters observed over June 2015 for 3C 279 give the first indication that the γ-ray emission during this flare is not suffering from large amounts of γ-γ absorption. Although the spectrum might not be considered remarkably hard, it does not seem likely that a large amount of the high energy emission is being attenuated though γ-γ pair production. The curvature in the spectrum throughout the flare is very low, being consistent with zero in some cases. γ-γ opacity arguments can be used to place a lower limit on the distance of the emission region from the SMBH. This reveals that the location of the emission region is $r \geq 2.5 \times R_{BLR}$, based on the significant detection of $E_{\gamma,emitted} \geq 50$ GeV photons. It is not possible to put tighter constraints on the location of the emission region in 3C 279 using the methods employed in this study, due to the relatively less luminous BLR of 3C 279. It is expected that high energy emission at $E_{\gamma,emitted} \geq 50$ GeV would be detected if the emission were located at the mid-point of the BLR, so the opacity constraints cannot provide additional information on the location of the emission region. The lack of spectral curvature observed during the flare period does however suggest that the emission is suffering from very little absorption, and is therefore likely to be farther towards the edge of the BLR than the mid-point. In addition to this, the intrinsic KN suppression shown in Fig. 4.10, arising from the KN IC scattering regime, would introduce a significant amount of curvature into the spectrum if the emission

region was located at the mid-point of the BLR.

A significant spectral hardening is observed during the flare, as can be seen in Fig. 5.9. In addition, although limited by photon statistics either side of the flare, it can also be seen that the curvature present in the spectrum before the flare is generally larger than during the flare. These observations are supported by the detection of $E_\gamma \geq 20$ GeV emission during the flare, but not directly before or afterwards. This suggest that a multi-zonal emission model may be appropriate. Interestingly, there is also a $\sim 4\sigma$ detection of $E_\gamma \geq 20$ GeV emission ~ 5 days after the flare has finished. The curvature in the spectrum during this period is very low, and a small increase in the flux can be seen in Fig. 5.4. If the baseline emission is being emitted from a different part of the jet than the flare, perhaps the emission between MJD 57191-95 contains contributions of flux from both the baseline and flaring emission regions.

Investigation into the energy-dependence of the electron cooling did not produce conclusive results. The decreasing trend of hardness ratio with time during the flare suggests an emission location outside of the BLR, but only at the 2σ level due to statistical uncertainty. The high energy flux may peak before the low energy flux, which would make observing the trend of hardness ratio with time void.

The flux doubling timescales discussed in Section 5.2 constrain the size of the emission region to $R\delta^{-1} \leq 4.83 \times 10^{-5}$ pc. No sub-hour intrinsic flux doubling timescales are found, nor are any intrinsic flux halving timescales that are < 2.5 h at $\geq 3\sigma$ significance. As with 3C 454.3, these relatively long flux halving timescales might indicate that the emission region is not within the BLR, based on the different scattering regimes in the BLR and MT as described by Dotson et al. (2012).

The size of the BLR in 3C 279, R_{BLR}^{out} is ~ 0.4 pc and the inner radius, R_{BLR} is ~ 0.1 pc (Liu Bai & Ma, 2008; Hartman, 2001). Therefore, assuming a constant cone-line geometry of the jet with an opening angle of ~ 0.1 rad, the cross-sectional width of the jet at $r = 2.5 \times R_{BLR}$ is ~ 0.05 pc. Comparing this to the size of the emission region, $R\delta^{-1} \leq 4.83 \times 10^{-5}$ pc, the width of the jet at this distance is ~ 1 order of magnitude larger than the width of the emission region, when a Doppler factor $\delta = 24.1$ is taken. Therefore, if the geometry of the jet is cone-like and constant, the emission region could be modelled as a blob-in-jet, but not as covering the cross-section of the jet. However, if the geometry of the jet is not constant, either model could be applicable and more information would be required in order to draw any conclusions.

By combining the results found in this chapter, it can be concluded that the γ-ray emission region during the June 2015 flare of 3C 279 is located at the mid-point of the BLR or farther from the SMBH. It is strongly suggested that the emission region is located farther from the SMBH than the $\gamma - \gamma$ opacity argument can constrain. This may extend to the edge of the BLR or beyond, based on the lack of spectral curvature throughout the flare. The emission region may either be a blob-in-jet or cover the cross-section of the jet, depending on the jet geometry.

Chapter 6

Synopsis and Comparisons

6.1 Synopsis

In this thesis, data collected by the *Fermi*-LAT were used to examine the $0.1 \leq E_\gamma \leq 300$ GeV γ-ray emission characteristics of flat spectrum radio quasars. Daily binned light curves were created for a selection of FSRQs, illustrating the variation in their γ-ray flux since the launch of *Fermi*. From these FSRQs, 3C 454.3 and 3C 279 were selected for further analysis. Periods during which these two FSRQs underwent bright flaring episodes were isolated, and the γ-ray emission characteristics of these flares were used to put constraints on the location of the γ-ray emission region.

6.1.1 3C 454.3

The γ-ray emission between MJD 56799 and 56855 was analysed, during which 3C 454.3 underwent a bright flaring episode spanning ~25 days. The γ-ray flux doubling timescales were calculated during the period of interest by binning the data into good time intervals, whilst maintaining a $TS \geq 10$ selection criterion. Four intrinsic doubling timescales $\tau_{int} < 1$ h were found, with a fastest doubling timescale of $\tau_{int} = 0.68 \pm 0.01$ h. This allowed an upper limit on the size of the emission region of $R\delta^{-1} < 2.38 \times 10^{-5}$ pc to be calculated.

The γ-ray spectral shape, evidence for high energy emission and the energy-dependence of the electron cooling were investigated, in order to constrain the distance of the emission region along the jet. The spectral curvature during the flares was low and steady in comparison with during the baseline γ-ray emission. Significant $E_{\gamma,emitted} \geq 35$ GeV and $E_{\gamma,emitted} \geq 50$ GeV emission were observed from 3C 454.3 over the flaring period. Optical depth calculations therefore allowed the position of the emission region to be constrained to outside of the BLR, at $r \geq 1.3 \times R_{BLR}^{out}$ from the SMBH. The slight curvature

in the spectrum can be attributed to the KN suppression present outside of the BLR.

It is concluded that the flaring emission region is located outside the BLR. Due to the compact size of the emission region, the emission region is either a blob-in-jet or distributed across the cross-section of the jet, depending on the jet geometry. These conclusions differ from the traditional view of γ-ray emission, both from 3C 454.3 and AGN more generally. They are, however, in support of more recent studies that have reported non-BLR emission from 3C 454.3. It is suggested that 3C 454.3 may be another example of an FSRQ that emits γ-rays from multiple emission regions.

6.1.2 3C 279

The γ-ray emission activity of 3C 279 increased in an unprecedented manner in June 2015, when the FSRQ displayed its brightest γ-ray flare ever detected. The flare reached a peak daily flux of $(2.5 \pm 0.06) \times 10^{-5}$ ph cm^{-2} s^{-1} during its brief ~3 day flare. The period spanning this flare, between MJD 57174 and 57203, was analysed in this thesis. The fastest intrinsic flux doubling timescale found was $\tau_{int} = 1.38 \pm 0.16$ h, using gti binned data at $TS \geq 10$. This flux doubling timescale puts an upper constraint on the size of the emission region of $R\delta^{-1} \leq 4.83 \times 10^{-5}$ pc.

Investigation into the spectral shape of 3C 279 during the flare revealed extremely low spectral curvature, consistent with zero on many occasions across the period of interest. The spectrum also hardened as the flare peaked, suggesting an increase in the high energy emission during the flare compared to during the baseline emission of 3C 279. This information was interpreted alongside a quantitative analysis of the high energy emission during the flare. Significant $E_{\gamma,emitted} \geq 35$ GeV and $E_{\gamma,emitted} \geq 50$ GeV emission were observed from 3C 279, allowing a constraint to be put on the location of the emission region using the luminosity of the BLR and previous $\gamma - \gamma$ opacity studies. This places the minimum emission distance at $r \geq 2.5 \times R_{BLR}$ from the SMBH, the mid-point of the BLR. Evidence is found for an energy-dependence of the electron cooling population at the ~2σ level only, due to statistical uncertainty on the hardness ratio of the flux as the flare cools.

The γ-ray emission region during the June 2015 flare of 3C 279 can be described as either a blob-in-jet or as an emission region covering the cross-section of the jet, based on the size of the emission region and its minimum distance from the SMBH. Without a knowledge of the jet geometry, it is not possible to distinguish between these two cases.

Source	3C 454.3	3C 279
Redshift	$z = 0.859$	$z = 0.536$
Duration of flare	~25 days	~5 days
Peak date	15th June 2014	16th June 2015
Peak daily flare brightness	$(1.3 \pm 0.1) \times 10^{-5}$ ph cm^{-2} s^{-1}	$(2.5 \pm 0.1) \times 10^{-5}$ ph cm^{-2} s^{-1}
Fastest flux doubling	$\tau_{int} = 0.68 \pm 0.01$ h	$\tau_{int} = 1.38 \pm 0.16$ h
Size of emission region	$R\delta^{-1} < 2.38 \times 10^{-5}$ pc	$R\delta^{-1} \leq 4.83 \times 10^{-5}$ pc
Spectral curvature during flare	Low	Low
Energy-dependent e^- cooling	Not found	Not found
Emission location	$r \geq 1.3 \times R_{BLR}^{out}$	$r \geq 2.5 \times R_{BLR}$
Multi-zonal emission suggested	Yes	Yes

Table 6.1: Summary of the γ-ray characteristics of 3C 454.3 and 3C 279 for the flares studied in this thesis.

The combination of the results of the analysis suggest that the γ-ray emission of 3C 279 is dissipating further downstream of the SMBH than the opacity argument can constrain, a result supported by Paliya (2015). 3C 279 may also be a candidate for a multi-zonal emission model.

6.1.3 Comparison of the emission characteristics of 3C 454.3 and 3C 279

A summary of the results found for 3C 454.3 and 3C 279 are presented in Table 6.1 for comparison.

It can be seen from Table 6.1 that the emission region is located outside the BLR in 3C 454.3, but can only be constrained to be at the mid-point of the BLR or farther in 3C 279. However, it is very likely that there will be absorption of high energy γ-rays by the EBL between both of these FSRQs and the *Fermi*-LAT. This means that the significance of the high energy emission escaping from the medium surrounding the emission region is likely to be higher than the results presented in Chapters 4 and 5. This will in turn place the emission location of the flares further from the SMBH.

As discussed in Chapter 4, four intrinsic flux doubling timescales that are < 1 h are found for 3C 454.3. Interestingly, as can be seen from Tables 5.2 and 5.3, no sub-hour intrinsic flux doubling timescales are found for 3C 279. An analysis was also recently done on the June 2015 flare of 3C 279 by Paliya (2015), although the timescales were only probed down to 3 hour bins. In the case of Paliya 2015's results, the smallest flux doubling timescale found was $\tau = 2.2 \pm 0.03$ h, equivalent to an intrinsic flux doubling timescale of $\tau_{int} = 1.4 \pm 0.02$ h in the case of 3C 279. This was observed on MJD 57189, the same day on which the fastest flux doubling timescale $\tau_{int} = 1.38 \pm 0.16$ was measured in this thesis for 3C 279. It is often suggested that the lack of detections of sub-hour flux doubling

timescales could be due to poor photon statistics, but the results found in this thesis strongly suggest that this is not the case. The flare of 3C 279 was almost twice as bright as the flare from 3C 454.3 at their respective peaks, yet the flux is observed to double twice as quickly in the emission of 3C 454.3. This suggests that the lack of rapid flux variation is not due to statistics after all. The rapid variability observed in some γ-ray flares, such as in June 2014 for 3C 454.3 and October 2011 for PKS 1510-089 (Brown, 2013) (Foschini et al., 2013) may actually be a result of the processes occurring within the jet, or a property of the FSRQ itself. An analysis of the March - April 2014 flare of 3C 279 by Paliya, Sahayanathan & Stalin (2015) did in fact find faster flux doubling timescales in 3C 279 than were found for June 2015, of $\tau = 1.19 \pm 0.36$ h, or $\tau_{int} = 0.77 \pm 0.23$ h. This timescale is comparable to those found for 3C 454.3 in June 2014. This flare was also less bright than the 2015 flare of 3C 279. The evidence therefore also suggests that the timescales on which the flux varies may not be dictated by the source itself, unless it is governed by a characteristic that is likely to change in the source with time. The timescales that γ-ray flux vary on are more likely to be linked to a property of the emission process itself.

In the case of both of the flares studied in this thesis, no intrinsic flux halving timescales ≤ 2.5 h are found. This indicates that the γ-ray flux is rising much more quickly than it is falling, and therefore the acceleration or increase in density of the emitting particles is much faster than their cooling. This is often referred to as a 'Fast Rise, Exponential Decay' (FRED) shape of the flare. This has previously been interpreted as evidence that the γ-ray flare is a result of an acceleration of the emitting particles, rather than an increase in the number of particles (Paliya, Sahayanathan & Stalin, 2015). It is possible that a shock front may be the cause of a particle acceleration, giving rise to an increase in γ-ray flux. The slow decay of the flare (i.e. a slow cooling of the emitting particles), could then be attributed to a weakening of the shock. Modelling the emission as the result of an acceleration for the flares studied in this thesis is also consistent with our conclusions based on the shift of the IC SED peak in 3C 454.3, discussed in Chapter 4.

However, shorter flare *decay* times of $\tau = 1.58 \pm 0.51$ h and $\tau = 0.68 \pm 0.59$ h were found for 3C 279 during the March - April 2014 flare by Paliya, Sahayanathan & Stalin (2015) and Hayashida et al. (2015) respectively, although the fitting errors are quite large for the latter timescale. These flux falling timescales are either shorter or comparable with their associated flux rising timescales, $\tau = 1.19 \pm 0.36$ h and $\tau = 6.4 \pm 2.4$ h respectively. In addition, for the June 2015 flare of 3C 279 an analysis of the subflares by (Paliya, 2015)

demonstrated that the second sub-flare also had a flare decay time comparable to the rise time, both taking ~4 h. The flare cooling times for the first and third subflares were however found to be longer than for the corresponding rising times. It would therefore appear that the rise/fall symmetry of γ-ray flares in 3C 279 can differ, suggesting that the cause of the flares may therefore also vary for the same source. Whether or not changes in the symmetry of the flares at a subflare level is significant is also an interesting and most likely complex question. The Paliya (2015) study also noted that the third subflare was the only subflare to be accompanied by a spectral hardening, another intriguing difference at the subflare level of detail.

Having generally characterised both of the flares in this thesis as FREDs based on their lack of fast flux decay times, the light curves themselves demonstrate the differences in the shapes of the flares. Comparing Figs 4.2 and 5.3, there are two primary differences to discuss:

1. The heightened γ-ray activity of 3C 454.3 can be separated into two distinct flares, with the second flare peaking almost ten days after the first flare. These flares can also be clearly distinguished from one another in the daily binned Fig. 4.4. The flare of 3C 279 on the other hand seems structurally more complicated, with 3 smaller subflares visible in the 3 hour binned data. These subflares occur so close in time to one another that they cannot be differentiated when the flux is binned daily, as in Fig. 5.4.

2. It can also be seen that the flaring activity of 3C 454.3 reaches its peak relatively sooner than 3C 279, in terms of the total duration of the respective flares. A steady increase and decrease can be seen in the daily binned flux of 3C 454.5, for both flares. On the other hand, the flux of 3C 279 rises tenfold between MJD 57186 and 57187 before entering a plateau phase, where the flux remains constant within error for the duration of the next day. It is only on MJD 57189 that the flare reaches its maximum, following another ~50% increase in flux. There is no similar evidence for a plateau in the flux of 3C 454.3. This peak of 3C 279 is then followed by a seven-fold decrease in the flux, which does not rise significantly again. Following the peak in the daily binned flux of $F = (2.5 \pm 0.1) \times 10^{-5}$ ph cm^{-2} s^{-1}, the flux returns to an almost quiescent state at $F = (3.2 \pm 0.2) \times 10^{-6}$ ph cm^{-2} s^{-1}. This might lead one to expect this flare of 3C 279 to have rapid flux decay times, but the increased flux

uncertainty in shorter time bins, as shown in Fig. 5.3, is likely to be why this was not the case.

In this thesis, a one-zone leptonic model of IC scattering with external photons is assumed to be the primary method of γ-ray production, as has been done for many similar studies of FSRQs. However, it is possible that the differences in the flare characteristics described above indicate that there are differences in the physical process of producing γ-rays between the sources. The work done by Sol et al. (2013) might suggest that the flare in 3C 454.3 was caused by an increase in energetics of the emitting particles, rather than an increase in density. If the flares from both 3C 454.3 and 3C 279 are not due to particle acceleration alone, this may give rise to a possible explanation for the observed differences in the flares. On the other hand, if both flares are indeed caused by an acceleration of particles, there may still be differences in the particle acceleration mechanisms, even down to differences in the properties of the accelerating standing shocks.

It is also possible that the environment surrounding the emission region is having an effect on the properties of the emission, rather than the emission mechanism itself. The results in this thesis, supported by the work of Paliya (2015), show that for both FSRQs the location of the emission region is likely to be in a part of the jet that is suffering from little γ-γ absorption, at ~0.25 pc from the SMBH or farther. However, the density of the medium surrounding the γ-ray emission region, such as the photon fields or gas and dust clouds external to the jet, is likely to vary between the two sources even at similar distances from the SMBH. In addition, these properties will vary with distance from the SMBH, and there is no conclusive evidence that the emission locations are a similar distance from the SMBH in the two sources, just because they have the same lower constraint. Further examples of properties that may differ between the FSRQs include the accretion rate onto the central SMBH and the power of the relativistic jet, which may also vary with time. These too may be having an effect on the γ-ray emission characteristics.

MWL studies of FSRQs can often give additional insight into γ-ray emission mechanisms. Using MWL data, it has been suggested for both 3C 454.3 and 3C 279 that emission produced from a single region of particles, as is assumed in this thesis, may not in fact be sufficient (Pacciani et al., 2014; Hayashida et al., 2015). Dissecting the December 2009 γ-ray flare of 3C 454.3 into pre-flare, flare and post-flare components, Pacciani et al. (2010) concluded that a second region of emitting particles arising from an acceleration or injection near the base of the jet could be used to model the peak of the emission, whilst

not being necessary pre- or post-flare. This conclusion was based on the time-varying relationship between the flux at different wavelengths, perhaps as a result of a rise in the SMBH mass accretion rate. Multiple simultaneous emission regions have also been suggested for 3C 279 in order to explain the temporal differences in the x-ray and γ-ray flares. If single-region models for high energy flares from FSRQs are not always appropriate, there is an increased complexity in interpreting the emission characteristics in terms of the emission location, as the emission regions may be located in different jet environments.

Having stated that both the γ-ray emission mechanism and location can have an effect on the emission properties of the FSRQs, it may also be worth considering the possibility that the two are connected. In the case of emission being produced by IC scattering of relativistic particles, it could be argued that an injection of additional particles might be more likely to happen closer to the SMBH, although this is a speculative example. It has also previously been shown that standing shocks in the jets of FSRQs often lie in the observable part of the jets, as the 'core' of the jet (Jorstad et al., 2005; Marscher et al., 2010). Of course there may be additional shocks closer to the SMBH that are not observable, but having a standing shock at a considerable distance from the SMBH will most likely increase the likelihood of particles being accelerated far from the SMBH and therefore emitting γ-rays at this distance.

Multi-zonal emission models have been suggested for both 3C 454.3 and 3C 279, including a consideration of whether the same population of emitting particles can emit γ-rays at different locations. In addition to the multi-zonal conclusion of Brown (2013) for the FSRQ PKS 1510-089, Dotson et al. (2015) have also recently concluded that multi-zonal emission is applicable to PKS 1510-089, based on work using energy-dependent electron cooling timescales. Dotson et al. (2015) examined four γ-ray flares from PKS 1510-089 in 2009, all of which are separate events to the flare studied by Brown (2013). The results show that there are multiple γ-ray emission locations in PKS 1510-089 beyond the BLR. Although it was not the case for the sources studied in this thesis, evidence is increasingly demonstrating that an analysis of the energy-dependent electron cooling can be successfully applied to certain flares of FSRQs. As discussed in Section 4.6, previous studies of 3C 454.3 have concluded an emission location close to the base of the SMBH. The work done by Bonnoli et al. (2011) on the November 2010 flare concluded a BLR location of the emission region based on the region's compact size. An investigation into the significance of high energy emission from 3C 454.3 during this flare would provide

complementary information to the work done in this thesis, further testing the likelihood that the emission location in 3C 454.3 is not constant. Unlike for the June 2014 flare of 3C 454.3, a study of the November 2010 flare by Abdo et al. (2011) showed that a plateau stage in the flux was observed before the peak, adding yet another example of differences that can arise in γ-ray flares from the same source, and giving further support to a multi-zonal model in which these differences can be explained.

The March - April 2014 flare of 3C 279 showed a large amount of curvature in the γ-ray spectrum and a non-detection of VHE emission, as well as two distinct flares as observed in 12 hour bins (Paliya, Sahayanathan & Stalin, 2015). The significant detection of high energy emission during the June 2015 flare, as well as the extreme lack of spectral curvature suggest that the emission region in 3C 279 may have also changed since the last major flare, or that the emitting electron energy distribution has changed. Interestingly, the work done by Paliya (2015) on the June 2015 flare concluded that a significant spectral break was present at the peak of the flare, but opacity arguments based on the detection of an $E_\gamma = 52$ GeV photon still placed the emission region at the outer edge of the BLR or beyond, consistent with the results of this thesis.

6.1.4 Future Observations

In addition to a changeable emission location between flares, it is suggested that the emission location also differs between the baseline γ-ray emission and the flaring emission for each FSRQ. This is based on the change in the spectral shape of the γ-rays observed during the flare periods studied in this thesis. A study of the long-term emission from 3C 279 by Hayashida et al. (2012) discusses both parsec-scale γ-ray dissipation in conjunction with a precessing jet, and an emission region within the BLR. Confirming the baseline emission location of γ-rays requires better instrument sensitivity at lower flux levels, so that the characteristics of the baseline emission can be examined. Alongside this, a better characterisation of the baseline emission from FSRQs may in fact reveal varying characteristics or locations, either within individual FSRQs or between sources. A multi-zonal model may therefore also be applicable to the baseline emission of FSRQs.

Future γ-ray observatories are needed in order to make these sensitive observations, particularly at the highest energy end of the γ-ray spectrum. This will soon be made possible by the Cherenkov Telescope Array (CTA), currently in the pre-construction phase (CTA Consortium, 2011). The CTA project aims to build the next generation ground-based

VHE γ-ray instrument. As with *Fermi*, CTA will be an open observatory, and will bring a deep insight into the non-thermal Universe at VHE energies. CTA will be an array of imaging atmospheric Cherenkov telescopes (IACTs), detecting photons between a few 10s of GeV to $E_\gamma \leq 100$ TeV. The array will be comprised of many tens of telescopes constructed in both the Northern and Southern hemispheres, a large number compared to the handful of Cherenkov telescopes currently in operation. This will greatly increase the area over which the CTA can collect γ-rays, as well as increasing the angular resolution and sensitivity of the instrument over its predecessors. Among the primary science goals of the CTA is to explore the nature of particle acceleration mechanisms around SMBHs, further advancing the study of the origin of high energy γ-ray emission from AGN. In addition to future γ-ray observatories, continued MWL studies of FSRQs will provide complementary data, providing simultaneous low energy observations that allow the γ-ray emission properties of blazars to be interpreted in a wider context.

The results in this thesis demonstrate strong evidence that the γ-ray emission from FSRQs can be emitted outside of the innermost regions of AGN, supported by the growing body of work on this subject. As such, I hope that future observations continue to examine bright flares of FSRQs in order to gather further evidence of this for a larger number of sources. In particular, instruments with an increased capacity for high energy γ-ray detections may provide the most compelling new information. Once a multi-zonal emission model is established, it will be fascinating to probe in more depth the dominant factors that dictate where the emission is produced, and why this results in a changeable emission location.

Bibliography

Acero F. et al. (Fermi-LAT Collaboration), 2015, (arXiv:1501.02003)

Ackermann M. et al. (Fermi-LAT Collaboration), 2010, ApJ, 721, 1383

Ackermann M. et al. (Fermi-LAT Collaboration), 2012, ApJS, 203, 4

Ackermann M. et al. (Fermi-LAT Collaboration), 2015, (arXiv:1501.06054)

Abdo A. A. et al. (Fermi-LAT Collaboration), 2009, ApJ, 707, 1310

Abdo A. A. et al. (Fermi-LAT Collaboration), 2010a, Science, 328, 5979, 725

Abdo A. A. et al. (Fermi-LAT Collaboration), 2010b, Nature, 463, 919

Abdo A. et al. (Fermi-LAT Collaboration), 2011, ApJ, 733, L26

Agudo I. et al., 2011, ApJ, 726, L13

Aharonian F., 2001, Proceedings 27th ICRC (Hamburg), Invited, Rapporteur, and Highlight Papers, 250

Aharonian F. et al. (H.E.S.S. Collaboration), 2007, ApJ, 664, L71

Alexander D. M. & Hickox R. C, 2012, NewAR, 56, 4, 93

Albert J. et al. (MAGIC Collaboration), 2007, ApJ, 669, 862

Albert J. et al. (MAGIC Collaboration), 2008, Science, 320, 1752

Aleksić J. et al., 2014, Science, 346, 6213, 1080-1084

Atwood W. B. et al. (Fermi-LAT Collaboration), 2007, Astropart. Phys., 28, 4-5, 422

Atwood W. B. et al. (Fermi-LAT Collaboration), 2009, ApJ, 697, 1071

Atwood W. B. et al. (Fermi-LAT Collaboration), 2012, Fermi Symposium proceedings - eConf C121028, (arXiv:1303.3514v1)

Bastieri D., 2009, Astron. Telegram, #2168

Bennett A. S., Mem. R. Astron. Soc., 1962, 68, 163

Bennett K., 1990, Nuclear Physics B (Proc. Suppl), 14B, 23

Blazejowski M., Sikora M., Moderski R., Madejski G. M., 2000, ApJ, 545, 107

Blumenthal G. R & Gould R. J., 1970, RevModPhys., 42, 237

Bonnoli G., Ghisellini G., Foschini L., Tavecchio F., Ghirlanda G., 2011, MNRAS, 410, 368

Brown A. M., Adams J., Chadwick P. M., 2015, MNRAS, 451, 4842

Brown A. M., 2013, MNRAS, 431, 824

Buson S., 2014, Astron. Telegram, #6236

Buson S. & Gasparrini D., 2013, Astron. Telegram, #5156

Carpenter B., 2013, Astron. Telegram, #5452

Ciprini S., 2010, Astron. Telegram, #2943

Ciprini S. & Hays E. A., 2012, Astron. Telegram, #4182

Ciprini S. & Cutini S., 2013, Astron. Telegram, #4770

Ciprini S., 2015, Astron. Telegram, #7870

Csáki C., Kaloper N., Peloso M., Terning J., 2003, JCAP, 05, 005

CTA Consortium, 2011, Exp. Astr. 32, 193

Cutini S., 2015, Astron. Telegram, #7633

D'Ammando F., 2011, Astron. Telegram, #3655

D'Ammando F. & Orienti M., 2013a, Astron. Telegram, #4706

D'Ammando F., 2013b, Astron. Telegram, #5001

Della Ceca R., Zamorani G., Maccacaro T., Wolter A., Griffiths R., Stocke J., Setti G., 1994, ApJ, 430, 533

Dermer C. D., Finke J. D., Krug H., Böttcher M., 2009, ApJ, 692, 32

Dermer C. D., Yan D., Zhang L., Finke J. D., Lott B., 2015 (arXiv:1504.03228)

Donea A.-C. & Protheroe R. J., 2003, Astropart. Phys., 18, 377

Dotson A., Georganopoulos M., Kazanas D., Perlman E. S., 2012, ApJ, 758, 15

Dotson A., Georganopoulos M., Meyer E. T., McCann K., 2015, ApJ, 809, 164

Dube R. R., Wickes W. C. & Wilkinson D. T., 1977, ApJ, 215, L51

Edge D. O., Shakeshaft J. R., McAdam W. B., Baldwin J. E., Archer S., 1959, Mem. R. Astron. Soc., 68, 37

Foschini L., Ghisellini G., Tavecchio F., Bonnoli G., Stamerra A., 2011a, A&A, 530, A77

Foschini L., Ghisellini G., Tavecchio F., Bonnoli G., Stamerra A., 2011b, Proc. III Fermi Symposium, eConf C110509, (arXiv:1110.4471)

Foschini L., Bonnoli G., Ghisellini G., Tagliaferri G., Tavecchio F., Stamerra A., 2013, A&A, 555, A138

Ghisellini G. & Tavecchio F., 2009, MNRAS, 397, 985

Ghisellini G., Tavecchio F., Foschini L., Ghirlanda G., Maraschi L., Celotti A., 2010a, MNRAS, 402, 497

Ghisellini G., 2010b, ASPC, 427, 249

Gu M., Cao X., Jiang D. R., 2001, MNRAS, 327, 1111

Hagen-Thorn V. A. et al., 2009, Astron. Rep., 53, 510

Harris J., Daniel M. K., Chadwick P. M., 2012, ApJ, 761, 2

Harris J. & Chadwick P. M., 2014, JCAP, 10, 018

Hartman R. C. et al., 2001, ApJ, 553, 683

Hauser M. G. & Dwek E., 2001, ARA&A, 39, 249

Hayashida M. et al., 2012, ApJ, 754, 114

Hayashida M. et al., 2015, ApJ, 807, 79

Hungwe F., 2011, Astron. Telegram, #3694

Iafrate G., 2010, Astron. Telegram, #2687

Jackson N. & Browne I. W. A., 1991, MNRAS, 250, 414

Johnson W.N., Grove J.E., Phlips B.F., Norris J.P., Moiseev A.A., 1997, Nuclear Science Symposium, 1, 27

Jorstad S. G. et al., 2005, AJ, 130, 1418

Jorstad S. G. et al., 2010, ApJ, 715, 362

Jorstad S. G. et al., 2013, ApJ, 773, 147

Kaspi S., Brandt W. N., Maoz D., Netzer H., Schneider D. P., Shemmer O., 2007, ApJ, 659, 997

Katarzyński K. & Walczewska K., 2010, A&A, 510, 63

Kellermann K. I., Sramek R., Schmidt M., Shaffer D. B., Green R., 1989, AJ, 98, 1195

Kormendy J. & Richstone D., 1995, ARA&A, 33, 581

Kniffen D. A., 1989, Proceedings of the Gamma Ray Observatory Science Workshop

Kraushaar W. L. & Clark G. W., 1962, PhysRevLett., 8, 3

Lähteenmäki A. & Valtaoja E., 2003, ApJ, 590, 95

Longair M. S., 2011, *High Energy Astrophysics*, New York: Cambridge University Press

Liu H. T. & Bai J. M., 2006, ApJ, 653, 1089

Liu H. T., Bai J. M. & Ma L., ApJ, 688, 148

Magorrian J. et al., 1998, AJ, 115, 2285

Marscher A. P., 2006, in AIP Conf. Proc. 856, ed. P. A. Hughes & J. N. Bregman (Melville, NY: AIP), 1

Marscher A. P. et al., 2010, ApJ, 710, 126

Mattox J. R. et al., 1996, ApJ, 461, 396

Meegan C. A. et al., 2009, ApJ, 702, 791

Melrose D. B., 2009, (arXiv:0902.1803)

Mizuno Y., Gómez J. L., Nishikawa K., Meli A., Hardee P., Rezzolla L., 2015, (arXiv:1505.00933)

Moiseev A. A. et al., 2007, Astropart. Phys., 27, 5, 339

Nalewajko K., Sikora M., Madejski G. M., Exter K., Szostek A., Szczerba R., Kidger M. R., Lorente R., 2012, ApJ, 760, 69

Nandikotkur G. et al., 2007, ApJ, 657, 706

Nilsson K. et al., 2009, A&A, 505, 601

Nolan P. L. et al., 2012, ApJS, 199, 31

Ojha R., Carpenter B., Becerra J., Krauss F. & Gasparani D., 2014, Astron. Telegram, #6425

Orienti M. & D'Ammando F., 2012, Astron. Telegram, #4409

Pacciani L. et al., 2010, ApJL, 716, L170

Pacciani L., Tavecchio F., Donnarumma I., Stamerra A., Carrasco L., Recillas E., Porras A., Uemura M., 2014, ApJ, 790, 45

Padovani P., 1993, MNRAS, 263, 461

Paliya V. S., Sahayanathan S., Stalin C. S., 2015, ApJ, 803, 15

Paliya V. S., 2015, ApJL, 808, 48

Poutanen J. & Stern B., 2010, ApJ, 717, L118

Pian E., Falomo R., Treves A., 2005, MNRAS, 361, 919

Raiteri C. M. et al., 2008, A&A, 485, L17

Sanchez D. & Escande L., 2010, Astron. Telegram, #3041

Saito S., Stawarz Ł., Tanaka Y. T., Takahashi T., Madejski G., D'Ammando F., 2013, ApJ, 766, L11

Salpeter E. E., 1964, ApJ, 140, 796

Sbarrato T., Ghisellini G., Maraschi L. & Colpi M., 2012, MNRAS, 421, 1764

Smith E. P., Heckman T. M., Bothun G. D., Romanishin W. & Balick B., 1986, ApJ, 306, 64

Sokolvsky K. V. & Schinzel F. K., 2010, Astron. Telegram, #2837

Sol H. et al., 2013, Astropart. Phys. 43, 215

Sikora M., Blazejowski M., Moderski R., Madejski G. M., 2002, ApJ, 577, 78

Sikora M., Stawarz Ł., Moderski R., Nalewajko K., Madejski G. M., 2009, ApJ, 704, 38

Sironi L. & Spitkovsky A., 2009, ApJ, 698, 1523

Striani E. et al., 2010, ApJ, 718, 455

Szosteck A., 2011, Astron. Telegram, #3333

Tavecchio F. et al., 2002, ApJ, 575, 137

Tavecchio F. & Ghisellini G., 2008, MNRAS, 386, 945

Tavecchio F., Ghisellini G., Bonnoli G., Ghirlanda G., 2010, MNRAS, 405, 94

Tavecchio F., Pacciani L., Donnarumma I., Stamerra A., Isler J., MacPherson E., Urry C. M., 2013, MNRAS, 435, L24

Tavani M. et al., 2009, A&A, 502, 995

Teshima M. et al., Proceedings of the 30th International Cosmic Ray Conference, 2008. Volume 3, p.1045-1048

Thompson D. J. et al., 1995, ApJS, 101, 259

Urry C. M. & Padovani P., 1995, PASP, 107, 803

Vercellone S. et al., 2010, ApJ, 712, 405

Vercellone S. et al., 2011, ApJL, 736, L38

Villata M. et al., 2007, A&A, 464, L5

Vittorini V., Tavani M., Cavaliere A., Striani E., Vercellone E., 2014, ApJ, 793, 98

Wakely S. P. & Horan D., 2008, Proc. 30th International Cosmic Ray Conference (Mérida),
    ed. R. Caballero et al., Vol. 3, 1341

Wehrle A. E. et al., 2012, ApJ, 758, 72

Wilson A. S. & Colbert E. J. M., 1995, ApJ, 438, 62

Woo J.-H. & Urry C. M., 2002, ApJ, 579, 530